Comparing Siliciclastic Content of Ramp to Rimmed Carbonate Slope Deposits During Relative Sea Level Highstand

by

Eric Tyler Friedman

A Thesis

In

Geologic Science

Submitted to the Graduate Faculty
of Texas Tech University in
Partial Fulfillment of
the Requirements for
the Degree of

MASTER OF SCIENCE

Approved

Dr. Dustin Sweet
Chair of Committee

Dr. George Asquith

Dr. James Barrick

Dr. Branimir Segvic

Mark Sheridan
Dean of the Graduate School

August, 2017

ACKNOWLEDGMENTS

I would first like to thank my thesis advisor, Dr. Dustin Sweet, for constant input, advice, and encouragement. Without him, this project would not have been possible.

Secondly, I would like to thank my research committee: Dr. George Asquith, who kept me on task with constant encouragement; Dr. Jim Barrick, who allowed me to use his laboratory to dissolve my carbonates and provided instrumental knowledge about carbonate dissolution and mineral identification; and Dr. Branimir Segvic, who added a great deal to this project with his expertise on XRD and clay mineralogy.

Additionally, this project would not have been possible without Dr. Melanie Barnes and Dr. Callum Hetherington, of Texas Tech University, and Dr. Lynn Soreghan, of the University of Oklahoma, who allowed me to utilize their laboratories and the instruments within them. Support for costs associated with this project were provided by student grants from the AAPG Foundation, Geological Society of America, and the West Texas Geological Society. Samples were collected from Guadalupe Mountains National Park under permit #GUMO-2016-SCI-0009. Thank you to Guadalupe Mountains National Park geologist Jonena Hearst for assistance with permitting and to Daniel Pike and Khaled Chowdhury for assistance with field sampling.

Finally, I would like to thank all my friends and family in Lubbock, Florida, and across the country for their unconditional love and support.

TABLE OF CONTENTS

ABSTRACT

The Delaware Basin of west Texas is a world-class example of the reciprocal sedimentation model, which postulates that clastic sediment is delivered past exposed shelf to basins during relative sea level lowstands, whereas carbonate is produced on shelf and shed to basins during relative sea level highstands. However, visible volumes of siliciclastics are present in various highstand slope and basin carbonate deposits observed in the region, yet are absent in others. Shelf geometry may be a control on volume of siliciclastics delivered to the basin during highstands. Rimmed platforms appear more efficient at trapping sand and silt on-shelf than carbonate ramps, based on a higher Remaining Residue Fraction (RRF) occurring in slope and basinal carbonate deposits coeval to a rimmed platform.

Detailed, measured sections of similar environmental facies coeval to both rimmed and ramp settings were assessed both proximally and distally within the Bell Canyon Formation (Guadalupian; rimmed) and Bone Spring Limestone/Cutoff Formation (Leonardian; ramp) to analyze the RRF weight percent. The proximal section coeval to the carbonate ramp has a significantly higher RRF weight percentage (22.77%) and grain-size (17.6 μm D_{50}) than the other three sections (3.59%-6.50%; 8.37-11.2 μm D_{50}). It also has more, and larger, detrital quartz grains than any other section. Therefore, coeval shelf geometry likely played a role in limiting detrital quartz grains from reaching the similar environment in the rimmed system. Additionally, greater transport distance from the shelf likely limited detrital quartz grains from reaching the more distal sections.

LIST OF TABLES

LIST OF FIGURES

LIST OF ABBREVIATIONS

62A	Highway 62-A
ARM	Ancestral Rocky Mountains
BC	Bone Canyon
DQRRF	Detrital Quartz Remaining Residue Fraction
EDS	Energy Dispersive Spectrometer
GLC	Guadalupe Liquid Canyon
LMC	Lower McKittrick Canyon
MAB	Meters Above Base
QCI	Quartz Crystallinity Index
RIR	Reference intensity Ratio
RRF	Remaining Residue Fraction
SEM	Scanning Electron Microscopy
XRD	X-Ray Diffraction

CHAPTER 1

INTRODUCTION

Purpose

The reciprocal sedimentation model postulates that clastic sediment is delivered past exposed shelf to basins during relative sea level lowstand periods, whereas carbonate is produced on shelf and shed to basins during relative highstand periods (e.g., Schlager et al., 1994). In certain formations of the Delaware Basin, visible volumes of siliciclastic sediment occur in highstand slope and basin carbonate deposits. However, other highstand carbonate formations exhibit scarce to no visible siliciclastic fraction. This study hypothesizes that shelf geometry may be a control on either limiting or allowing siliciclastic material into the basin during highstands, such that a rimmed carbonate platform is more efficient at trapping sand and silt on-shelf during a relative highstand than a carbonate ramp. Accordingly, less siliciclastic content would occur in basinal carbonate deposits coeval to a rimmed carbonate platform than a carbonate ramp. To test this hypothesis, I will assess the siliciclastic content of highstand basinal carbonate deposits coeval to both rimmed platform (i.e., Bell Canyon Formation) and ramp (i.e., Bone Spring Limestone/Cutoff Formation) settings.

Determining the possible volume of siliciclastic sediment within carbonate strata during relative highstand periods impacts both scientific and industrial communities. The ability to first-order predict siliciclastic content (from shelf geometry alone) has applicability in the Delaware Basin and analogous systems worldwide in, for example, calibrating logging tools to ensure that highstand deposits are not misinterpreted as lowstand deposits.

Geologic Background

Origin of the Delaware Basin

The Delaware Basin formed in western equatorial Pangea during the Early Pennsylvanian when the Central Basin Platform was structurally uplifted as result of the collision of Gondwana and Laurentia segmenting the older Tobosa Basin into western (Delaware Basin) and eastern (Midland Basin) sub-basins (Cys and Gibson, 1988; Frenzel et al., 1988). The history of structurally controlled basins in the region began in the Proterozoic, and tectonic activity intermittently continued through Pennsylvanian-Permian time (Hills, 1984). The Delaware Basin, located in present day New Mexico and Texas (Fig. 1.1), is bounded by the Marathon orogenic belt to the south, Ancestral Rocky Mountain (ARM) structures to the north, and broad platform areas to the east and west (Bozanich, 1979; Hartman and Woodard, 1971; Ward et al., 1986). The Delaware Basin was largely filled by middle Permian (Guadalupian) time with pre-sorted eolian sandstone and associated siltstone strata that intercalate with carbonate ramp and rimmed shelf strata. The Delaware Basin was uplifted and tilted to the east during Mesozoic and Cenozoic tectonic activity (Adams, 1965), such that the western margin of the basin is well exposed in the modern Guadalupe Mountains.

Evolution of the Pangean Megamonsoon and Eolian Transport

Many studies have been devoted to reconstructing the Paleozoic paleoclimate of western equatorial Pangea. The assembly of the Pangean supercontinent likely caused evolution of a megamonsoonal system in the beginning of Permian time, replacing the prior zonal circulation (Parrish and Peterson, 1988; Tabor and Montanez, 2002; Soreghan and Soreghan, 2007; Soreghan et al., 2008). The megamonsoonal system would have caused strong, seasonal westerly winds to evolve from the typical easterly winds, alternating the source regions of windblown sediment. Provenance studies on coeval loess deposits of the area suggest similar dispersal patterns (Soreghan and Soreghan, 2013). Under those conditions, moist tropical air masses

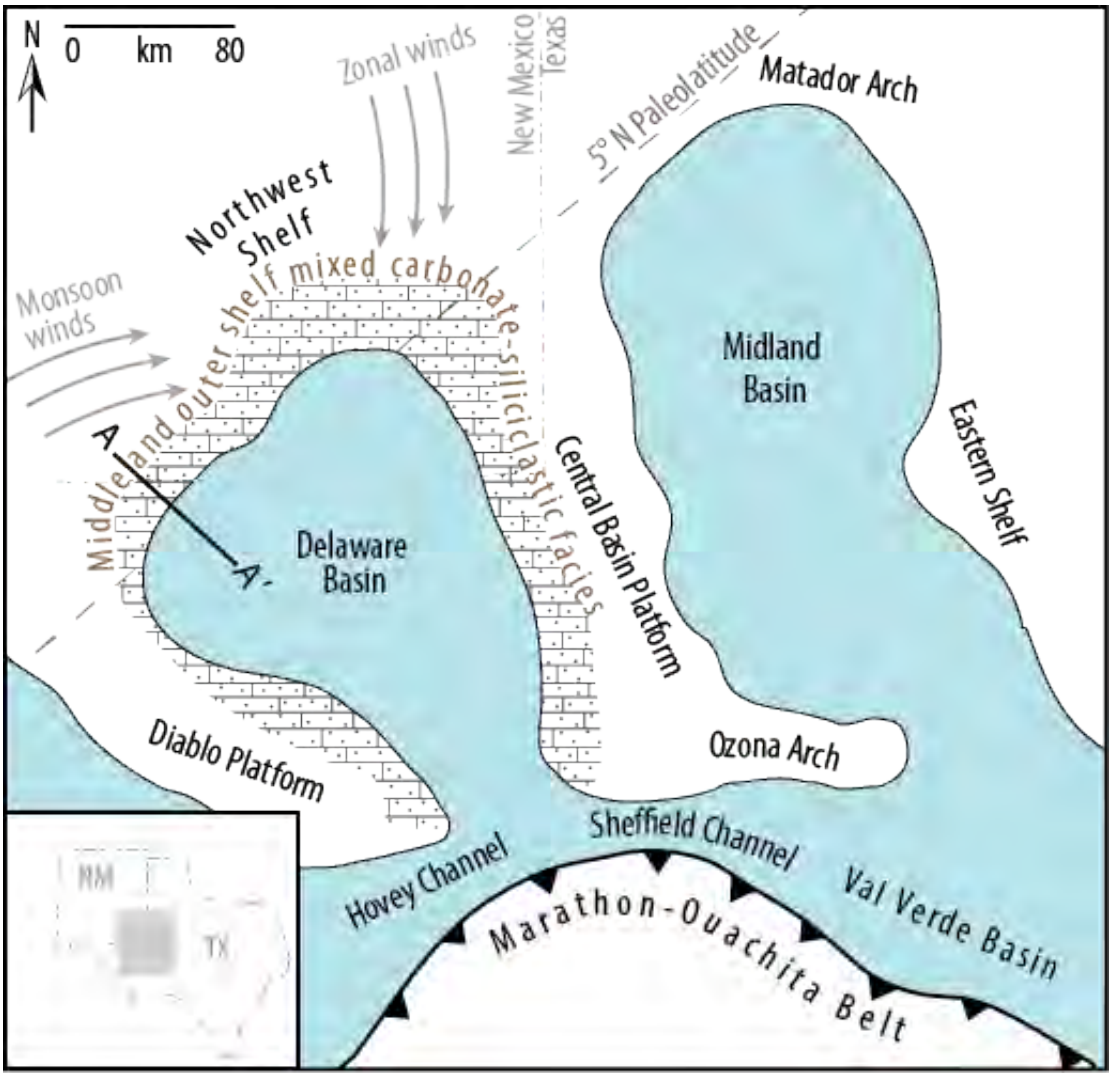

Figure 1.1: Guadalupian paleogeography of the Delaware Basin and surrounding region, adapted from Tinker (1998), Kerans and Tinker (1999), and Ward et al. (1986). A-A' transect is shown in cross section in Figure 1.4. Inset: Gray box denotes approximate location of larger map in west Texas and New Mexico.

would have been pushed northward, creating progressive drying in the tropics of the late Paleozoic (Tabor and Montañez, 2002). In addition, drying of epeiric seas in the region during a global sea level lowstand towards the late Permian should have led to a semi-arid climate, particularly in western equatorial Pangea. Semi-aridity is highly favorable to loess production, as are the presence of glaciers, which may have been periodically present atop equatorial highlands within equatorial Pangea (Soreghan et al., 2014). Loess is prevalent throughout late Paleozoic strata of the region (Soreghan et al., 2008). Global icehouse conditions coincide with sea level lowstand, but as

Gondwanan glaciation waned eustatic sea levels would have risen. Elevated sea level would have resulted in higher sea level conditions in the Delaware Basin, while significant dust was likely still in circulation. Equatorial conditions during the late Paleozoic are ripe for elevated silt concentrations, which explains why the late Paleozoic may be considered the dustiest time in Earth's history (Soreghan et al., 2008), and is perhaps why many carbonates of the period have such an elevated silt content.

The Reciprocal Sedimentation Model

The reciprocal sedimentation model was first developed by Wilson (1967), studying Virgilian strata exposed in the Sacramento Mountains of southeastern New Mexico (Wilson, 1967). Soon after and henceforth, the model has been applied to the Delaware Basin (Silver and Todd, 1969; Jacka et al., 1972; Pray, 1977; Tinker, 1998), allowing clarification of a longstanding stratigraphic conundrum; namely, that shelf-margin facies rimming the Delaware Basin are dominantly *in-situ* carbonate, whereas basinal facies are dominantly detrital siliciclastic sand that bypassed the shelf (Scholle et al., 2004). The model emphasizes that relative sea level lowstand deposition into the basin occurs by clastic bypass of the shelf, whereas carbonate growth occurs on the shelf during relative sea level rise and highstand (Fig. 1.2). More carbonate sediment is produced *in-situ* than can be stored on the platform, and thus must be exported to the basin. Therefore, deposition on the basinal slope from carbonate gravity flows and falling reef blocks, as well as carbonates on the platform top, are highstand deposits (Schlager et al., 1994). The type of deposition in the basin at any given time would thus depend on the contemporaneous rate of base-level change.

The Delaware Basin exhibits a world-class example of this reciprocal sedimentation model (Silver and Todd, 1969) and one in which shelf-to-basin settings are exposed in a continuous outcrop (Tinker, 1998). Sediments on the Delaware shelf demonstrate the classic model characteristics: alternating cycles of carbonate and siliciclastic strata deposited in relation to relative sea level. During relative sea level highstand, carbonate production thrives ("highstand shedding" Schlager et al., 1994).

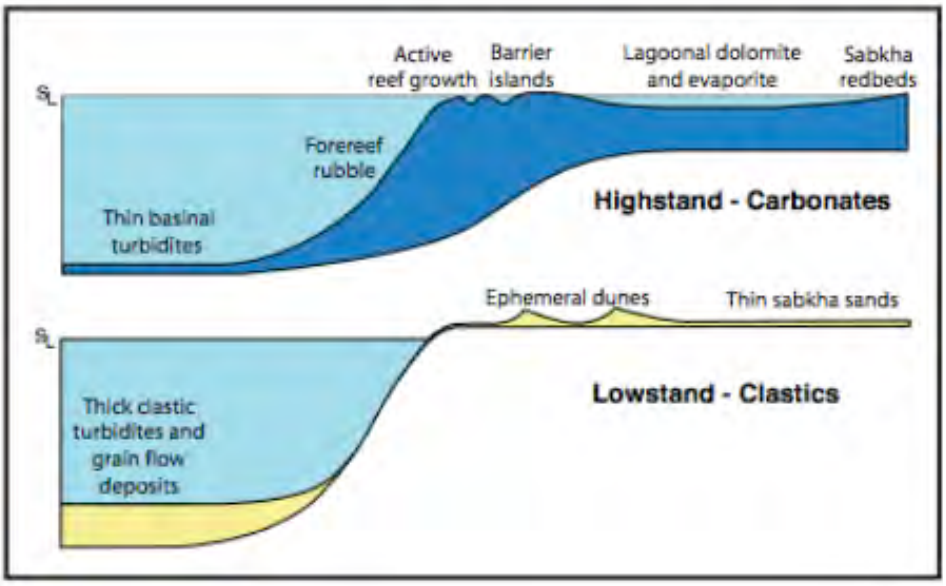

Figure 1.2: Diagrammatic representation of sea level highstand and lowstand deposition in Guadalupian strata (Scholle et al., 2004).

When shelf systems were exposed during relative sea level lowstand, siliciclastic-rich material was delivered to the basin from both fluvial and eolian systems before being reworked by marine processes (Fischer and Sarnthein, 1988).

Stratigraphy of Exposed Units

Bone Spring Limestone

The lower Permian (Leonardian) Bone Spring Limestone (uppermost part of the Bone Spring Formation) exposed in the Guadalupe Mountains records a distally steepened, carbonate ramp environment (Pray, 1977) coeval to the Victorio Peak Formation that represents more proximal shelf deposits. The Bone Spring Limestone is predominantly a dark, thinly bedded cherty limestone that coincided with a decrease in clastic supply, allowing several thousand feet of carbonate deposition (Hills, 1984; Fig. 1.3). Lenticular chert lenses are a key distinguishing characteristic of the unit.

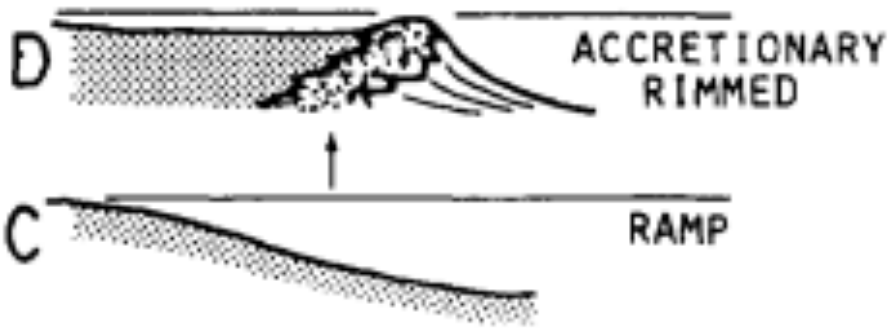

Figure 1.3: Shows the evolution of a carbonate ramp (C) into a rimmed carbonate platform (D) (Read, 1985).

Cutoff Formation

The Lower-middle Permian (latest Leonardian-earliest Guadalupian) Cutoff Formation is an amalgamation of carbonate, shale, sandstone, and breccia deposited in a slope environment. Although deposited over a long-term period of sea-level rise (Hurd et al., 2016), deposition alternated with heavy erosion (Harris, 1987, 2000). The exposed shelf-to-basin transect of the Cutoff Formation along the Western Escarpment of the Guadalupe Mountains is oblique to its depositional dip (Amerman et al., 2011). A large-scale inflection in the depositional slope is likely caused by the antecedent shelf topography consisting of the underlying drowned Leonardian (Victorio Peak/ Bone Spring) platform (Hurd et al., 2016).

Delaware Mountain Group

Stratigraphically above the Bone Spring and Cutoff formations lies the middle Permian (Guadalupian) Delaware Mountain Group that records basin-ward migration of the Capitan reef and shelf edge (e.g., Tinker, 1998). As the section youngs into the Guadalupian, reef-building processes of the Capitan Formation allowed for the carbonate slope to steepen and effectively evolve into a rimmed carbonate platform (Fig. 1.4; e.g., Read, 1985). The Delaware Mountain Group is divided into three units: the Bell Canyon, Cherry Canyon, and Brushy Canyon formations (youngest to oldest). The Brushy Canyon (300 m thick), Cherry Canyon (400 m thick), and Bell Canyon (500 m thick) formations are units of middle to late Permian (Guadalupian) basin fill (Fischer and Sarnthein, 1988) composed of over 90% terrigenious siliciclastic

Figure 1.4: Simplified cross-section of the upper Cisuralian (Leonardian) and Guadalupian series along the northwest margin of the Delaware Basin. Line of cross-section is shown as A-A' on Figure 1.1. Capitanian data is compiled from Tinker (1998). Leonardian through early Guadalupian is from Sarg (1988). Time scale is from Gradstein et al. (2012). Orange/tan fill is undifferentiated shelfal facies. Light blue fill is reef facies. Purple fill is slope and basinal carbonate strata. Yellow stippled fill is basinal sandstone strata. QF = Queens Formation, GF = Grayburg Formation, SAF = San Andres Formation, BCF = Bell Canyon Formation, CCF = Cherry Canyon Formation. Green lines represent approximate locations of Guadalupian sections. Red lines represent approximate locations of Leonardian sections. Section lengths are not to scale.

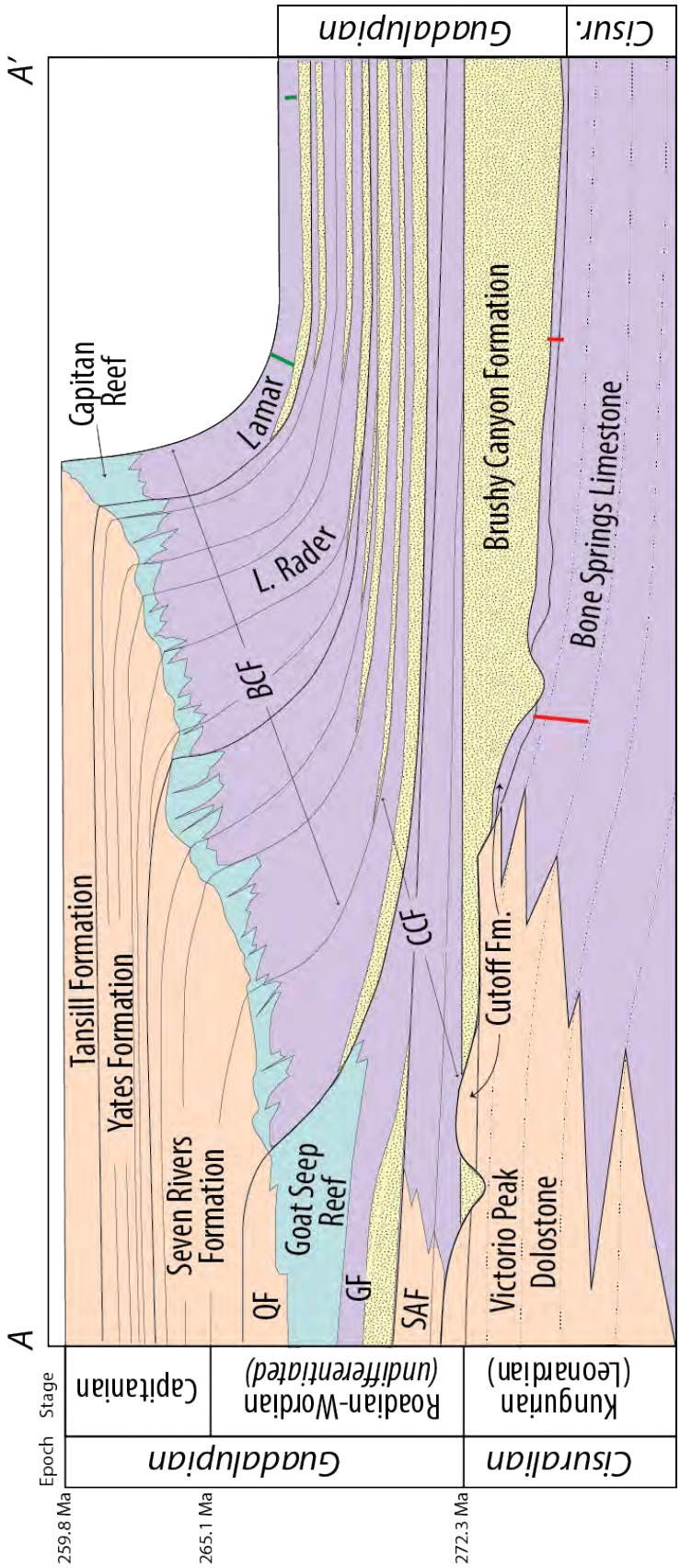
A
A'
Cisur.
Guadalupian
Capitan Reef
Lamar
L. Rader
BCF
CCF
Brushy Canyon Formation
Bone Springs Limestone
Tansill Formation
Yates Formation
Seven Rivers Formation
Goat Seep Reef
QF
GF
SAF
Cutoff Fm.
Victorio Peak Dolostone
Capitanian
Roadian-Wordian (undifferentiated)
Kungurian (Leonardian)
Guadalupian
Cisuralian
Epoch
Stage
259.8 Ma
265.1 Ma
272.3 Ma

sediment, along with thin carbonate debris aprons (Scholle et al., 2004). Fischer and Sarnthein (1988) proposed that there are dual eolian and marine mechanisms responsible for siliciclastic sediment deposition in the Delaware Basin. While sands were swept into eolian dunes on the coast, silt was carried out into the basin where it eventually settled and deposited as laminated units. Clay was carried by wind even farther, which explains the scarcity of detrital clay-sized grains within the Delaware Mountain Group. During relative sea level lowstands, sand was exported to the basin as well-sorted and ungraded turbidites forming deep-sea fans, now recorded in the Brushy Canyon Formation. As relative sea level increased upward though the Guadalupian, sediment became less sorted. Sand and silt mixed on-shelf before being deposited in the basin via gravity flows, as recorded in the Cherry Canyon and Bell Canyon formations (Fischer and Sarnthein, 1988). These turbidite sandstone deposits are interbedded by two other lithologies: organic-rich siltstone beds, which accumulated from settling of suspended eolian sediment and dead marine algae (Dutton, 2008), and basinal carbonate units, which are typically dark colored, very fine grained, and finely laminated (Scholle et al., 2004). Thus, during deposition of the Cherry Canyon and Bell Canyon formations the clastic sandstone was deposited during times of relative lowstand, when sand could bypass the shelf as dune fields or via ephemeral rivers that incised through exposed reef. However, the basinal carbonate units were likely deposited during relative highstand, when carbonate being produced on the shelf was exported via gravity flows to the basin. It is these carbonate intervals within the Bell Canyon Formation that is an area of interest to this study.

CHAPTER 2

METHODOLOGY

Study Location: Delaware Basin Comprises an Ideal Natural Laboratory

The uplift of the Delaware Mountain Group has exposed a transect across numerous Permian-aged units, which allows for comparison of the Bell Canyon, Cutoff, and Bone Spring formations without necessitating sub-surface coring. This type of continuous lateral and vertical exposure is extremely rare (Tinker, 1998). The Delaware Basin is also a prolific hydrocarbon reservoir that is currently being produced. Because of the incredible exposure and interest of the hydrocarbon industry, the lithostratigraphy and sequence stratigraphy of the basin's shelfal units are very well correlated and understood (e.g., Pray, 1977). Thus, the Delaware Basin is an ideal natural laboratory to test the effect of shelf geometry on the siliciclastic input into the basin during relative sea level highstands.

Sampling Strategy: Identifying Coeval Rimmed and Ramp Basinal Deposits

To compare the siliciclastic content between the different formations, samples were collected along detailed, measured sections through similar environmental facies of the Bell Canyon and Bone Spring/Cutoff intervals. Samples (1.0-2.0 kg) were collected (only from beds that contain no extensive zones of chert) to assess the weight percent of the non-carbonate/organic fraction, hereafter termed the *Remaining Residue Fraction* (or RRF). This was done as follows: 1) weigh initial sample, 2) dissolve carbonate with 10% formic acid, 3) oxidize organic matter using 34% hydrogen peroxide, and 4) weigh remaining RRF. This process was modified from the technique presented in Sur et al. (2010). After separation, the RRF fraction was analyzed using binocular microscope, X-ray diffraction, and scanning electron microscope to assess the mineralogical content.

Physical Processing

Acidification Methodology

Bulk samples were washed to remove any modern soil, debris, or encrustations, and then crushed with mortar and pestle, which were cleaned prior to each usage. Crushed samples were weighed, then subjected to 10% formic acid treatment that occurred over a multi-day to week period. Samples were decanted, stirred, and refilled with acid as needed. Upon termination of dissolution activity, beakers were filled with deionized water, and then decanted upon settling, until samples were free of excess acid.

Oxidation Methodology

To remove the organic material from the indissolvable fraction; residue was subjected to 20 ml of 34% hydrogen peroxide in 300 ml of deionized water and stirred twice daily until reaction ceased. Beakers were stirred and refilled with deionized water, as needed. The RRF was extracted upon completion of this step.

Removal of Sample for Grain-Size Analysis

While still in solution, the RRF was stirred and approximately 5 ml was removed while sediment was suspended. Grain-size distribution was analyzed with a Malvern Mastersizer Hydro SV laser particle-size analyzer in the laboratory of Dr. Lynn Soreghan at the University of Oklahoma.

Separation of Coarse and Fine Fractions

Samples in solution were wet sieved, one beaker at a time, on 62.5 μm mesh in order to separate out coarse and fine grain-size fractions, which were dried and weighed separately. The total RRF weight percent was determined by dividing the

combined coarse and fine RRF weight by the initial bulk rock sample weight. Chert-rich incompletely dissolved rock fragments (chert fragments) were sieved out of the coarse RRF using 2 mm mesh. Weight of any granule-sized chert fragments caught in the sieve was subtracted from the original rock weight, so that the RRF weight percent would not be significantly inflated. Sand-sized pieces of chert fragments, though typically rare, occur within the RRF weight percent in certain samples.

Further Analyses

Binocular Microscopy

The coarse fractions of the RRF were analyzed via binocular microscope to determine relative abundance of mineralogy and presence of detrital shaped quartz grains.

X-Ray Diffraction

Mineral quantification was conducted using the Reference Intensity Ratio (RIR) method that uses simultaneous equations to solve analytic concentrations in a multicomponent mixture. Many vendor programs interface to ICDD database to automatically extract I/Ic and peak areas from the experimental data for automated quantitative analysis. I/Ic stands for the ratio between the measured intensity of a phase present in the mixture and intensity of the standard, in this case corundum. Automated programs assume that the combination of all phases identified account for all observed scattering and 100% of the specimen. Significant errors can occur, if there are non-crystalline phases or unidentified materials present in the specimen. RIR concentrations are expressed in weight percent.

X-ray powder diffraction analysis was performed on the RRF and clay-sized fraction of the RRF. Sample preparation initially included material powdering in an agate mortar prior to RRF measurements. Out of 24 measured RRF samples, six

representative samples were chosen for further investigations on the clay-sized fraction. To prevent possible mixing of detrital with authigenic clays, the samples were not powdered but only gently disaggregated.

The clay-sized fraction was separated from the crushed material by centrifuge. Further disaggregation was accomplished in an ultrasonic bath. To ensure a uniform cation exchange, clay-sized fractions separated by centrifuge were saturated with Mg using a solution of 10 ml of approximately 4M $MgCl_2$. Suspensions were washed and centrifuged with distilled water at least three times to minimize the content of free ions. The suspended material was transferred to the mount glass using a pipette. After the clay suspension was drawn onto the mounts, it was left to dry overnight. The thickness of such prepared mounts exceeded 50 μm, which is required for semi-quantitative determination of the clay mineral content (e.g., 'infinite thickness' of Moore and Reynolds Jr., 1997).

The measurements were undertaken in air-dried conditions. A Rigaku MiniFlex II machine at Texas Tech University was used for XRD analyses. Measurement parameters comprised a step scan in the Bragg-Brentano geometry using CuKα radiation (30 kV and15 mA). At a counting time of 10 s per 0.05°, sample mounts were scanned from 2° to 80° 2θ for RRF measurements. At a counting time of 1 s per 0.02°, sample mounts were scanned from 3° to 70° 2θ for clay-sized fraction measurements.

Scanning Electron Microscopy

Scanning electron microscopy was conducted at Texas Tech University. Various grains from the RRF were placed on stubs and coated according to standard operating procedure, in order to gain insight on grain morphology. Energy dispersive spectrometers (EDS) were utilized to gain insight on grain mineralogy. EDS phase chemistry spectra obtained were compared to an online database from McGill University to determine best mineralogical fit. All images were captured using a 15.0 kV beam.

CHAPTER 3

RESULTS

Stratigraphic Sections

Lower McKittrick Canyon

The Lower McKittrick Canyon (LMC) section is 26.1 meters of exposed limestone measured in the Lamar Member of the proximal Bell Canyon Formation (Fig. 3.1). The weathered rock surface is elephant gray, and fresh rock is slightly darker than the exposed surface. Above 10 meters above base (MAB) the section is measured on sporadic subcrop, and the uppermost subcrop on the hill 26.1 MAB represents the top of the section.

Observations showed that the base of the section is micrite that grades into wackestone and packstone moving upwards. The planar bed sets typically range from 5-15 cm thick and are laminated with sharp bases. Floating brachiopods and other diverse fauna are common across the entire unit, creating small local pockets of wackestone to floatstone. A wide variety of other allochem types also formed components of various samples, including calcispheres, sponge spicules, quartz silt extraclasts, foraminifera, echinoderms, and broken shell hash (Fig 3.2).

Highway 62-A

The Highway 62-A (62A) section is 3.5 meters of road-cut outcrop representing the distal Bell Canyon Formation (Fig. 3.3). Using the stratigraphic relationships of Tinker (1998) and field correlations, the section is most likely within the Lamar Member or McCombs Member of the Bell Canyon Formation.

The section is composed of gray, planar-laminated, silty biomicrite with local sparsely fossiliferous wackestone intervals interbedded throughout. These internally laminated beds typically range from 5-10 cm, with the main allochemical

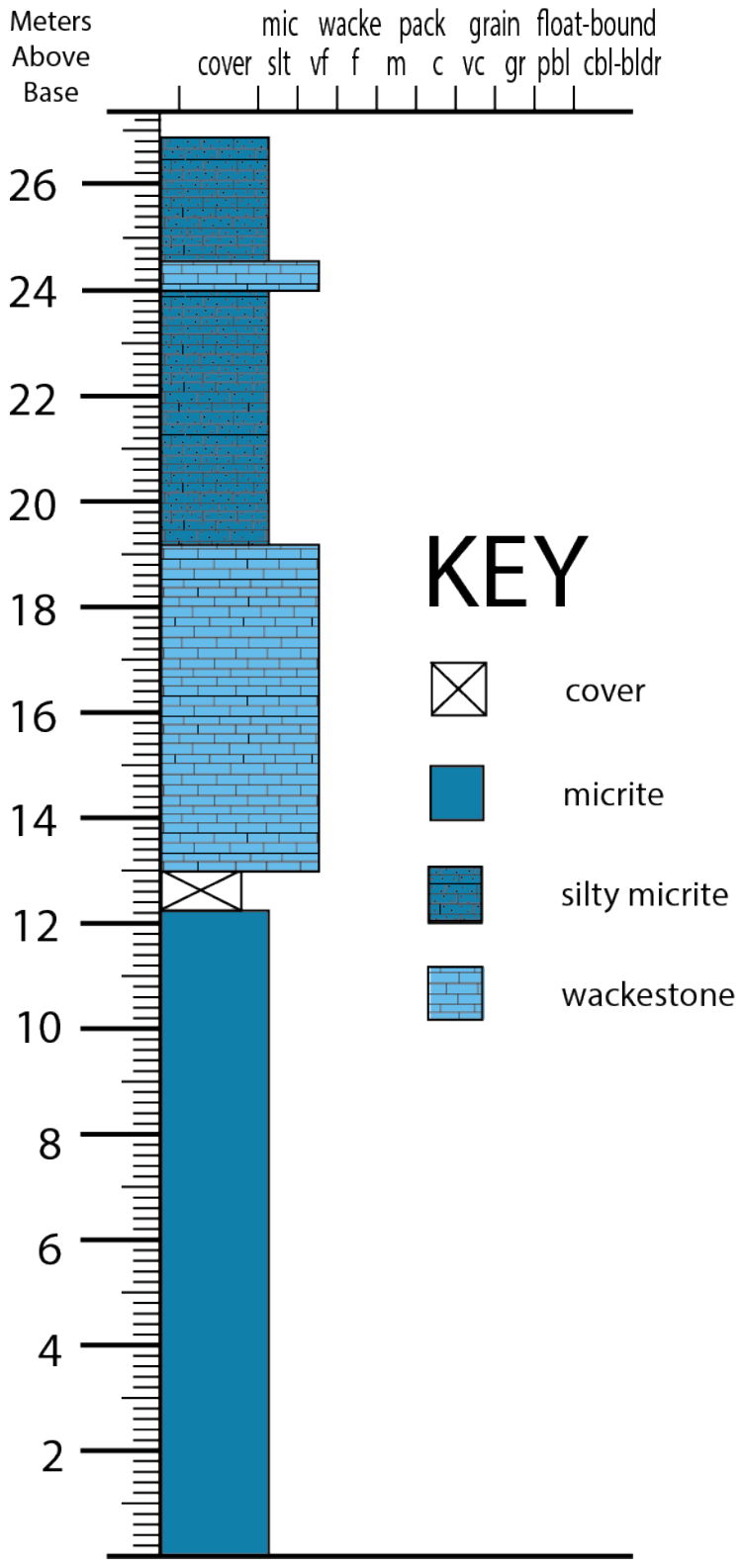

Figure 3.1: LMC stratigraphic column.

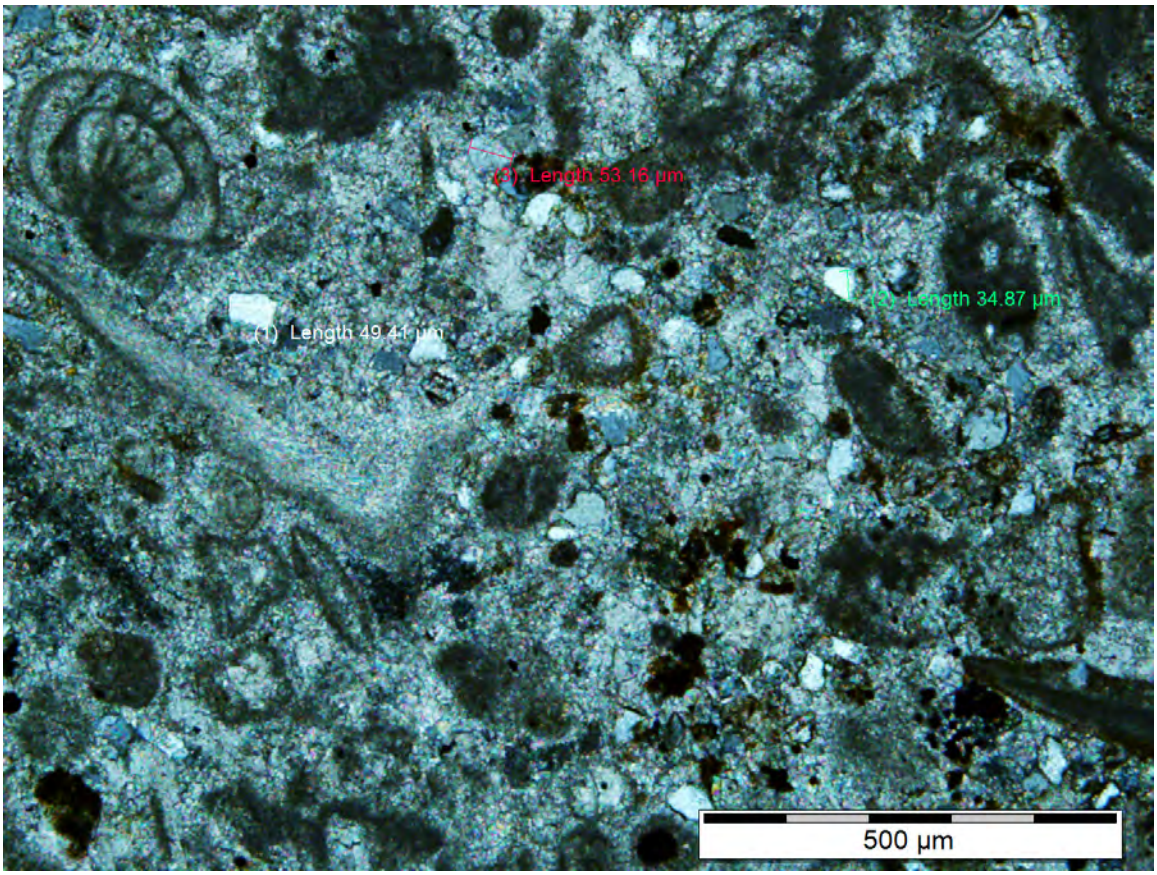

Figure 3.2: Photomicrograph taken from LMC-24.5 in cross-polarized light. Quartz grains measured are silt-sized.

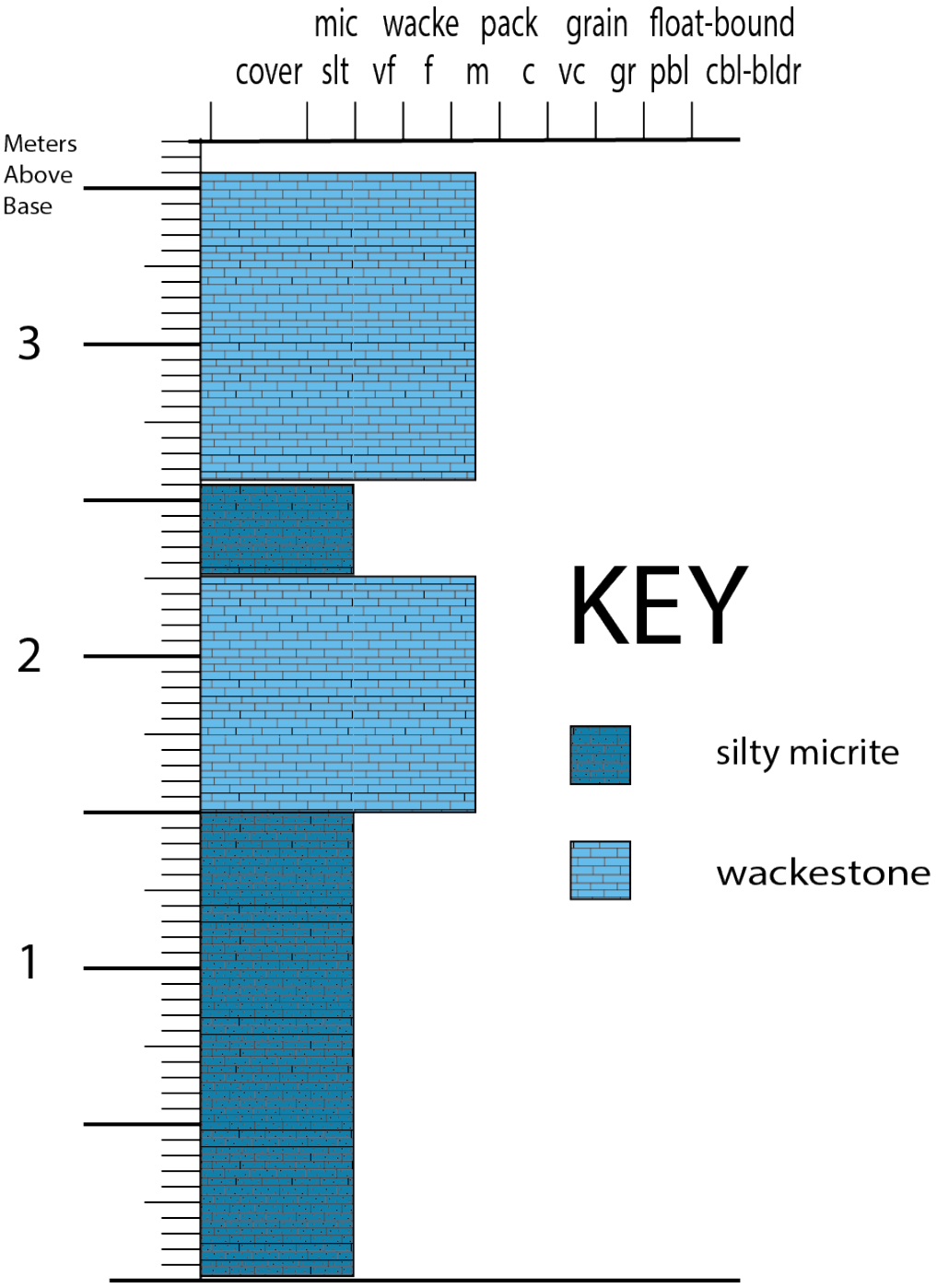

Figure 3.3: 62A stratigraphic column.

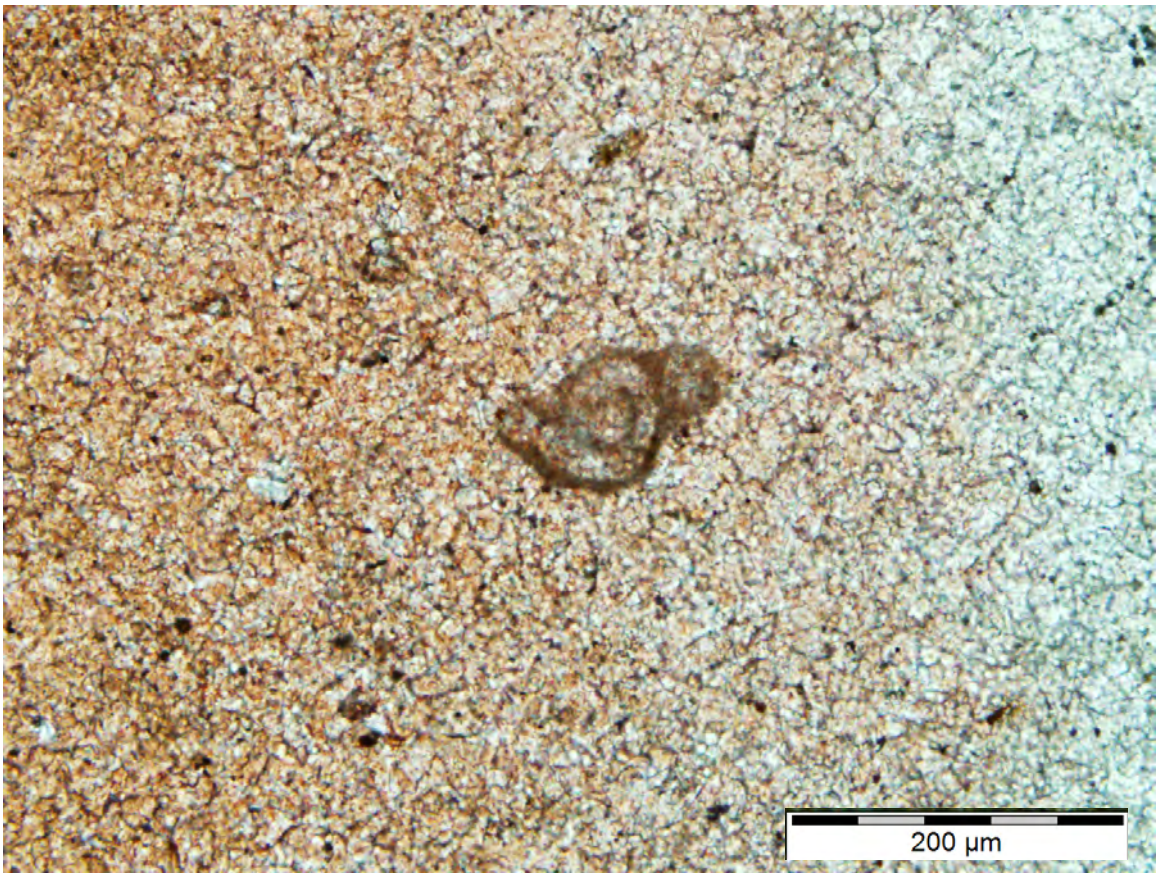

Figure 3.4: Photomicrograph taken from 62A-2.15 in plain-polarized light. Left side of slide is stained with alizarin red for calcite. Allochem in center is foraminifera.

component of samples being broken shell hash near the base of section and foraminifera at the top of the section (Fig. 3.4).

Bone Canyon

The Bone Canyon (BC) section is 208 meters of measured section in Bone Canyon, near Williams Ranch homestead (Fig. 3.5). The strata here record the proximal Bone Spring Limestone. The top of the measured section occurs at the transition into breccia of the overlying Cutoff Formation. Rocks here are yellow to grey with dark black, often petroliferous, fresh surfaces.

Observations showed mainly silty biomicrite to fossiliferous micrite with local wispy cross-laminations and platy chert stringers. Wackestone beds often interfinger near the base of the section, while the silty micrite is interbedded with shale partings

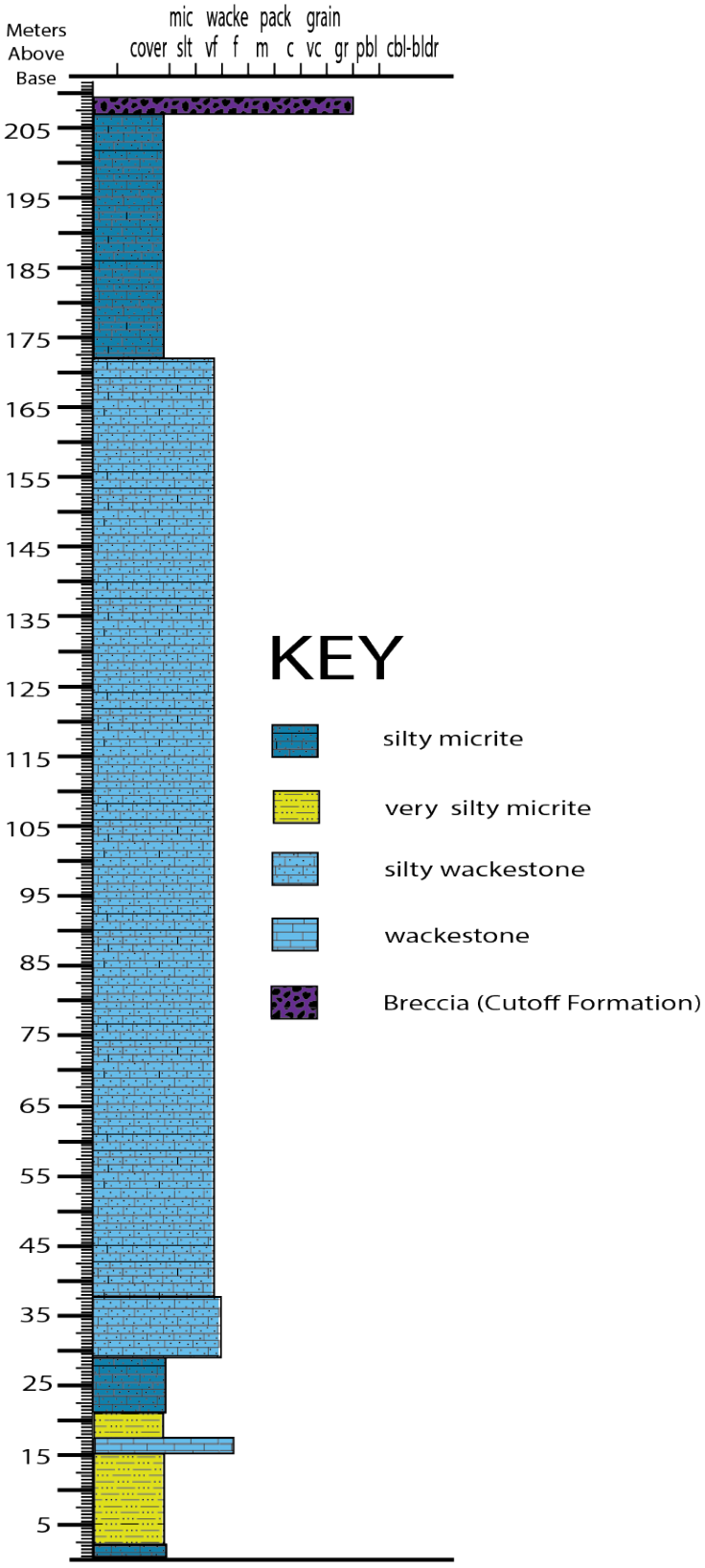

Figure 3.5: BC stratigraphic column.

frequently in the upper parts of the section. Dominant allochems were regionally consistent throughout the section: quartz extraclasts dominated near the base, broken hash dominated around the middle, and calcispheres and sponge spicules dominated at the top of the section (Fig. 3.6).

Guadalupe Liquid Canyon

The Guadalupe Liquid Canyon (GLC) section is 9.25 meters within the Cutoff Formation (Fig. 3.7). It contains light gray weathered limestone with black interior fresh surface. The section is poorly exposed beneath cover towards the top of the section.

Observations showed that the section consists of highly fractured silty fossiliferous micrite to biomicrite. Laminated beds of micrite 4-15 cm thick with sharp bases dominate. Fossils are scarce, but local wackestone occurs. A diverse variety of allochems consist of the main allochemical component for any given sample, including calcispheres, brachiopods, foraminifera, quartz extraclasts, broken hash, and sponge spicules (Fig. 3.8).

Remaining Residue Fractions Measurements

The RRF is the weight percent representing all the material remaining after samples were processed to remove calcium carbonate and organic material. Here, the volume and grain-size distribution of RRF is presented for each section. The RRF includes both detrital mineral grains and diagenetic products; thus, diagenetic minerals are recorded in the data presented. In addition, some samples contained sand-sized chert fragments, which affect grain-size distribution. Overall, these grain-size trends do correlate to the grain-sizes of detrital quartz inferred within the RRF. Each section is discussed below, ordered as proximal and distal pairs beginning with the rimmed system.

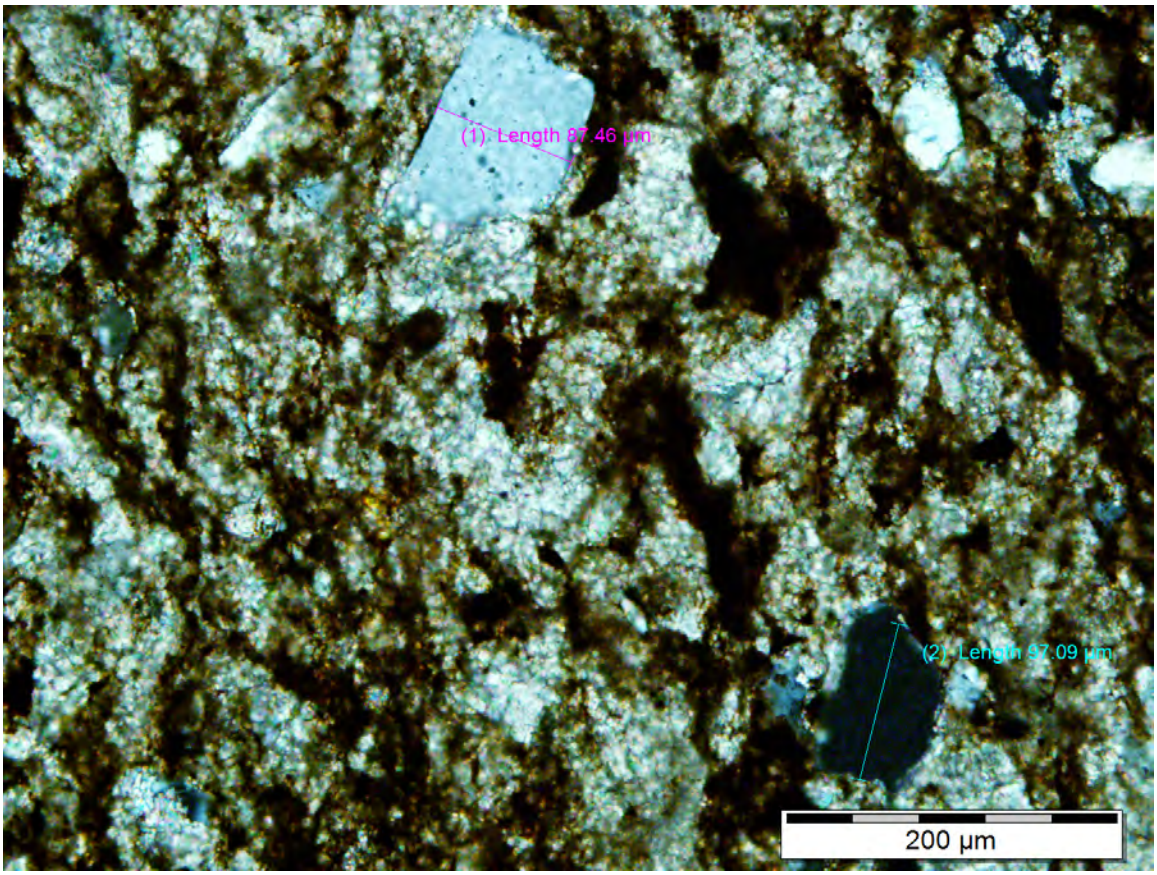

Figure 3.6: Photomicrograph taken from BC-21.4 in cross-polarized light. Quartz grains measured are sand-sized.

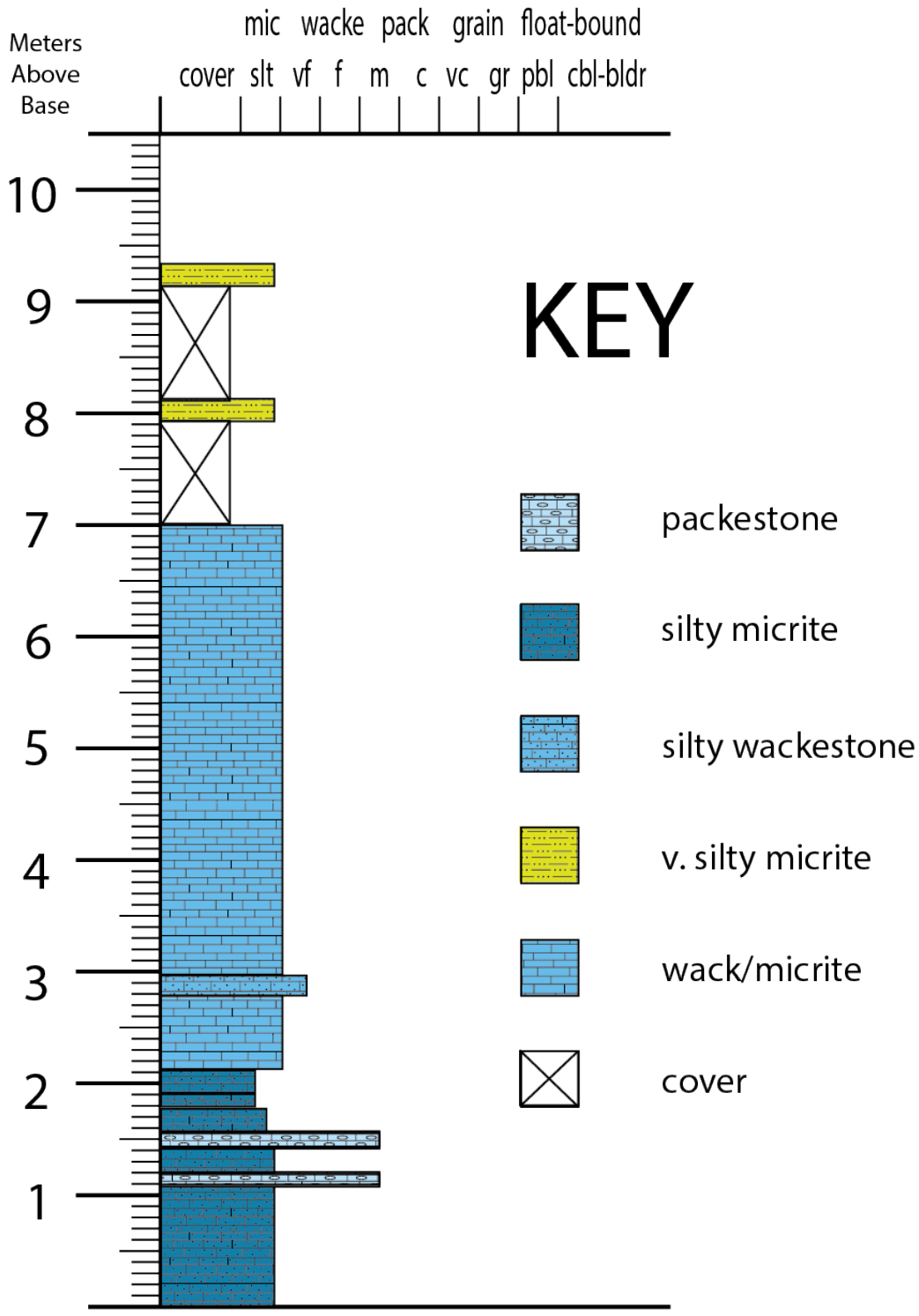

Figure 3.7: GLC stratigraphic column.

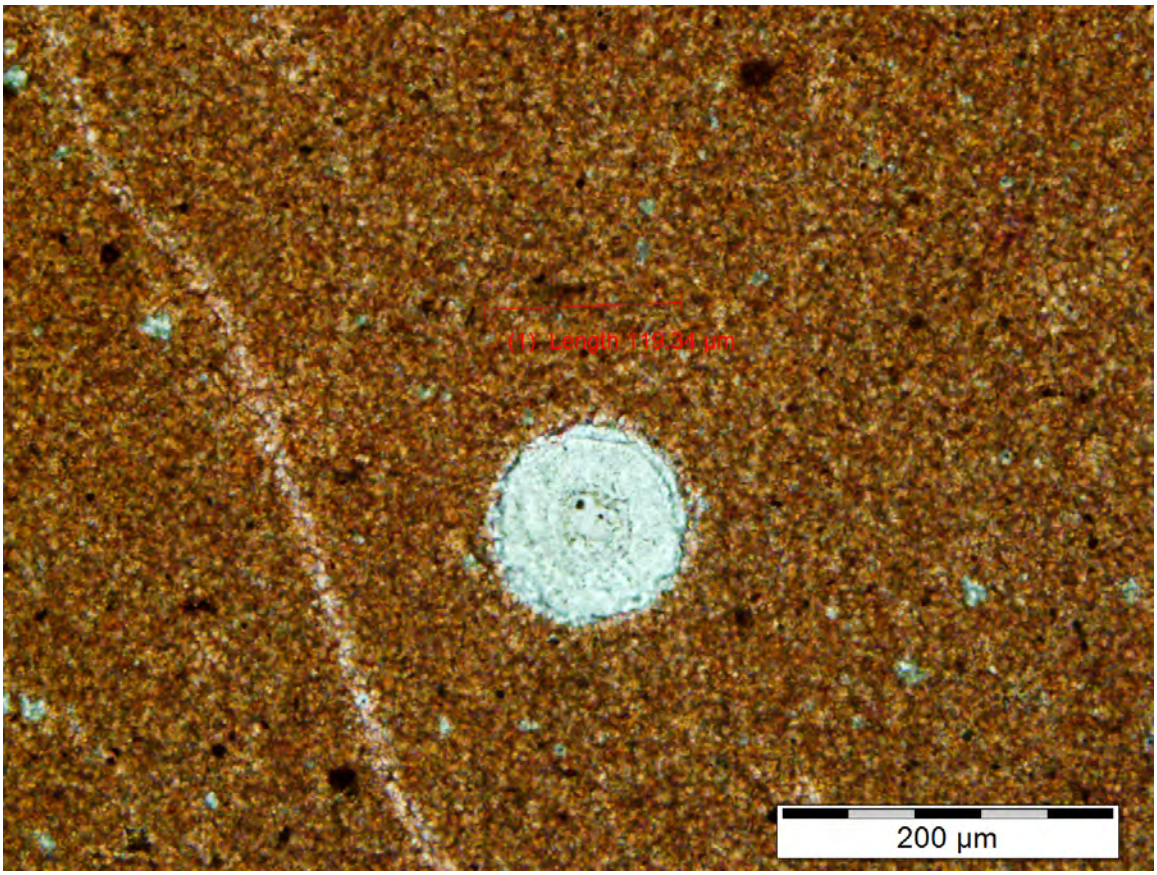

Figure 3.8: Photomicrograph taken from GLC-2.5 in plain-polarized light. Slide stained with alizarin red for calcite. Allochem is a calcisphere of unknown origin.

Lower McKittrick Canyon

The RRF from the proximal rimmed section averages 5.39% of original rock weight, with a high of 13.06%, near the top of the section, and a low of 1.81%, near the upper-middle of the section (Fig. 3.9).

Grain-size distribution for the RRF average D_{10}, D_{50}, and D_{90} values of 2.46, 11.24, and 27.27 µm, respectively (Fig. 3.10). These average values are inflated by an outlier near the top of the section, at 24 MAB. Grain-size generally increases slightly up section. Very fine sand-sized grains were only detected in the outlying 24 MAB sample, which consisted of 11.17% sand-sized volume (Fig. 3.11). Overall, sand-sized grains (>62.5 µm) consisted of 1.40% of each sample by volume. Clay-sized grains (<4 µm) decrease when moving up the section.

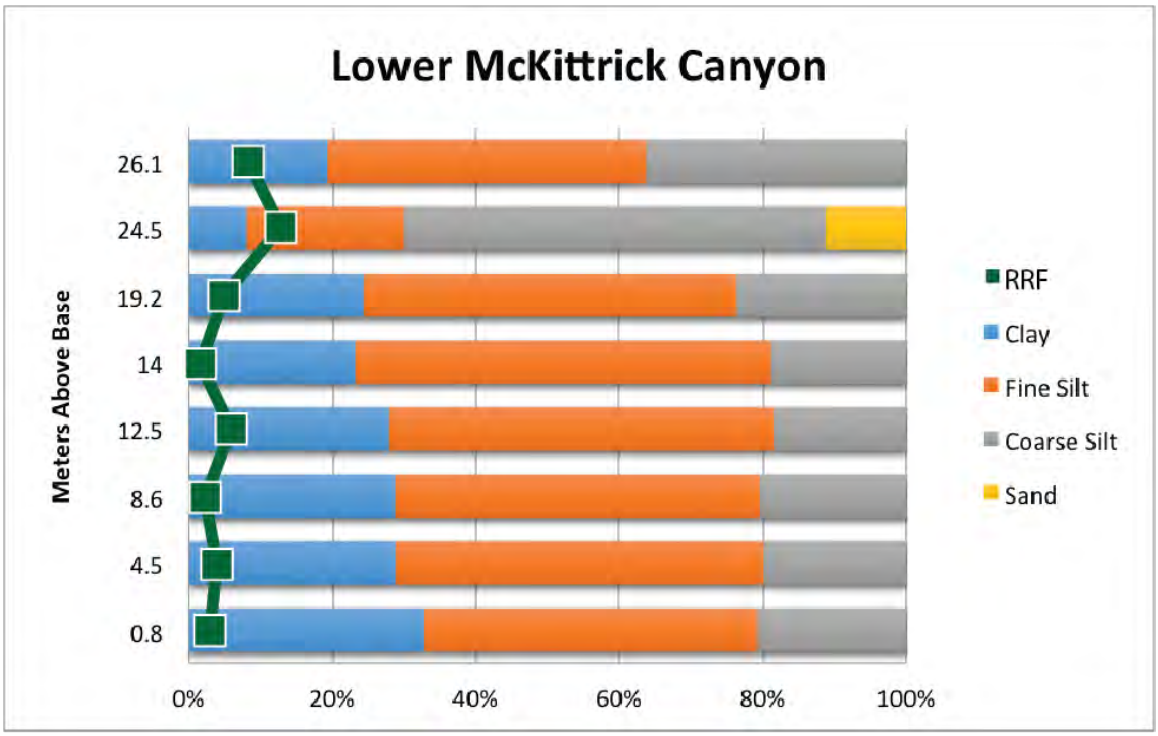

Figure 3.9: LMC RRF and grain-size distribution. RRF is shown by green line, grain-sizes are distributed into proportionate bins.

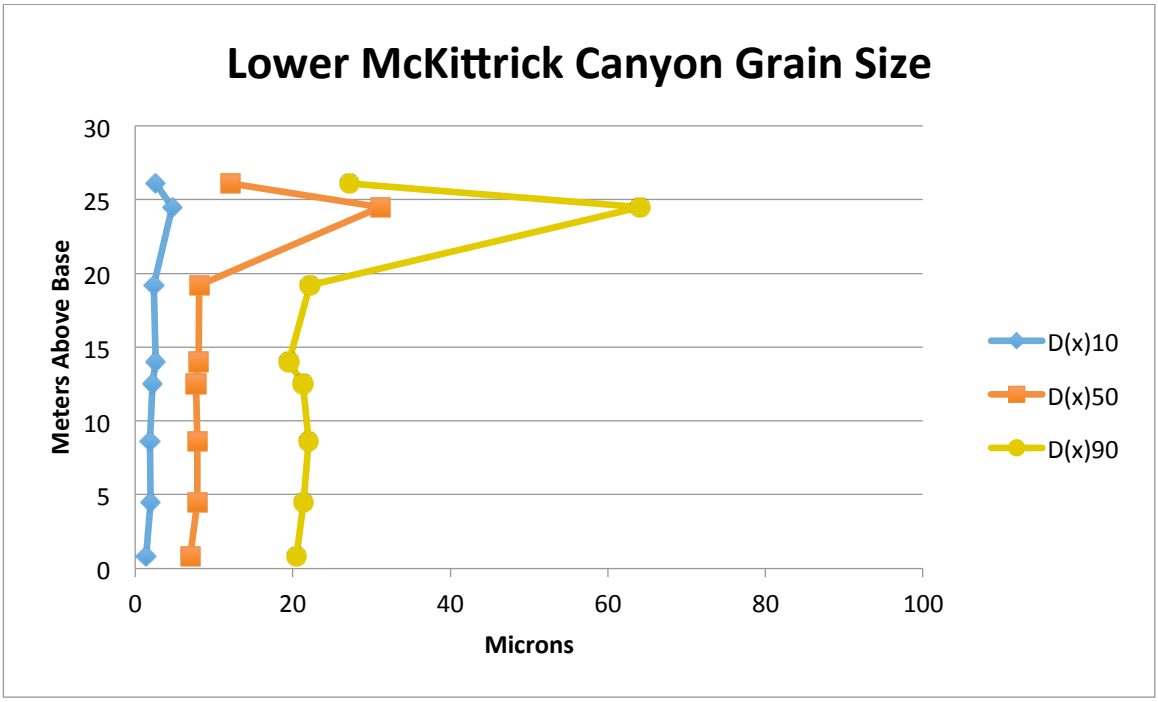

Figure 3.10: LMC fine (D_{10}), mean (D_{50}), and coarse (D_{90}) grain-sizes.

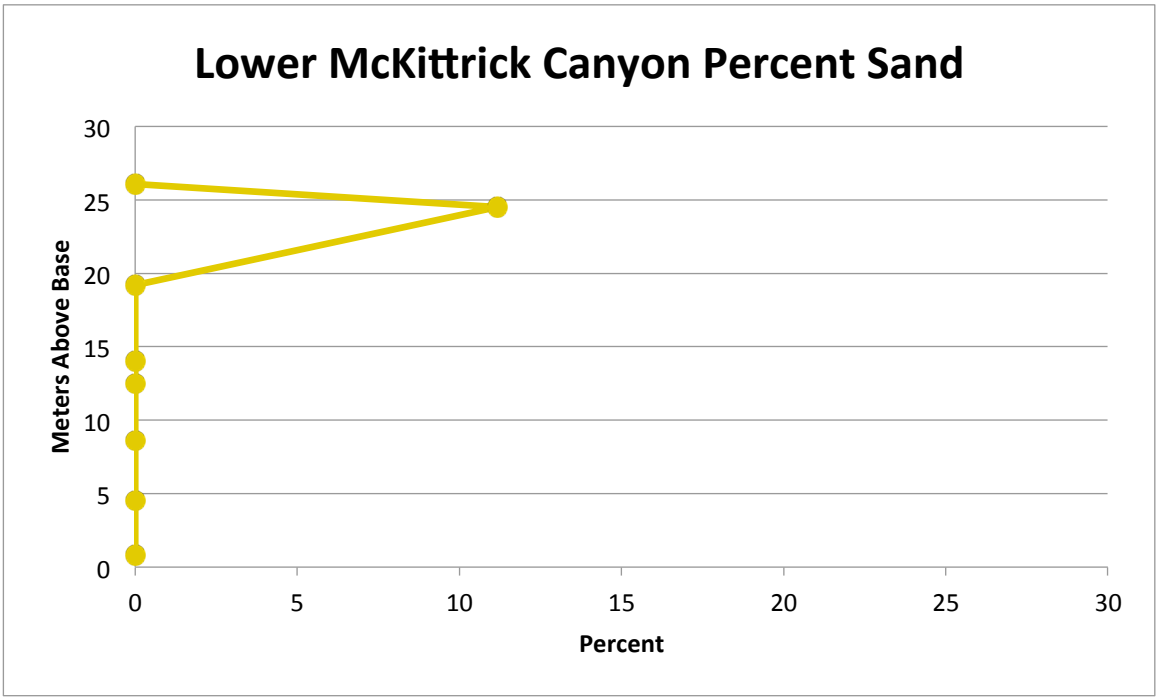

Figure 3.11: LMC percent sand, as a function of RRF.

Highway 62-A

The RRF from the distal rimmed section averages 6.50% of original rock weight, with a high of 10.31% at the top of the section, 3.45 MAB, and a low of 3.21%, near the top of the section at 2.15 MAB (Fig. 3.12).

Grain-size distribution of the RRF exhibits average D_{10}, D_{50}, and D_{90} values of 1.74, 9.73, and 35.32 µm, respectively (Fig. 3.13). Grain-size is relatively constant vertically through the entire 3.45-meter section. Very fine to fine sand-sized particles are present in each sample, and remained relatively constant by volume percent, averaging 2.43% (Fig. 3.14).

Bone Canyon

The RRF from the proximal ramp section averages 22.77% of original rock weight, with a high of 74.96%, near the top of the section and a low of 5.75%, near the upper-middle of the section (Fig. 3.15).

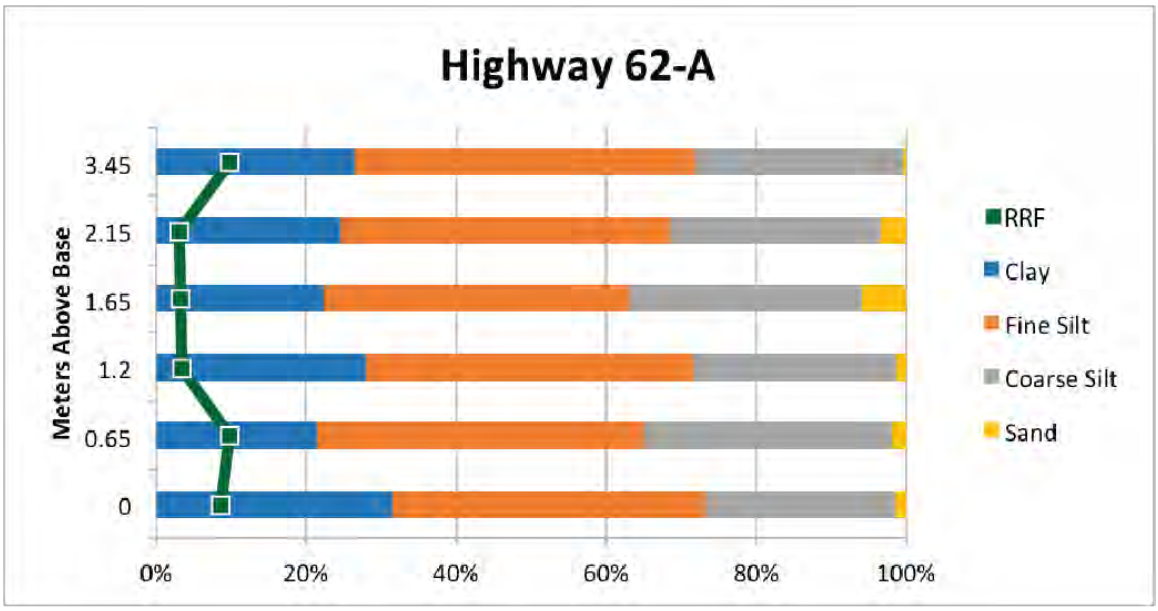

Figure 3.12: 62A RRF and grain-size distribution. RRF is shown by green line, grain-sizes are distributed into proportionate bins.

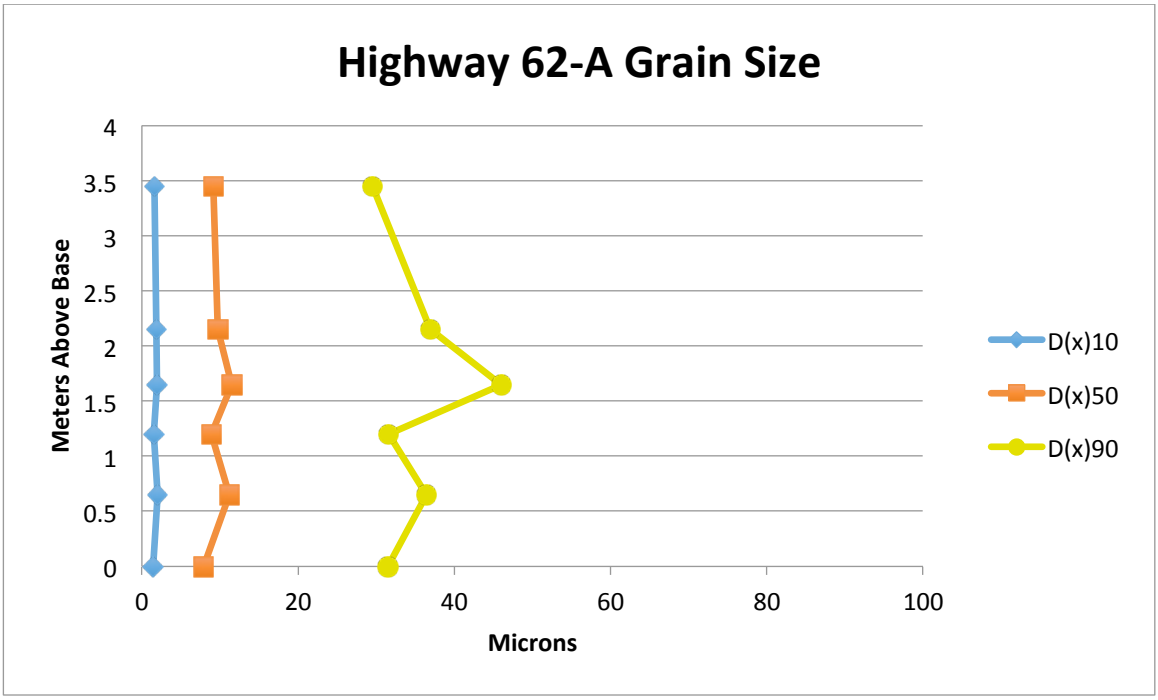

Figure 3.13: 62A fine (D_{10}), mean (D_{50}), and coarse (D_{90}) grain-sizes.

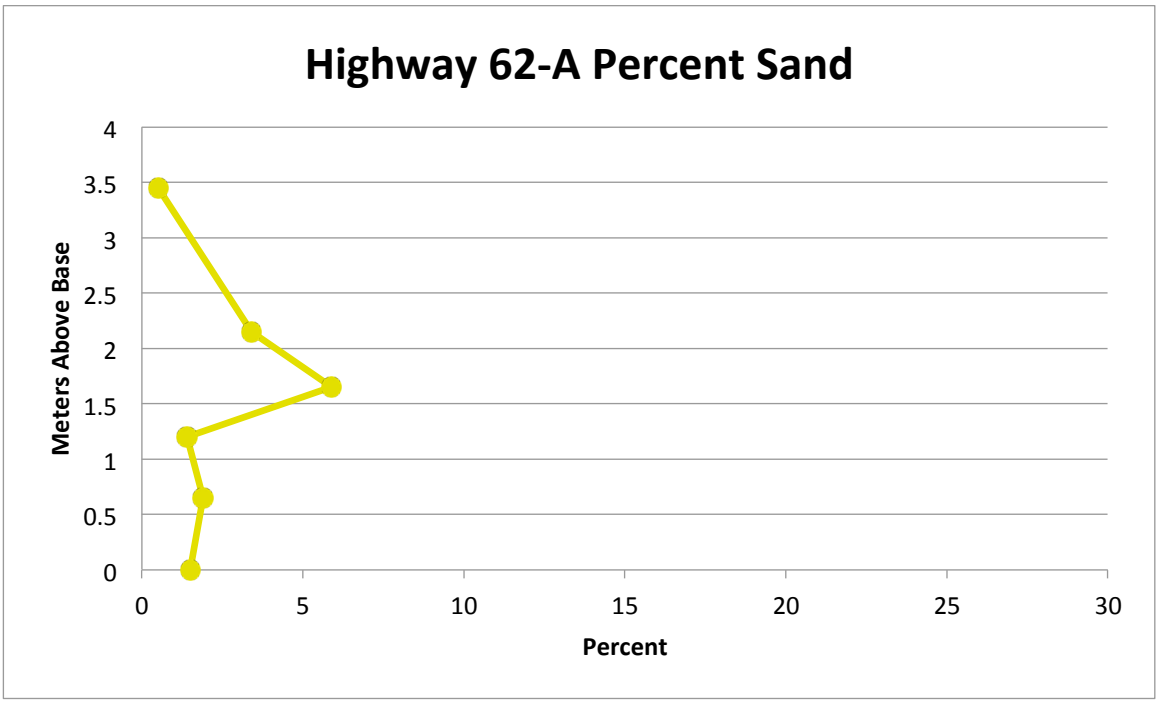

Figure 3.14: 62A percent sand, as a function of RRF.

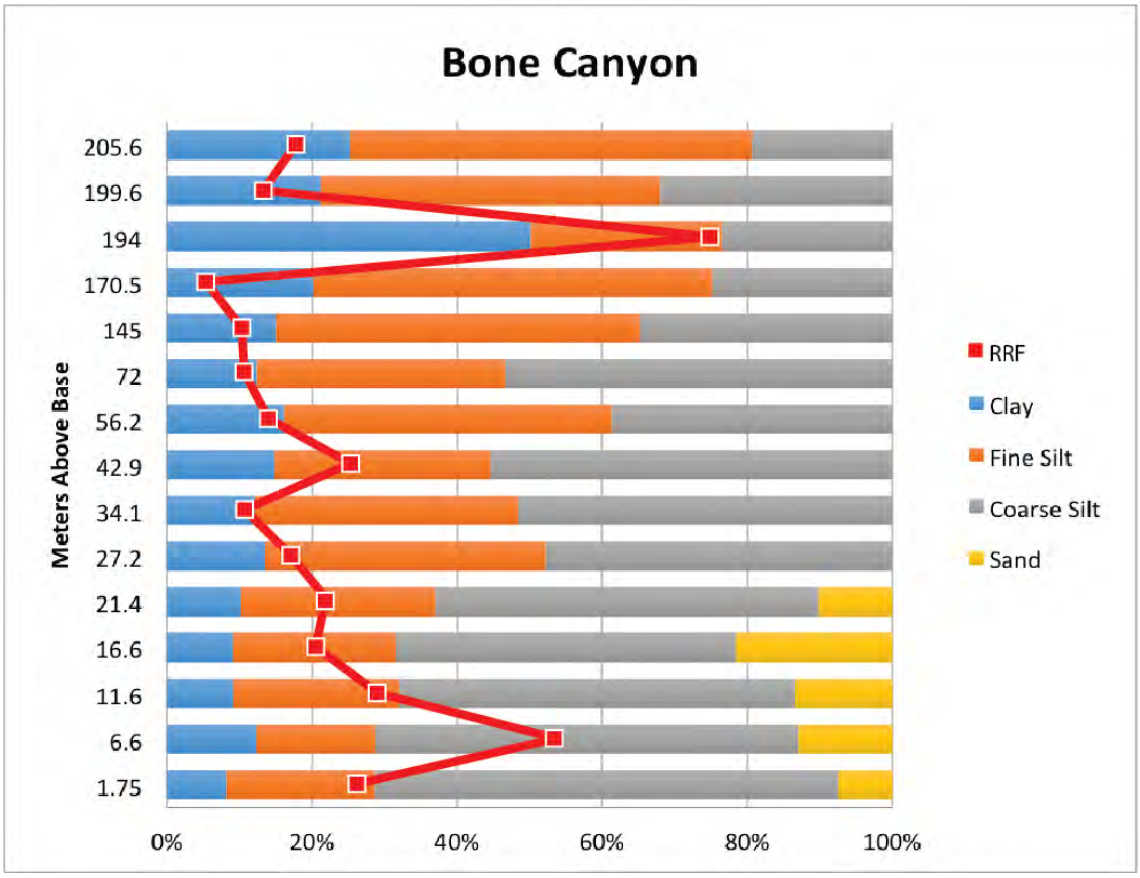

Figure 3.15: BC RRF and grain-size distribution. RRF is shown by red line, grain-sizes are distributed into proportionate bins.

Grain-size distribution for the RRF average D_{10}, D_{50}, and D_{90} values as 3.16, 17.56, and 42.68 µm, respectively (Fig. 3.16). Grain-size generally decreases when moving up the 208-meter section, and demonstrates a maximum peak at 16 MAB. Very fine to coarse sand-sized grains were detected in the lowermost five samples with the sample at 16 MAB producing over 21% sand-sized volume. Sand-size grains were not detected above 22 MAB. Overall, sand-sized grains consisted of 4.36% of each sample by volume (Fig. 3.17). Clay-sized grains increase when moving up the section. This section exhibited less clay-sized grains by average volume than any other section.

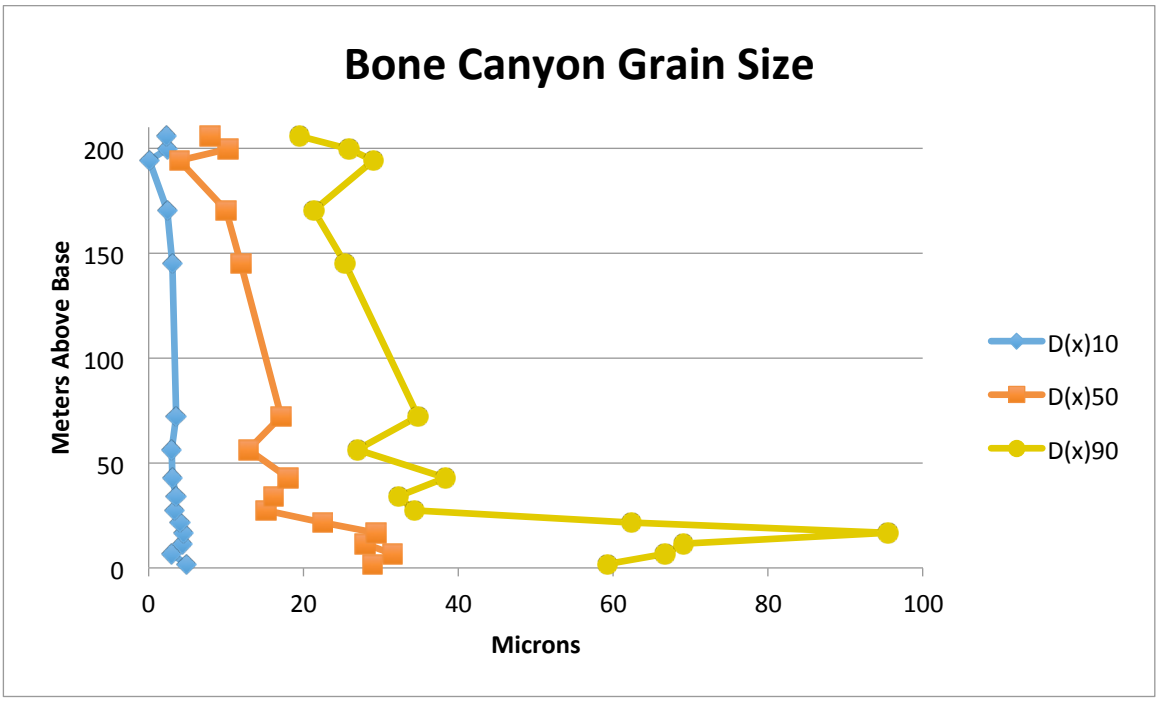

Figure 3.16: BC fine (D_{10}), mean (D_{50}), and coarse (D_{90}) grain-sizes.

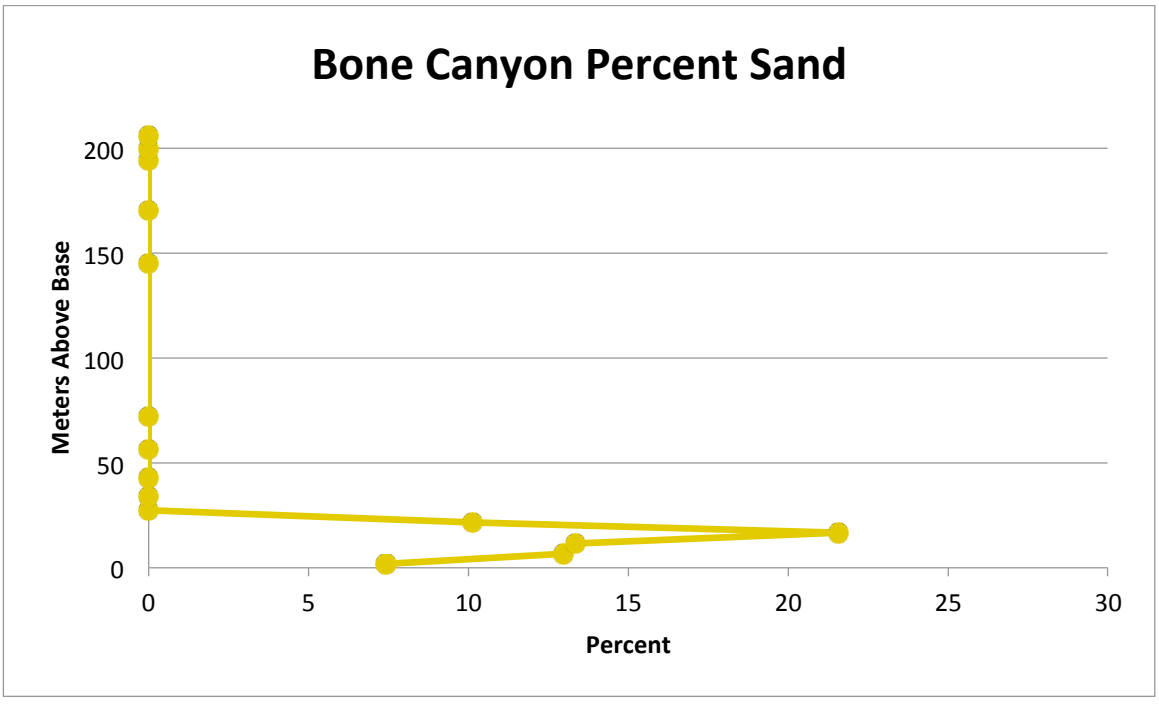

Figure 3.17: BC percent sand, as a function of RRF.

Guadalupe Liquid Canyon

The RRF from the distal ramp section averages 3.59% of original rock weight with a high of 8.18% near the top of the section, 8.0 MAB, and a low of 2.25%, near the top of the section at 6.6 MAB (Fig. 3.18).

Grain-size distribution for the RRF exhibits average D_{10}, D_{50}, and D_{90} values of 1.55, 8.37, and 27.15 μm, respectively (Fig. 3.19). Excluding a peak in the D_{90} fraction at 1.15 MAB, the grain-size generally increases upward through the section. Very fine to coarse sand-sized grains were detected in four samples distributed through the section, with the highest by volume being the 1.15 MAB sample that contained 10.60% sand-sized grains by volume. The other three samples contained less than 2% sand-sized grains by volume. Overall, sand-sized grains consisted of 1.03% of each sample by volume (Fig. 3.20), although that value is inflated by the 1.15 MAB sample. Clay-sized grains show no consistent trend when moving up the section. This section contains more clay-sized grains by average volume than any other section.

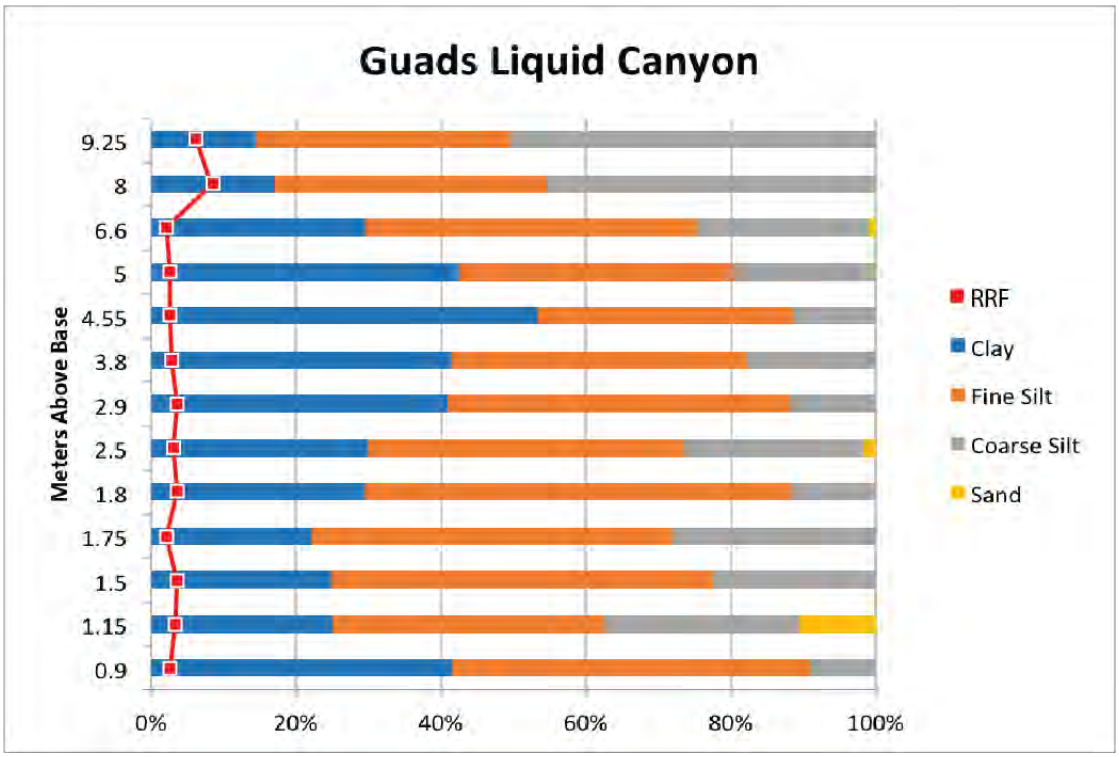

Figure 3.18: GLC RRF and grain-size distribution. RRF is shown by red line, grain-sizes are distributed into proportionate bins.

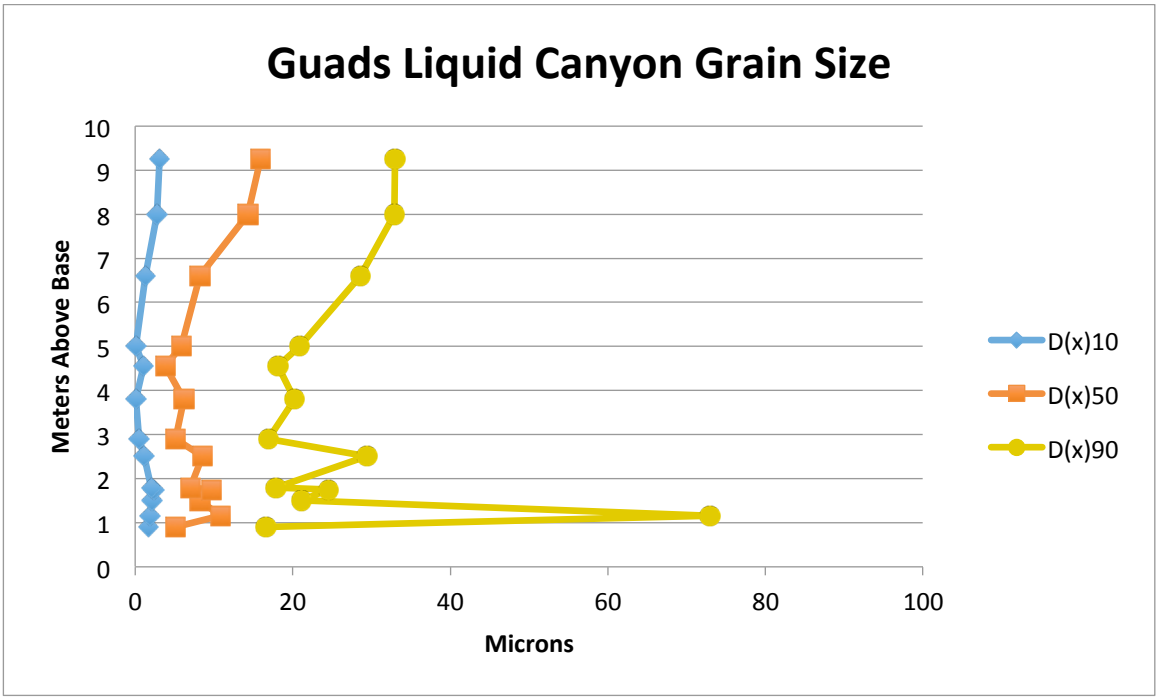

Figure 3.19: GLC fine (D_{10}), mean (D_{50}), and coarse (D_{90}) grain-sizes.

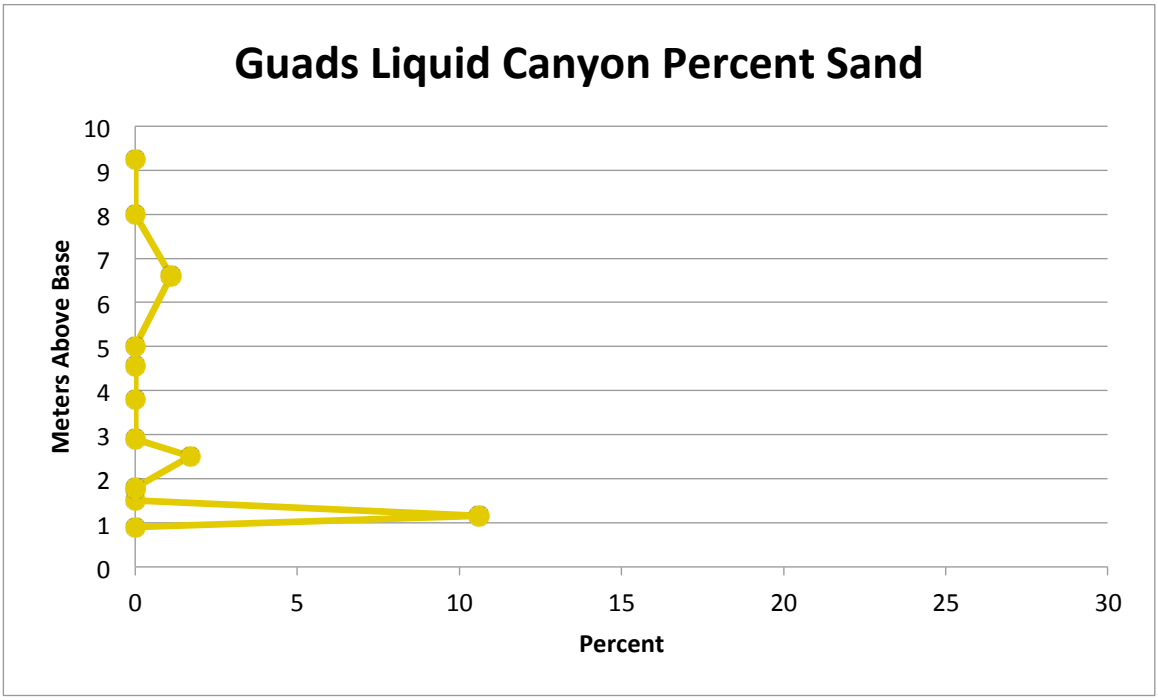

Figure 3.20: GLC percent sand, as a function of RRF.

Mineralogy of the Remaining Residue Fraction

The RRF includes both detrital mineral grains and diagenetic products. The following techniques were utilized in an attempt to reveal the percentage of the RRF that is detrital quartz grains: binocular light petrography, X-ray diffraction (XRD), and scanning electron microscopy (SEM).

Binocular Light Petrography

Binocular light microscopy was used to qualitatively assess what varieties of minerals were present in the RRF. Mineral quantities were described qualitatively as rare, present, common, or dominant as their quantity increased.

Lower McKittrick Canyon

Petrographic analysis of the coarse RRF contains common or dominant coarse silt-sized quartz grains in every sample. Very fine sand-sized quartz grains were rarely

observed, except 26.1 MAB, where they were commonly observed. Additionally, clay/quartz aggregates were the dominant component in two different samples, and uncoated silt-sized quartz grains were common in other samples. In nearly every sample, opaque iron oxide minerals were common, and mica sheets were present. No chert fragments were observed. Sponge spicules (sometimes coated by pyrite or goethite) occurred in all samples except 14.0 MAB. Translucent fluorite crystals, identified through SEM-EDS, occurred in multiple samples, but were the dominant component of the RRF at 14.0 MAB. Phosphate (apatite) minerals were common in the uppermost sample, but not observed in any other samples (Fig. 3.21).

Highway 62-A

Petrographic analysis of the coarse RRF suggested quartz was present throughout all samples from the section. Coarse silt-sized quartz grains were consistently present, as were aggregates of clay/quartz. Very fine sand-sized quartz grains were visible in rare amounts, only from two samples, 0.65-1.2 MAB. Iron oxide minerals and mica sheets were present across all samples, and sponge spicules were present but rare in most of the samples (Fig. 3.22).

Bone Canyon

Petrographic analysis of the coarse RRF showed quartz grains in every sample, often as a dominant component. Coarse silt-sized quartz grains are present in every sample except the uppermost and are dominant from 21.4-34.1 MAB. In the uppermost sample, at 205.6 MAB, where coarse silt-sized quartz grains are absent, clay/quartz aggregates are present. Very fine to fine-sand quartz grains were observed in most of the samples 170.5 MAB and below; moreover, very fine sand-sized grains were generally common and composed the dominant component of the RRF at 21.4 MAB. Iron oxide minerals were observed in most of the samples, and mica sheets were observed in over half. Sponge spicules (sometimes coated by pyrite or goethite) were also a common component in the majority of samples, especially at the base and

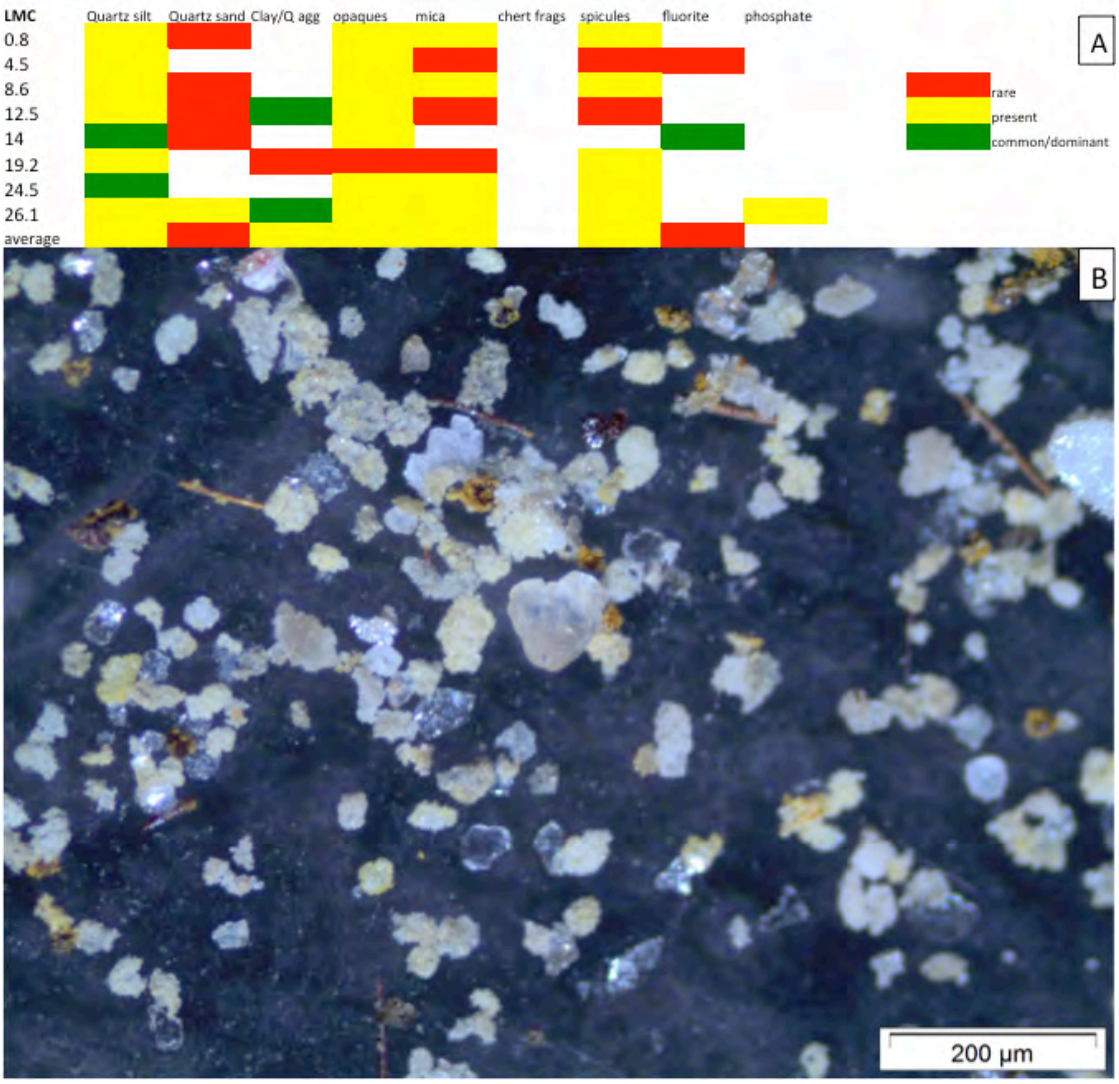

Figure 3.21: A) Mineralogy of the RRF from the Lower McKittrick Canyon section. B) Binocular light microscope image from LMC-0.8 showing sand-sized quartz grain in center, silt-sized quartz grains, quartz/clay aggregates, mica sheets, opaque iron oxide minerals, and opaque minerals coating sponge spicules.

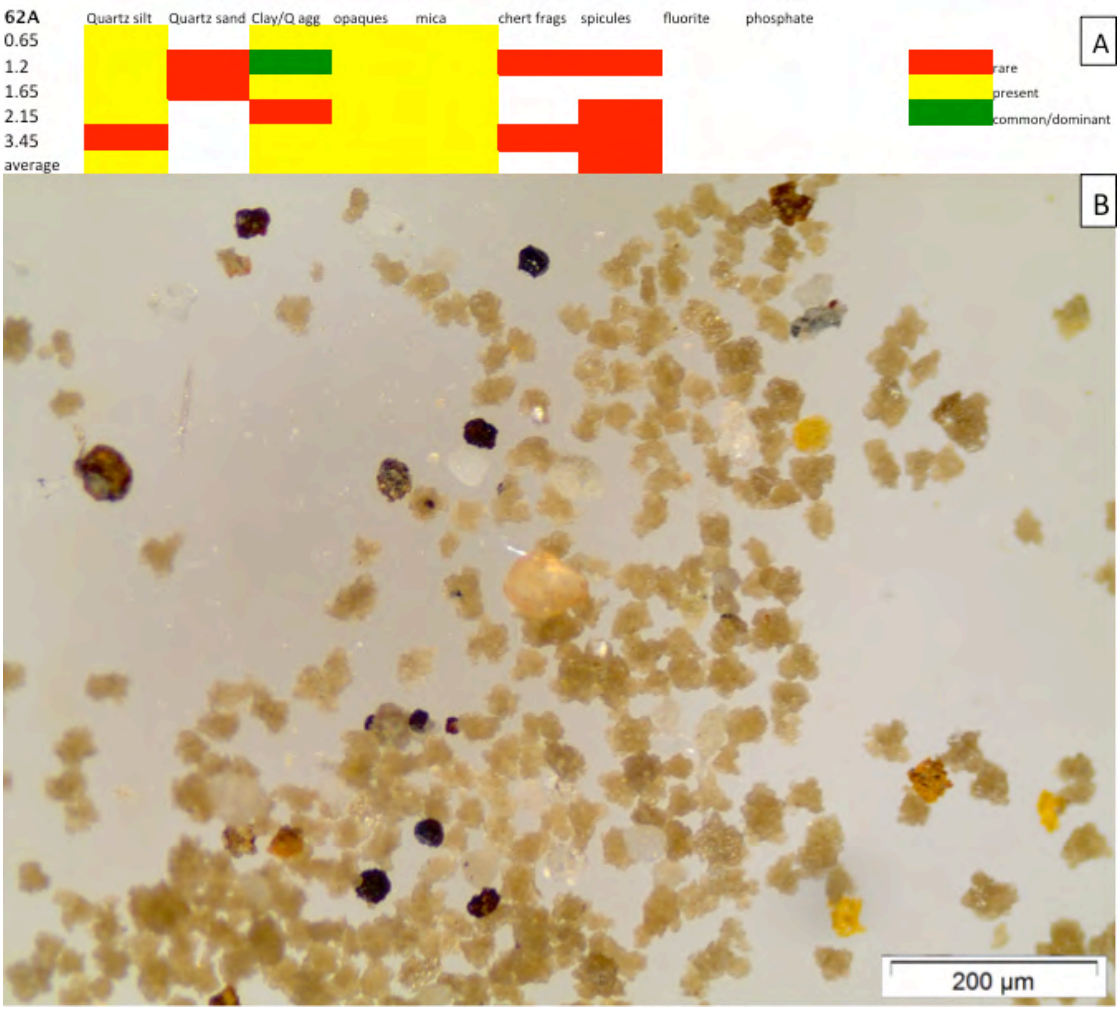

Figure 3.22: A) Mineralogy of the RRF from the Highway 62-A section. B) Binocular light microscope image from 62A-1.2 showing sand-sized quartz grain in center, silt-sized quartz grains, and opaque iron oxide minerals.

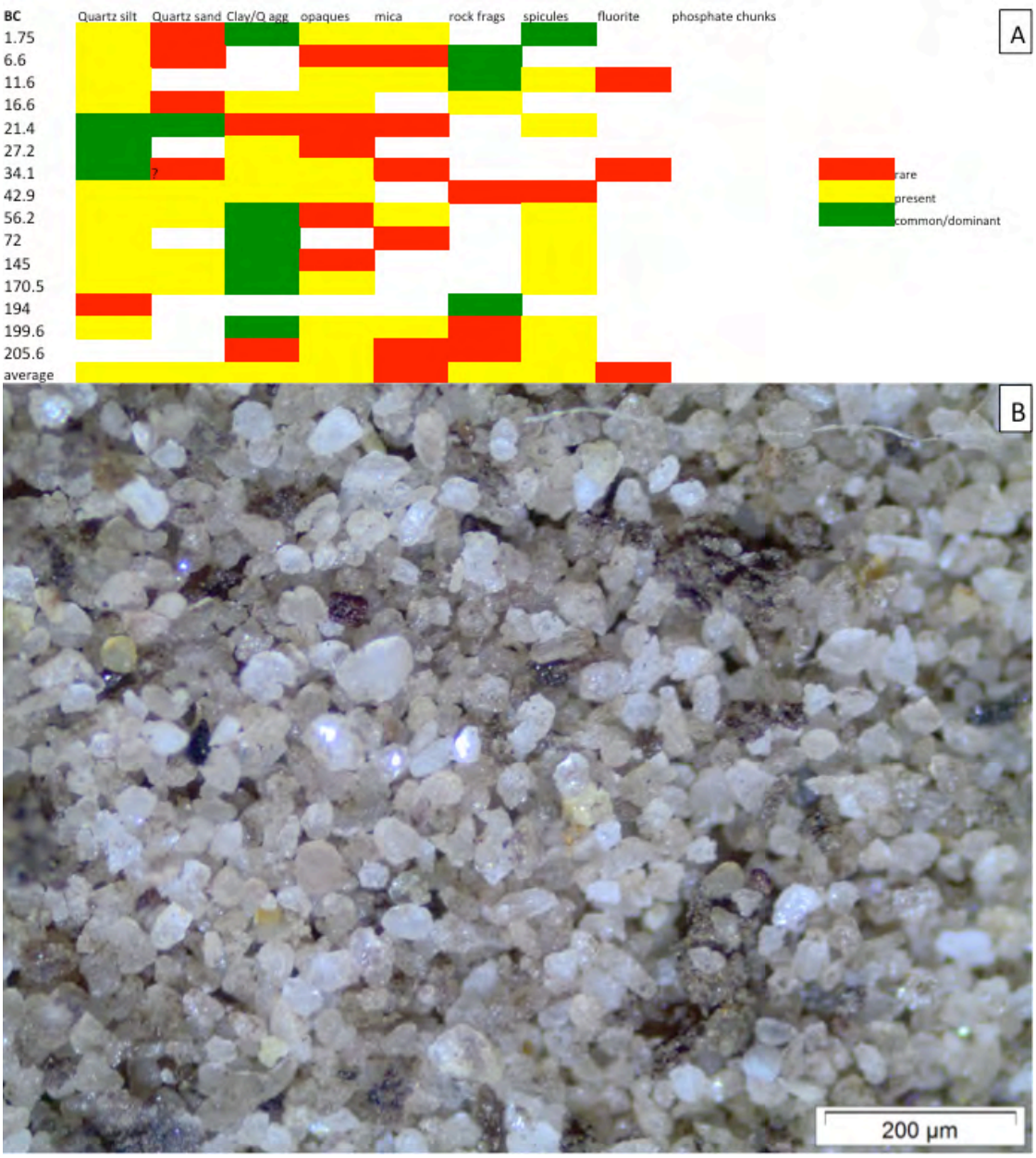

Figure 3.23: A) Mineralogy of the RRF from the Bone Canyon section. B) Binocular light microscope image from BC-21.4 showing silt to sand-sized quartz grains throughout, it addition to darker fine quartz and clay aggregates.

in the upper half of the section. Sand-sized pieces of chert fragments were a dominant component of the RRF in certain samples near the base of the section, as well (Fig. 3.23).

Guadalupe Liquid Canyon

Petrographic analysis of the coarse RRF suggested quartz grains are present in all samples in the section except for the two uppermost samples. Although these uppermost samples appeared very silty in outcrop, sample could not be completely dissolved resulting in the RRF composed only of chert fragments and spicules. Coarse silt-sized quartz grains and clay/quartz aggregates were almost always present in the RRF below 7 MAB, and were occasionally the dominant fraction of the RRF. Very fine to fine-sand quartz grains were rare to present in a few samples, at 2.5 MAB and below. Iron oxide minerals, mica sheets, phosphate minerals, and sponge spicules (sometimes coated by pyrite or goethite) were observed in most samples (Fig. 3.24).

X-Ray Diffraction

Because the RRF was typically sieved into fine and coarse fractions, XRD analysis was typically conducted on both of those fractions, except in rare cases when unsieved samples were used. In one instance, chert fragments were picked out and analyzed. Pie charts showing mineralogy from each section are shown in Figure 3.25.

The percentage of quartz in the chert fragments was not factored into the average XRD data presented for each section. Mica and illite were quantified together as a result of their structural similarity that led to practically identical diffraction patterns.

Clay-sized grains were isolated from each section and prepared for XRD analysis, as well. Analysis of these results will be reported in a later section.

Lower McKittrick Canyon

XRD results from the LMC section demonstrate that the coarse RRF averages 66.3% quartz (by weight), while the fine RRF averages 53%. The LMC section in total averages 59.7% quartz (Fig. 3.26). Fluorite (56%), not quartz (36.5%), was the dominant mineral at 14.0 MAB, which depresses the section's average quartz percentage. Removing fluorite from 14.0 MAB, LMC in total would have an average

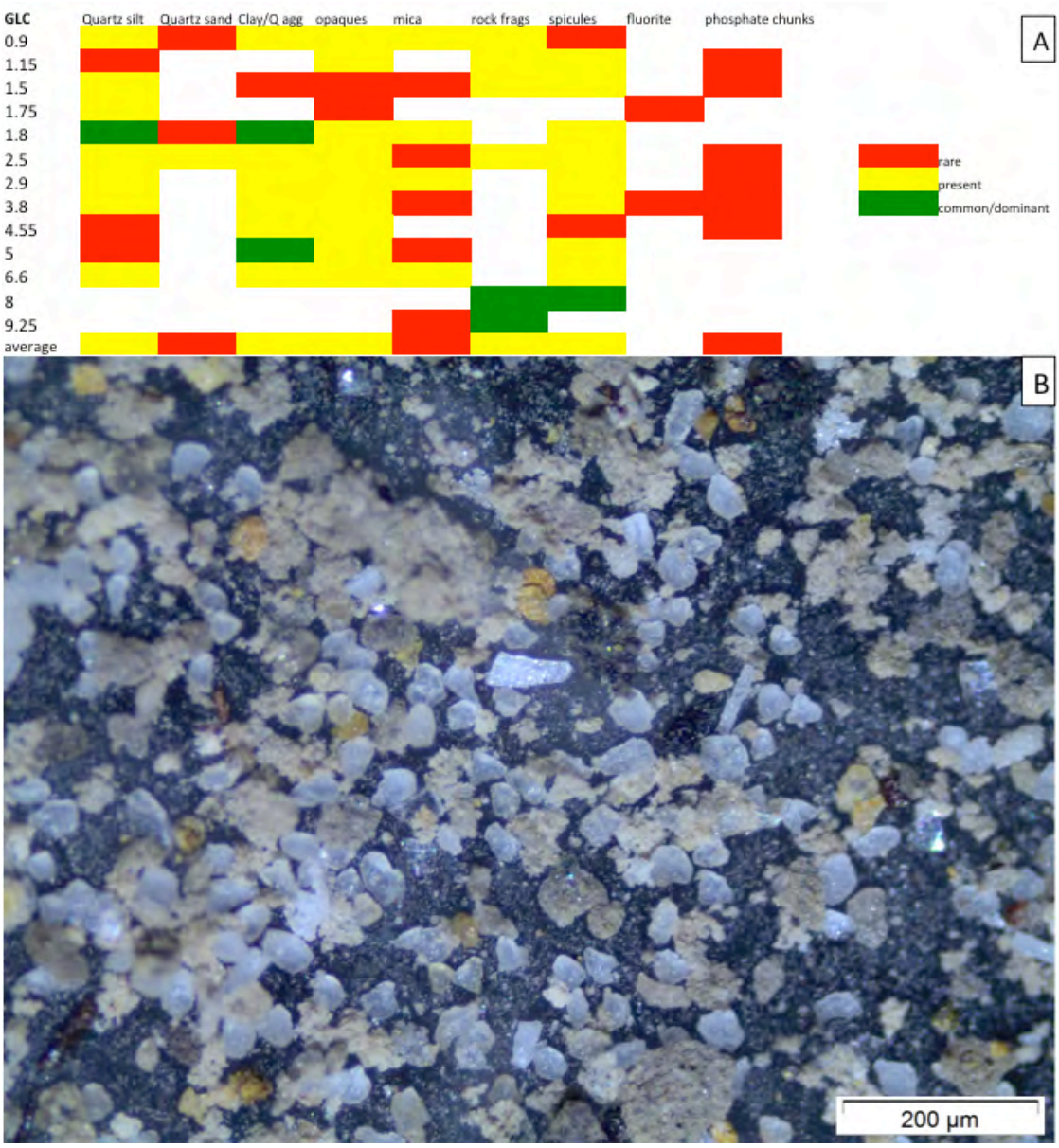

Figure 3.24: A) Mineralogy of the RRF from the Guadalupe Liquid Canyon section. B) Binocular light microscope image from GLC-1.8 showing translucent white silt to sand-sized quartz grains and tan clay/quartz aggregates present throughout, along with opaque iron oxide minerals, mica sheets, and sponge spicules.

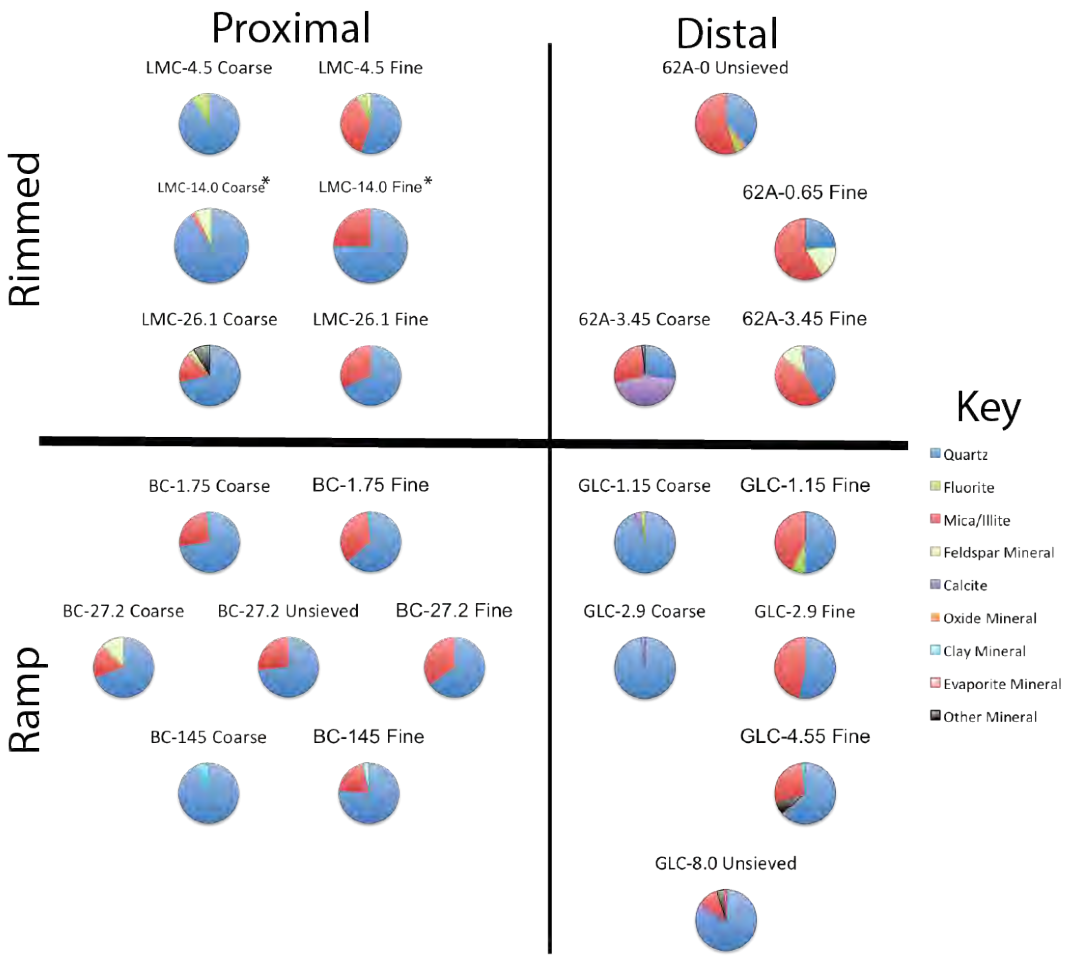

Figure 3.25: Mineralogy of the RRF broken down via pie charts representing XRD reported mineralogy for each sample. *LMC-14.0 has been normalized to remove fluorite.

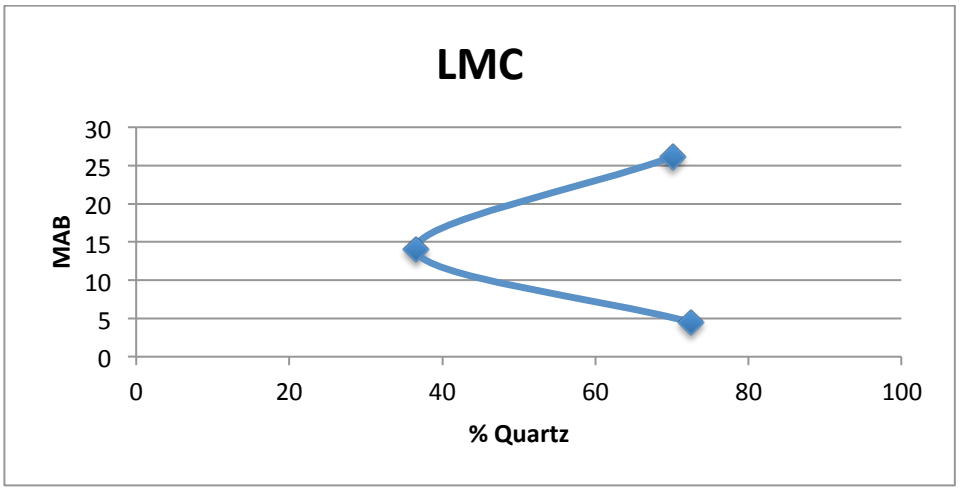

Figure 3.26: Percentage of Quartz of the RRF Throughout the LMC Section.

quartz percentage of 76.1% that is on par with BC and GLC. Fluorite is a minor component of the samples measured in LMC (4% average when excluding the 14.0 MAB sample), but was not as prominent as mica/illite (18% average). Orthoclase is also present in the coarse fractions, averaging to 2% of the RRF.

Highway 62-A

XRD analysis from 3.45 MAB demonstrates that the coarse RRF is 26.8% quartz. All fine RRF samples average to 32.5% quartz. Unsieved RRF from the base of the section exhibits 39% quartz (Fig. 3.27). This section in total averages 32.8% quartz, by far the lowest of the four sections. The other dominant mineral components are mica/illite (44% average), and albite (14.5% of the fine RRF). Fluorite and Fe-oxide minerals are minor constituents that appear in only one sample, both at less than 5%.

Bone Canyon

XRD results demonstrate that the coarse RRF averages 78.4% quartz, while the fine RRF averages 68.5%. Unsieved RRF from 27.2 MAB measures 73% quartz. A sample of RRF consisting of chert fragments from 16.6 MAB measures 95% quartz. This section in total (not including the chert fragments) averages 73.3% quartz (Fig.

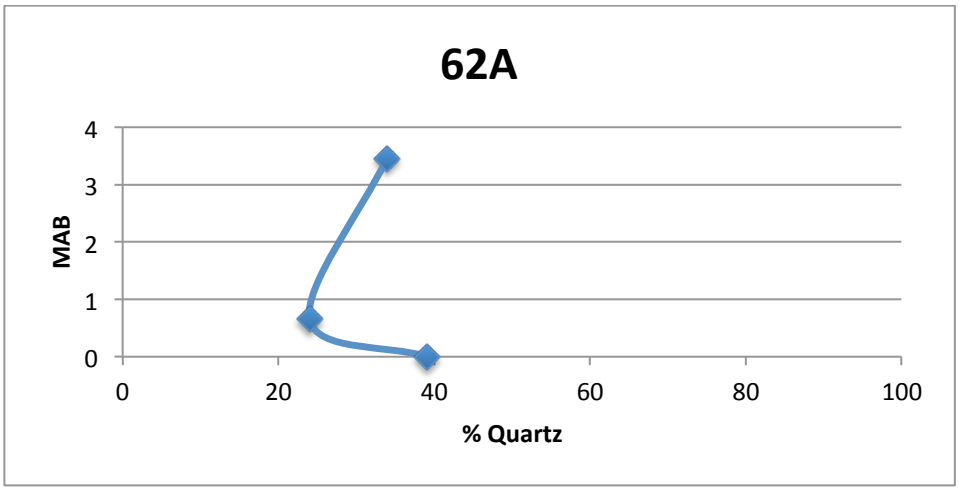

Figure 3.27: Percentage of Quartz of the RRF Throughout the 62A Section.

3.28); a value similar to GLC and normalized LMC, and well above 62A. The other dominant mineral component is mica/illite (18%), with minor constituents of albite (0-12% range) and kaolinite (0-7% range).

Guadalupe Liquid Canyon

XRD results from the lower part of the section demonstrate that the coarse RRF averages 93.15% quartz, while the fine RRF averages 53.67% quartz, both with low variability. Unsieved RRF from the top of the section averages 80% quartz. This section in total averaged 75.6% quartz (Fig. 3.29), which is very similar to the two proximal sections. The dominant component of the fine RRF besides quartz is mica/illite (37%).

Scanning Electron Microscopy EDS Data

Unknown specimens were further analyzed using SEM coupled with EDS in order to assess mineralogy, morphology, and size of grains. Presence and size of detrital quartz grains is key to interpreting the impact of coeval shelf geometry, as per the study's hypothesis.

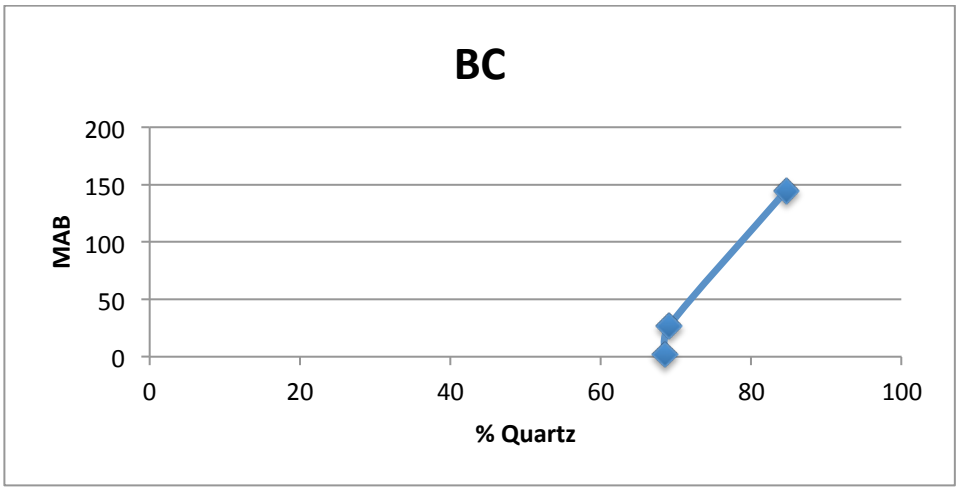

Figure 3.28: Percentage of Quartz of the RRF Throughout the BC Section.

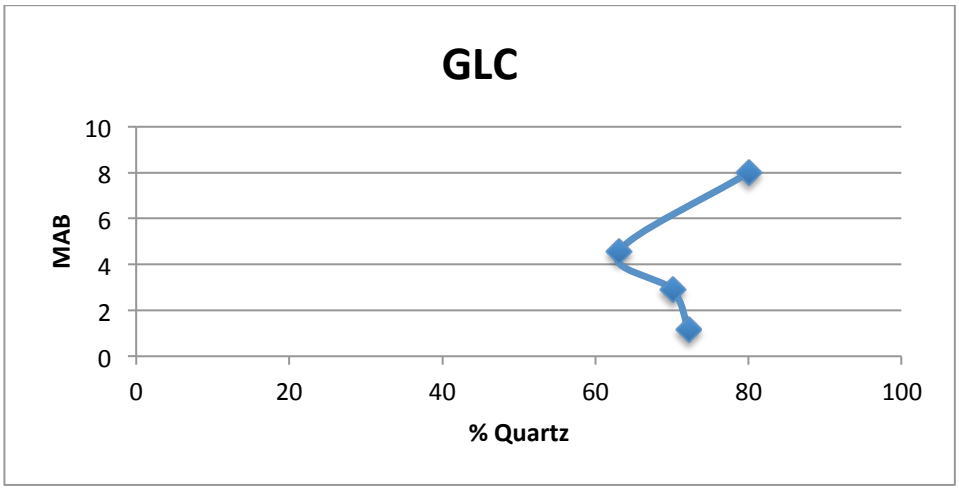

Figure 3.29: Percentage of Quartz of the RRF Throughout the GLC Section.

Quartz

Commonly, clay minerals completely coated other grains, obscuring the underlying grain mineralogy (Fig. 3.30). That underlying mineralogy is inferred as quartz because the EDS beam occasionally penetrated through a clay coating to an underlying grain (Fig. 3.31). Clay coating did not allow for original grain shape to be fully assessed, except in a few cases that are discussed later. Quartz also demonstrated euhedral crystal forms (Fig. 3.32).

Clay Minerals

X-ray diffraction of clay-sized fractions and scanning electron microscopy both show a range of smectite to illite, with mixed-layer clay minerals present, in the RRF (Table 3.1). The transformation of smectite to illite in mixed-layers is a widely known diagenetic reaction, increasing with a progressive burial (e.g., Burley, 1986). Three distinct clays appeared in EDS phase chemistry (Fig. 3.33). Clay mineral identification will be addressed in the following chapter.

Siliceous Cement and Sponge Spicules

A sample of sponge spicules was isolated from the coarse fraction of BC-1.75 for further study. Occasionally, siliceous sponge spicules demonstrated Fe-oxide or clay coating (Fig. 3.34). Chert fragment samples demonstrated spectra with silica dioxide elemental ratios (Fig. 3.35).

Other Minerals

In the LMC section, translucent minerals are reported that could not be identified with standard light petrography. EDS phase chemistry analysis determined the mineral to be fluorite (Fig. 3.36).

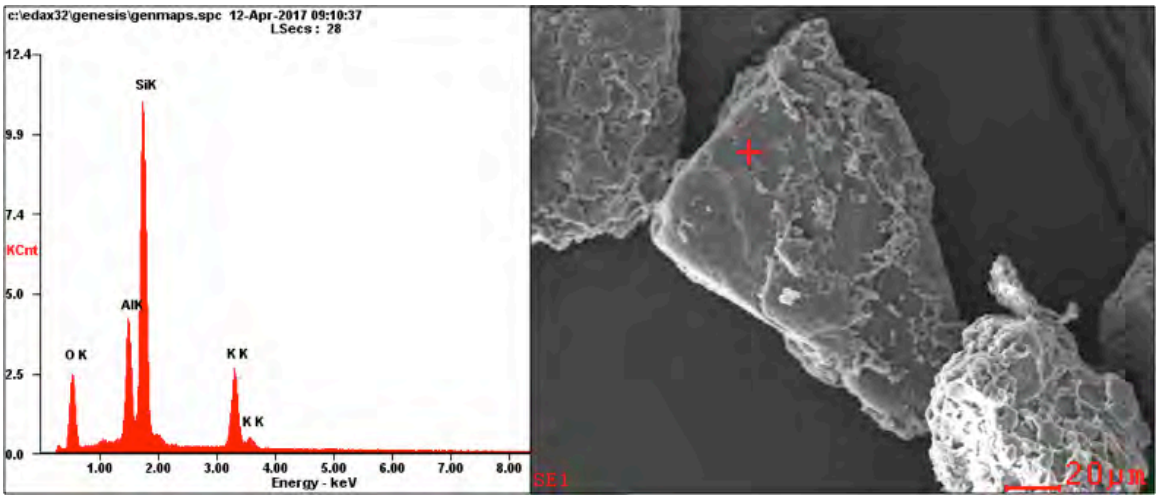

Figure 3.30: EDS spectrum and SEM image show a clay mineral coating a grain inferred as quartz.

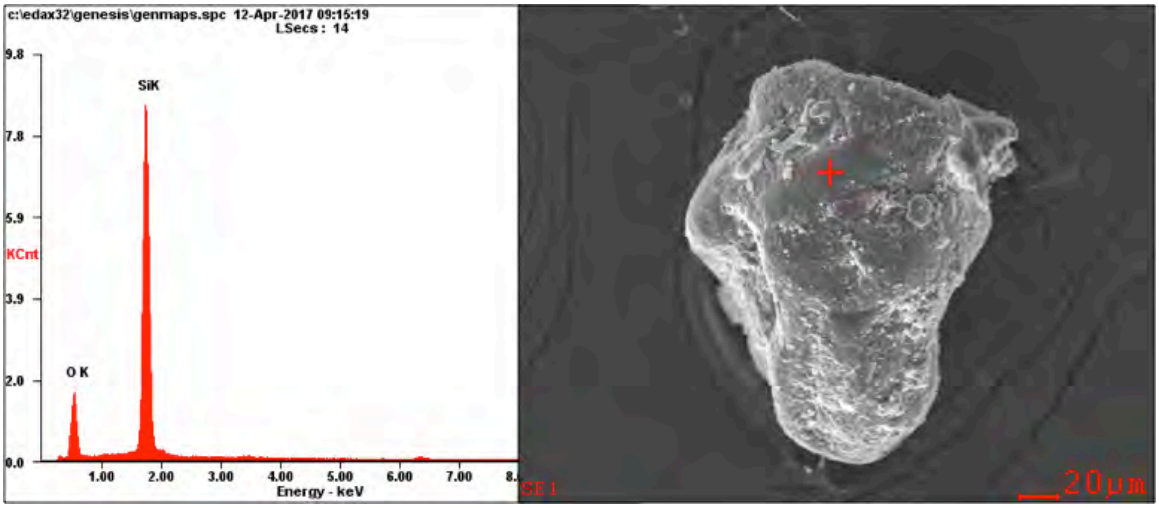

Figure 3.31: EDS spectrum and SEM image show a pure quartz grain.

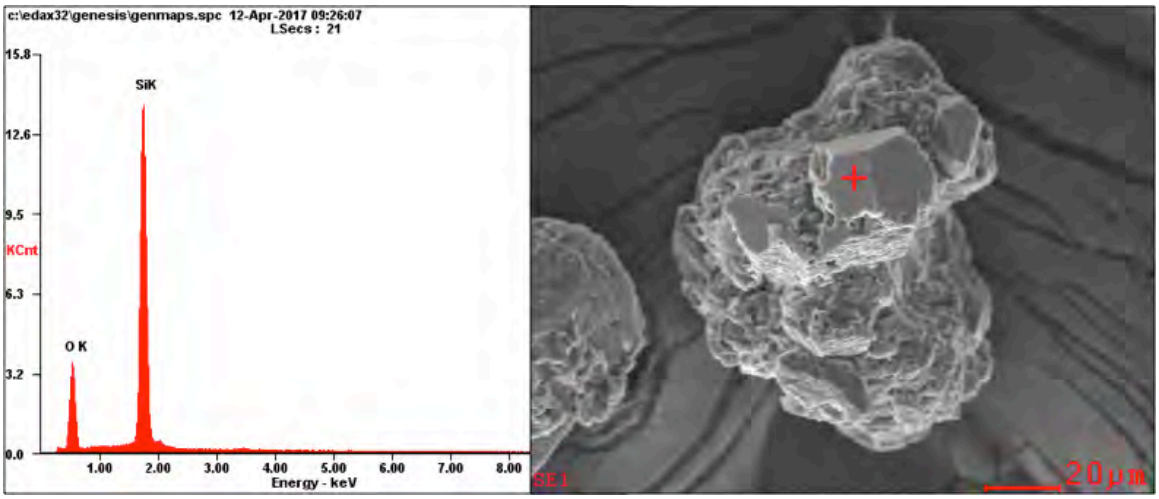

Figure 3.32: EDS spectrum and SEM image show a clearly diagenetic, euhedral quartz crystal.

Table 3.1: Elemental Breakdown of Clay Minerals From EDS Phase Chemistry

Sample	Mg	Al	Si	K	Fe	O	C	Total
GLC-0.9	0.64	23.53	30.96	9.69	0	27.62	7.28	99.72
GLC-0.9	1.31	11.5	30.27	5.5	17.55	23.26	10.61	100
GLC-0.9	0.75	10.32	43.25	6.41	15.51	10.79	7.14	94.17
GLC-0.9	1.14	17.75	40.16	7.15	0	25.51	7.8	99.51
BC-1.75	0.7	8.1	57.02	4.11	0	28.15	0	98.08
BC-1.75	0.97	10.87	47.17	4.45	7.52	29.01	0	99.99
BC-1.75	0.59	9.66	54.16	5.12	2.45	28.02	0	100

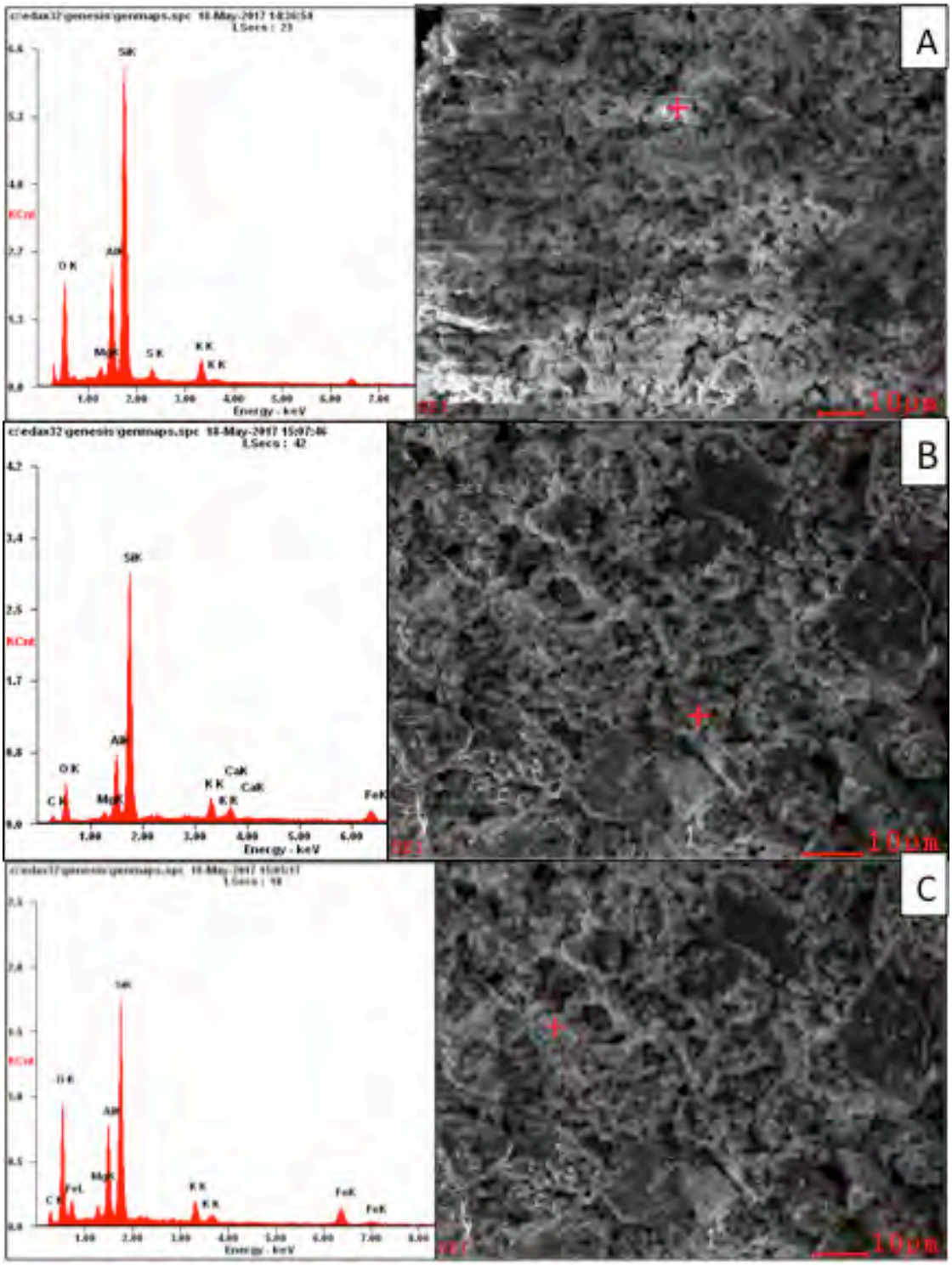

Figure 3.33: EDS spectra and SEM images of three clay minerals of different phases.

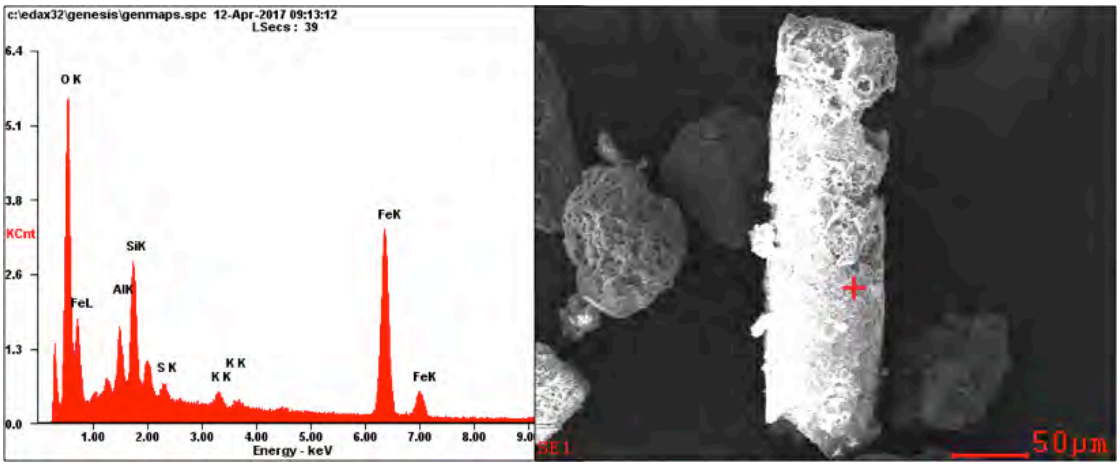

Figure 3.34: EDS spectrum and SEM image show an Fe-oxide mineral (likely goethite) coating a siliceous sponge spicule.

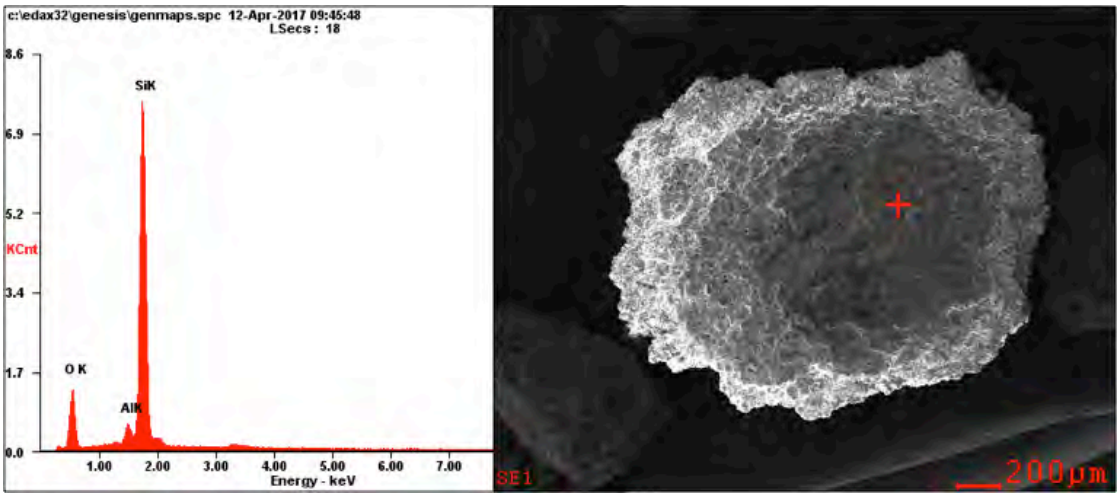

Figure 3.35: EDS spectrum and SEM image shows that incompletely dissolved rock fragments are composed of SiO_2, hence they are considered chert fragments.

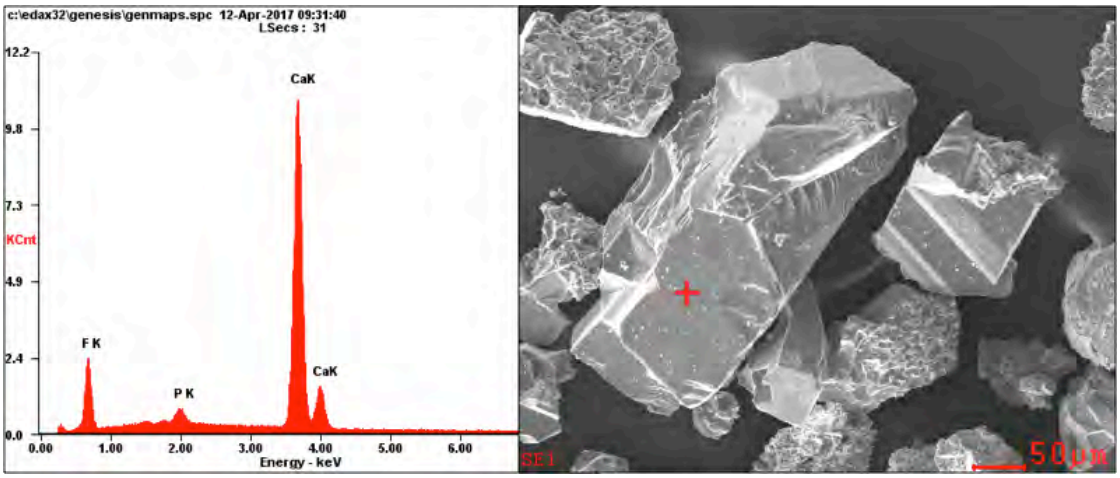

Figure 3.36: EDS spectrum and SEM image show the mineral fluorite.

CHAPTER 4

DISCUSSION

Section Correlation and Facies Interpretation

Relative sea level interpretations of the studied sections can be made based on stratal relationships at each section. For example, measurement of the Guadalupe Liquid Canyon section ended with the uppermost unit of carbonate visible, at 9.25 MAB. About twenty meters of cover later, around 30 MAB, clean sandstone suddenly outcrops. The carbonate was deposited during relative highstand, while this sandstone represents a relative lowstand deposit. Similarly, reaching the Bone Canyon section requires hiking through meters of lowstand siliciclastic-rich deposits before reaching an erosional surface that marks the switch to highstand carbonates above it (Fig. 4.1). These most basal carbonate beds represent the beginning of a relative highstand.

Fortunately, shelf and slope deposits of the Delaware basin have been studied in detail, and the stratigraphy is mostly understood. In the following sections, correlations between the proximal and distal sections coeval to a rimmed carbonate platform or carbonate ramp, respectfully, are discussed.

Guadalupian Sections

Using Tinker's (1998) facies distribution map that demonstrates proximal slope carbonate deposits coeval to a rimmed platform, the LMC section represents the Lamar Member of the Bell Canyon Formation (Fig. 4.2). Further use of Tinker's (1998) model indicates that the 62A section was sampled from either the Lamar Member or McCombs Member of the Bell Canyon Formation. Conodont or radiolarian biostratigraphy is necessary to make more constrained correlations.

Figure 4.1: These most basal carbonates of the BC section mark a change to the beginning of relative sea level highstand.

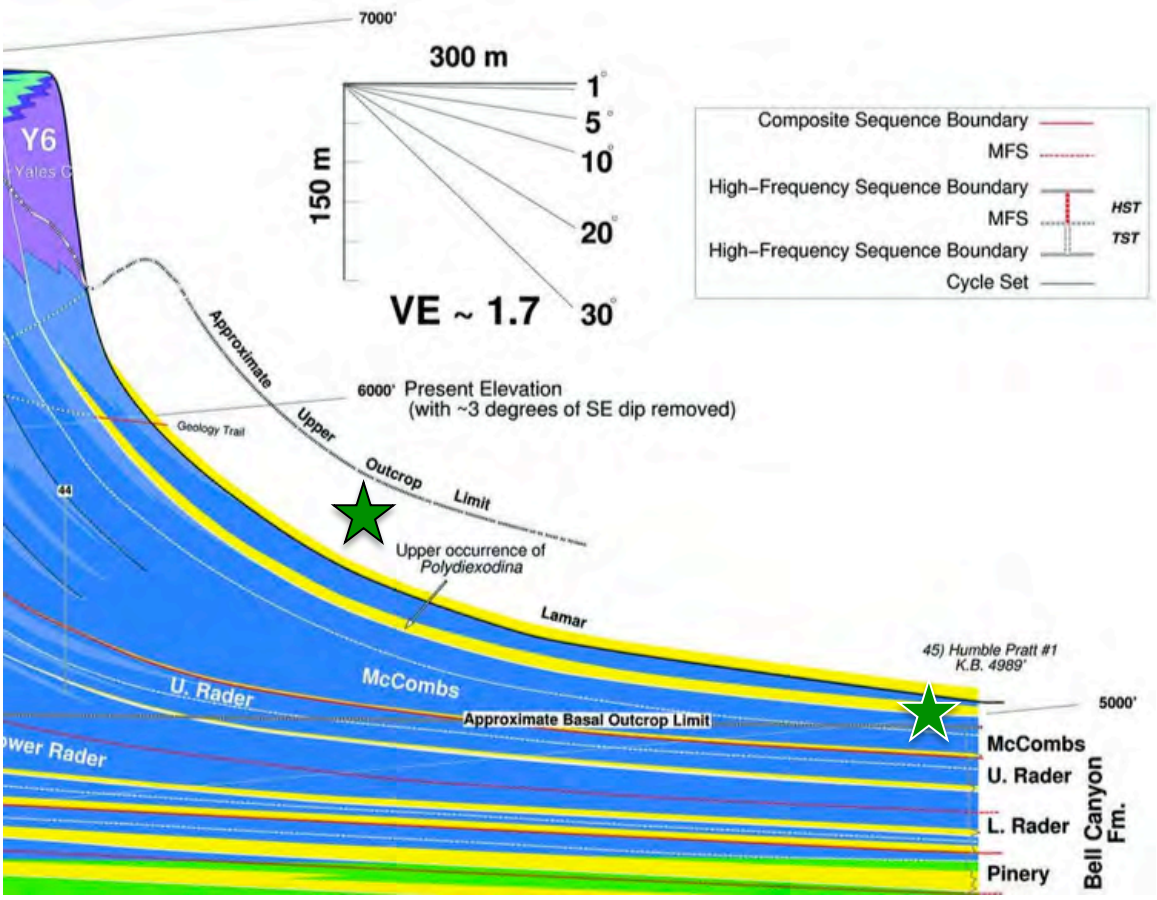

Figure 4.2: Green star with black outline shows approximate location of LMC section. Green star with white outline shows approximate location of 62A section. Modified from (Tinker, 1998).

Leonardian Sections

Stratigraphic framework in the Leonardian (and earliest Guadalupian) sections coeval to a distally steepened carbonate ramp was recently studied by Hurd et al. (2016). The proximal ramp section, measured at Bone Canyon, represents carbonate slope deposits (Fig. 4.3). Over two hundred meters of silty carbonate was measured from the Bone Spring Limestone, with the top of the section terminating at a breccia denoting the base of cycle L7 of the overlying Cutoff Formation (see Fig. 3.5). The Bone Spring Limestone projects into the subsurface to the east, as such, a coeval distal section of the Bone Spring Limestone does not crop out. Therefore, sampling was done on a section as stratigraphically low as possible. The latest Leonardian-early Guadalupian Cutoff Formation is exposed in Liquid Canyon and the lowest exposures there comprise our GLC section. The GLC section likely correlates to the G2 cycle

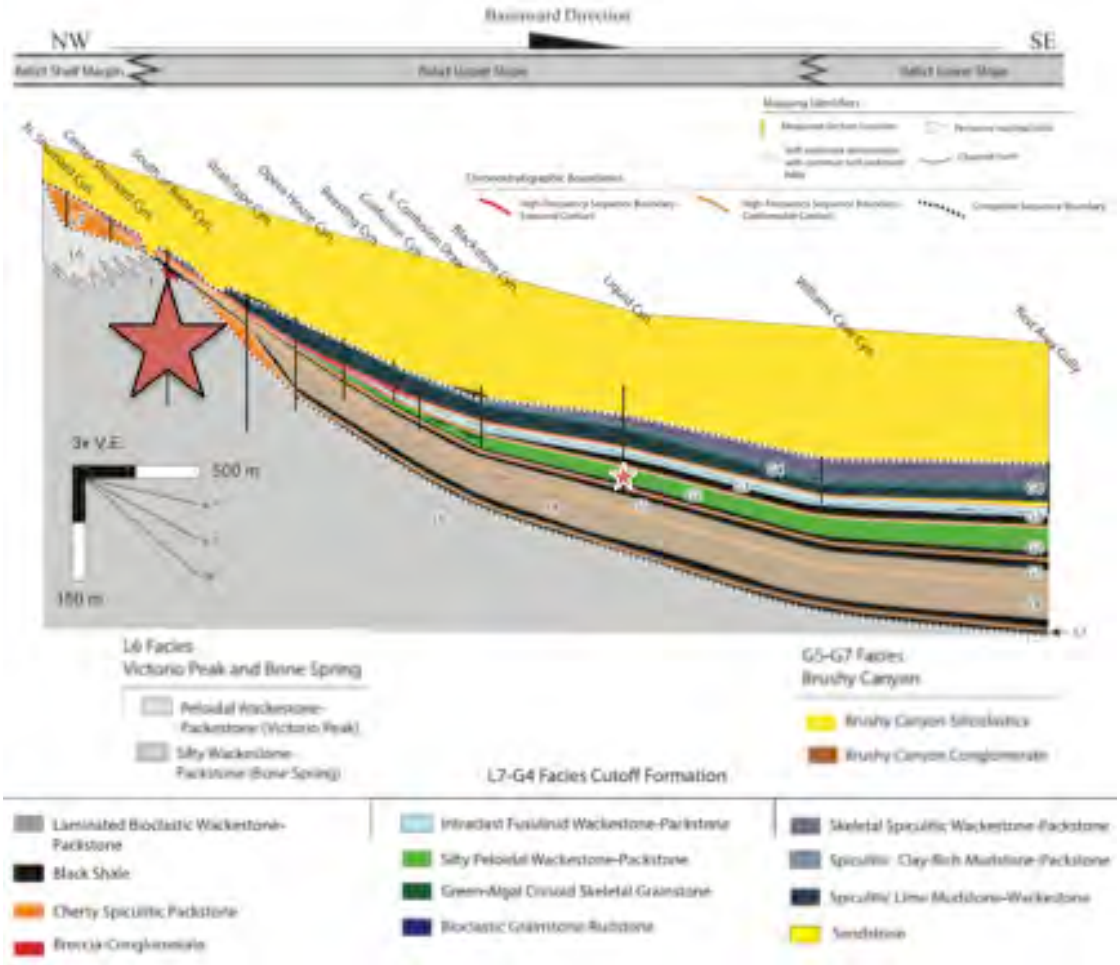

Figure 4.3: Large red star with black outline represents presumed location of BC section. Small red star with white outline represents presumed location of GLC section. Modified from (Hurd et al., 2016).

exposed in the lowest part of Liquid Canyon, where Hurd et al. (2016) also noted the high visible silt content of the carbonate strata. Figure 4.3 shows a thin layer of cherty spiculitic packstone (orange) overlying silty peloidal wackestone-packstone (green) in the G2 cycle. This cherty spiculitic packstone likely correlates to the top few meters of this study's GLC section (see Fig. 3.7).

The BC and GLC sections do not correlate; however, both Leonardian sections were deposited on a similar distally steepened carbonate ramp system, and can be compared to their Guadalupian equivalents to determine the impact of shelf geometry on presence of siliciclastic sediments in slope and basinal carbonate deposits.

Completeness of Sections

The fining upward sequence shown in the Bone Canyon section is typical of deepening upward deposits, which fits the greater sea level trend of the Permian. When looking at the BC section, it is noticeable that the majority of the RRF stems from its high siliciclastic content near the base (see Figs. 3.5, 3.15-3.17). It is possible that this shallower part of the highstand was not sampled from other sections, providing another variable that allows BC to have the highest RRF. However, this is unlikely based on two observations. Firstly, the LMC and GLC sections were sampled from the most basal carbonate deposits present in each canyon. In these sections, those most basal carbonate deposits were not any more siliciclastic rich than the rest of the section. The 62A section was a road-cut outcrop, which makes it impossible to know whether or not the base of section actually represents the most basal carbonate or not. It appears this trend is more likely inherent to the BC section than it was missed in all the other sections. Secondly, the average RRF of the BC section 56.2 MAB and above (not including the outlying 194 MAB sample) is 12%. Although this is substantially lower than the BC section as a whole and its basal samples, 12% RRF is still twice as high as any other section's RRF.

Biogenic, Diagenetic, and Detrital Components of the RRF

In order to address the hypothesis, it is necessary to determine the detrital component of the RRF. The RRF is composed of biogenic, diagenetic, and detrital components. Partitioning the RRF into these three components is challenging. This section discusses quantitative and qualitative data that attempts to unravel the detrital and diagenetic components of the RRF.

Biogenic Products

The biogenic component of the RRF was produced by the fauna living near the shelfal slope. These fauna include siliceous sponges and conodonts. Preserved fauna

with carbonate or apatite skeletons would have been mostly, if not completely, dissolved during processing, and therefore are not part of the RRF.

Sponge Spicules

Sponge spicules contribute to the RRF weight percent, and to the percentage of quartz that was determined using quantitative X-ray diffraction. The latter was confirmed by analyzing sponge spicules taken from the BC-1.75 sample with XRD (Fig. 4.4).

In total, sponge spicules compose no more than 10% of the total RRF weight percent of each section. Added weight from sponge spicules is not significant enough to affect RRF interpretation, especially since there is no evidence that the RRF from a section contains more or less sponge spicules than any others.

Sponge spicules initially precipitate as biogenic amorphous silica (opal-A). As diagenesis takes place opal-A gradually evolves into cristobalite and/or tridymite (opal-CT), and with continued diagenesis opal-CT converts to cryptocrystalline quartz and eventually to microcrystalline quartz (Williams and Crerar, 1985). Our results show that the sediment reached a high enough burial temperature to convert most of the original biogenic marine silica to crystalline quartz.

Though never proportionally quantified from the RRF, sponge spicules were rarely a major component. Only two samples had sponge spicules considered as a "common/dominant" component: GLC-8.0 (near the top of the section) and BC-1.75 (near the base of the section). However, spicules did occur in many of the other samples. Nevertheless, the amount of spicules in a sample did not largely affect the XRD quartz quantification, nor did it affect the relative interpretations of RRF weight percent between the sections. This can especially be argued since there is no major difference in sponge spicule abundance between the four sections studied.

Metastable sponge spicules are relatively easily dissolvable before the end of their diagenesis sequence, which would have freed silica ions to possibly recrystallize nearby. This may be a likely mechanism for precipitation of siliceous "cherty" cement, or quartz overgrowths, that were found in numerous samples. Fine silt-sized quartz

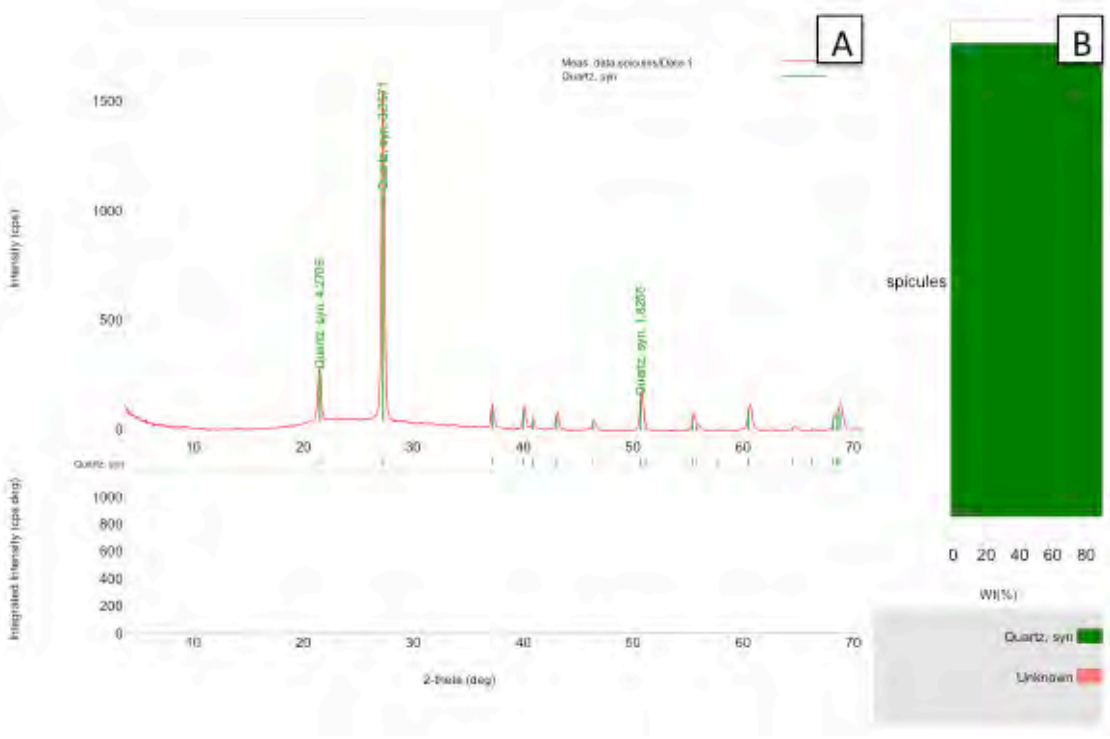

Figure 4.4: A) The XRD spectrum shown for spicules isolated from BC-1.75 matches perfectly with a standard quartz spectrum. B) Quartz was quantified as 100% of the samples mineralogy.

grains are also known to dissolve in carbonate and mobilize into chert nodules (Cecil, 2015). Incompletely dissolved rock fragments were confirmed as siliceous by both XRD and SEM-EDS analysis, and likely indicate chert-rich rock fragments.

Apatite

Apatite was observed in a few samples, only in small quantities, and likely represents conodont fragments. However, given the relative small contributions to the RRF, the proportion of apatite is not further considered.

Diagenetic Products

Numerous minerals are present in the RRF that are considered to be diagenetic products, including phyllosilicates, Fe-oxides, pyrite, and fluorite.

Iron Oxides and Pyrite

Fe-oxide and pyrite were observed with binocular microscopy as either discrete crystals or coatings on grain surfaces. EDS spectra confirmed that Fe-oxide minerals occasionally coat siliceous sponge spicules present in the RRF. Spectra of pristine siliceous spicules normally show only silica and oxygen, but Fe-oxide coating, commonly goethite, has decreased relative silica abundance while enriching iron and oxygen (Fig. 4.5). Fe-oxides, and goethite in particular, form from weathering of sheet silicates that are rich in Fe (e.g., biotite, vermiculite). Goethite is overwhelmingly present in the samples analyzed and under favorable redox conditions is usually dominant with regard to other Fe-oxides (Scheffer et al., 1976). Iron oxides were present in nearly every sample, albeit always in insignificant amounts.

Fluorite

Based on morphology, fluorite minerals present in the RRF were diagenetically precipitated. Fluorite was rare in the RRF, except in LMC-14.0, where it was the dominant component. Normalization by subtracting the fluorite from the RRF within this sample yields an average quartz content for LMC that is equivalent to the BC and GLC sections. Presence of fluorite in carbonate strata may imply cooling after oil migration, with fluorite filling porosity left from corroded carbonate matrix (Esteban and Taberner, 2003).

Estimating Detrital Component of RRF

Estimating the detrital fraction from the varied components of the RRF is extremely challenging. While it is clear that detrital material for the RRF could represent clay minerals, quartz grains, and even some iron oxides and heavy minerals, to estimate the detrital component this study begins with the simplistic assumption that all non-quartz material is diagenetic. An average non-quartz fraction from all four sections was calculated and removed from the RRF. This allows isolation of the quartz fraction of the RRF.

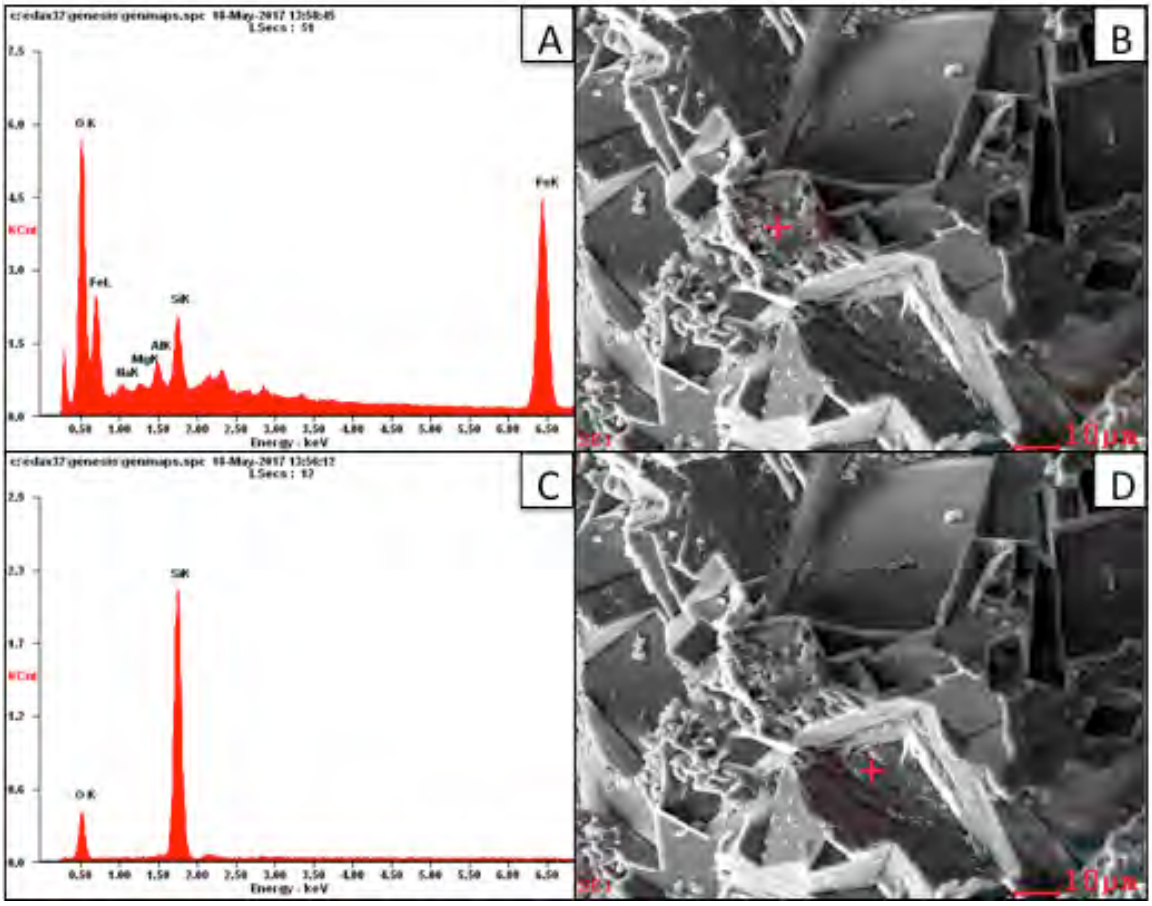

Figure 4.5: A/B show goethite coating on spicule. C/D show recrystallized quartz crystal.

The quartz fraction of the RRF contains biogenic, diagenetic, and detrital quartz. The author is aware of no known quantitative method for disentangling these three components; thus, the approach in this study argues first that the sponge spicule volume does not vary greatly between the four measured sections. Secondly, that most of the silica available for precipitation as chert and quartz overgrowths derives from dissolution of the sponge spicules. Therefore, by estimating the average volume of sponge spicules in the sections as 10%, we can remove that value from the quartz fraction of the RRF (Table 4.1) ultimately resulting in the estimated detrital quartz RRF, hereafter termed DQRRF.

Table 4.1: Average Remaining Residue Fraction Weight Percentages for Each Section

Section	RRF Weight %	Detrital Quartz % of the RRF	DQRRF Weight %
LMC	5.39	0.69	3.69
62A	6.50	0.30	1.92
BC	22.77	0.66	15.02
GLC	3.59	0.68	2.45

Shelf By-Pass Mechanism for the Detrital Fraction

The estimated DQRRF derives from basinal slope carbonate strata and thus must have bypassed the shelf either via shallow marine processes leading to gravity flows or through eolian suspension. Sand-sized grains could not have been in eolian suspension long enough to bypass the shelf via that mechanism. However, silt could bypass the shelf through either transport mechanism (Fig. 4.6). This section attempts to sort out the transport mechanism by assessing regional studies that address silt variation and grain-size distribution of the DQRRF.

Shallow Marine Processes and Gravity Flows

Detrital grains could have been transported to the on-shelf shallow marine realm by numerous processes including fluvial transport, sabka processes, and near-shore eolian dune fields. It is unknown what processes would have driven the shallow marine basinward transport of these grains to the shelf edge; however, the shelf geometry would have certainly played a role in limiting the ability of grains to by-pass the shelf.

The sharp-based nature of the finely laminated slope deposits observed in this study, combined with distal decrease in RRF, implies that gravity flows are a likely

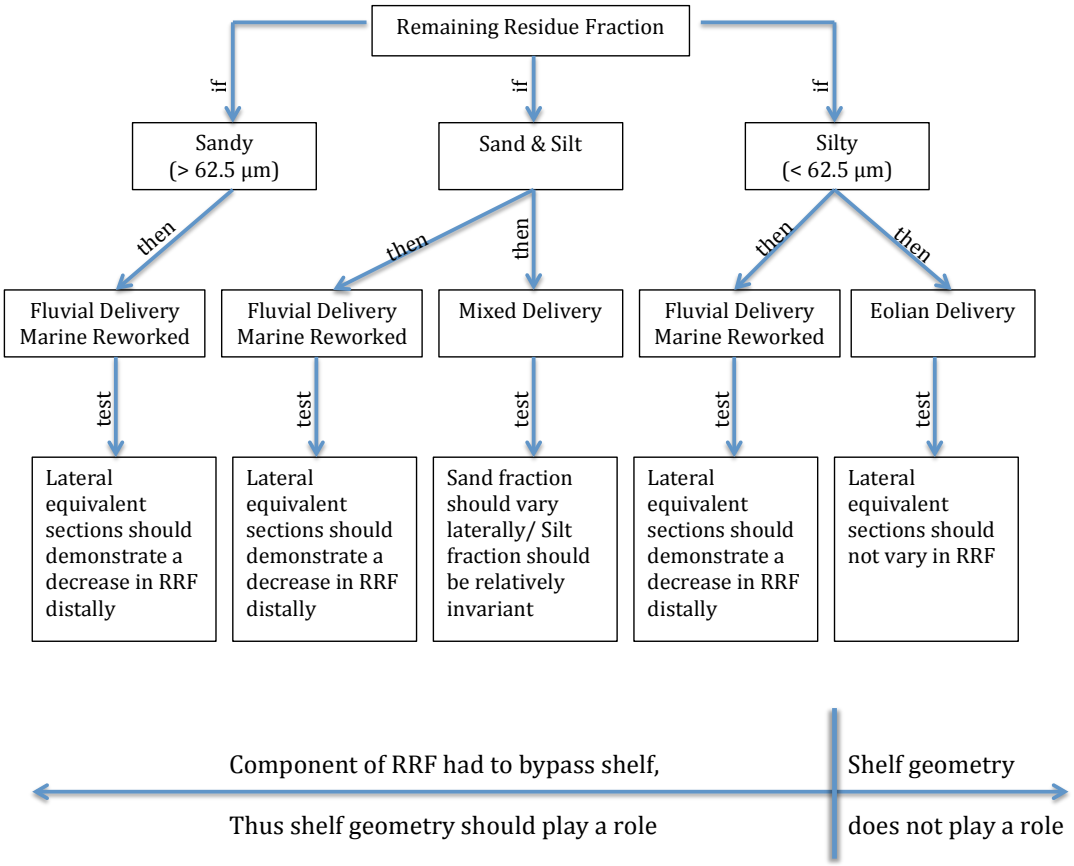

Figure 4.6: Flow chart of RRF transport mechanisms.

mechanism for sediments shed from the shelf margin to be deposited in the slope and basin. These gravity flows were most likely turbidity currents, however further work is necessary to confirm this.

Eolian Transport

Terrestrial grains moved offshore by eolian transport could have bypassed the shelf through the air, unaffected by shelf geometry. The simplest factor in determining transport is grain size (Bridge and Demicco, 2008), as grains larger than 62.5 µm likely are too large to be transported great distances by suspension. Clay and silt-sized grains may have experienced eolian suspension transport. However, if these grain sizes are interspersed in the same sample with sand, they may have also been brought

across the shelf within the water column. Here we attempt to differentiate between shelf bypass via eolian or shallow marine processes through: 1) comparison to regional studies to assess the dustiness of the period; 2) microtextural analysis of grain surfaces and 3) relative proportions of sand, silt and clay grain-sizes within the RRF.

Previous Studies

A regional assessment demonstrates the relative continuous and ubiquitous presence of silt in stratigraphic records throughout the late Paleozoic across western North America (Soreghan et al., 2008). Thus, it is hard to envision from that analysis that temporal changes in silt abundance could be responsible for variations observed in this study. For example, locations nearby the study area such as the Midland Basin and Oklahoma do not appear to show variation in the quantity of silt between the Kungurian (Leonardian) and Capitanian (upper Guadalupian) stages (Fig. 4.7). Higher frequency temporal variation in atmospheric silt flux may also exist. Sur et al. (2010) demonstrated that eolian derived silt content in Pennsylvanian strata atop the Horseshoe atoll in the Midland Basin peaked during early lowstand intervals atop subaerial unconformities. That study further demonstrates decreasing upward silt content into highstand deposits suggesting that, at least for the Pennsylvanian, atmospheric silt content was a full order of magnitude lower than the data presented in this study (Fig. 4.8, Cf. Table 4.1). This is notable given that the Midland Basin is generally siltier than the Delaware Basin (Soreghan et al., 2008). Thus, it is plausible that a significant portion of the detrital silt fraction was delivered by mechanisms other than eolian suspension because: 1) the RRF in this study is one to two orders of magnitude greater than highstand silt delivered to Pennsylvanian strata through eolian suspension according to studies in the nearby Midland Basin, and 2) temporal changes show consistent regional silt content in the Pennsylvanian-Permian.

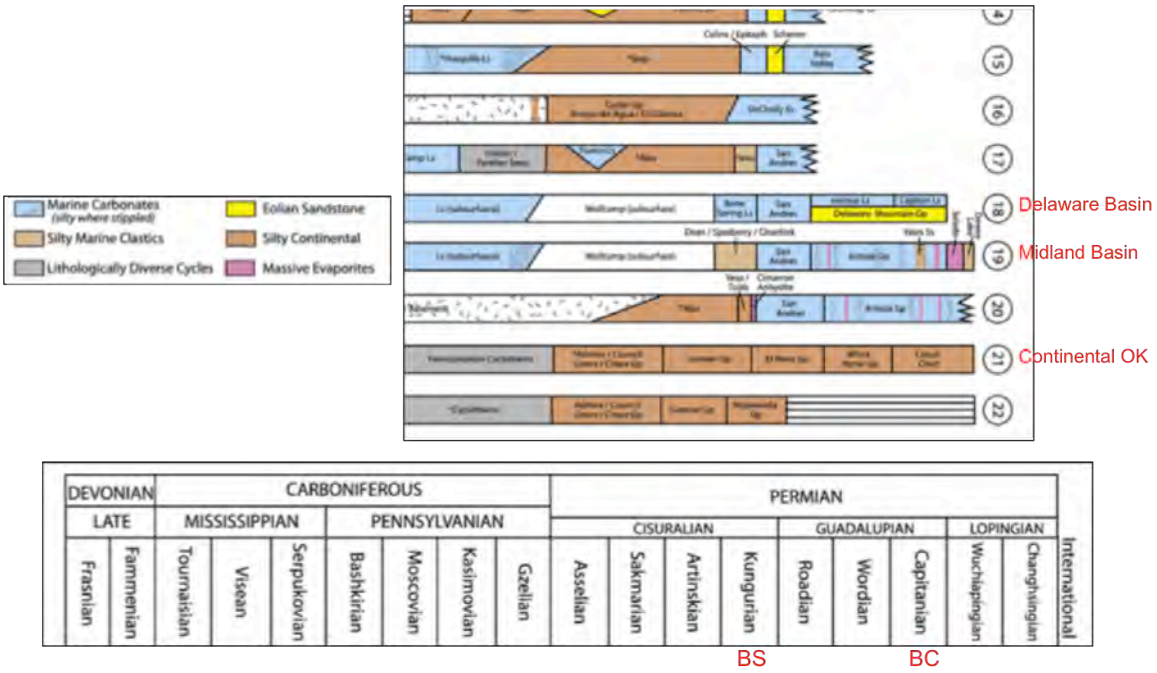

Figure 4.7: Previous regional silt study, modified from (Soreghan et al., 2008). BS shows the time of the Bone Spring Formation (Leonardian), BC shows the time of the Bell Canyon Formation (Guadalupian).

Eustatic phase		Climatic phase	Lithology and environment	Average SMF (wt%)	Relative variation of SMF with respect to minimum SMF*	Atmospheric dustiness and aridity	Average SMF MAR (g/cm2/kyr)	Mode of SMF MAR (g/cm2/kyr)
LOWSTAND	Early	Incipient glacial	Very shallow marine Carbonate	0.3034	3.76	Moderately high	0.0147	0.02 to 0.03
	Late	Glacial	Terrestrial mudrock (pedogenically altered loess)	89.725	1113.22	Maximum	1.57‡ and 15.7**	1.585‡ and 15.85**
TRANSGRESSION	Early	Incipient interglacial	Terrestrial mudrock (pedogenically altered loess) and very shallow to shallow marine carbonate	0.847	10.51	High	0.0498	0.03 to 0.05
	Late	Interglacial	Relatively deep marine carbonate	0.0806	1.00	Minimum	0.0023	0.003 to 0.005
HIGHSTAND	Early	Interglacial	Intermediate depth marine carbonate	0.0806 to 0.1036	1 to 1.28	Minimum to low	0.0023 to 0.0068	n.d.
	Late	Interglacial	Shallow marine carbonate	0.1036	1.29	Low	0.0068	0.003 to 0.007

* Relative variation of SMF is calculated by dividing average SMF (wt%) by minimum average SMF (wt%).
‡ Mudrock SMF corresponding to 5 kyr age model.
** Mudrock SMF corresponding to 50 kyr age model.
n.d. Not determined (in sufficient number of data points)

Figure 4.8: Previos regional silt study, modified from (Sur et al., 2010). Notice the maximum reported average SMF (similar to RRF) from highstand carbonates is 0.1036%.

Quartz Microtexture Fingerprinting

Transportation of quartz grains can leave distinct microtexture fingerprinting on the grains, unique to a variety of mechanisms. Eolian transport, for example, tends

to produce a platy texture across the grain surface which can be viewed under high power scanning electron microscope (Bull and Morgan, 2006). Although we attempted to view quartz microtextures by following a similar SEM approach, most grains have accumulated coatings of clay minerals and quartz overgrowths, which hide original texture (Fig. 4.9). The only grain with visible microtextures exhibits rounded and bulbous edges that are cross cut by v-shaped percussion cracks (Fig. 4.10). The high degree of rounding, low relief and bulbous character of the grain resembles eolian grains (e.g., Mahaney, 2002). V-shaped cracks are indicative of saltation and traction during subaqueous transport (Margolis, 1968; Mahaney et al., 2001; Sweet and Brannan, 2016). First-principle crosscutting relationships then suggest that this grain experienced eolian transport followed by subaqueous transport. This is consistent with the idea that eolian sands fed siliciclastic sediments into the Delaware basin (Mazzullo et al., 1985). Subaqueous transport would then be shallow marine transport or reworking. A sole grain is clearly insufficient data to draw any strong conclusions; nevertheless, it seems very likely that this sand-sized grain was deposited within carbonate strata during highstands on the slope after experiencing eolian transport and subaqueous transport.

Grain-Size Test

A flow chart representing possible delivery mechanisms, and tests for those mechanisms, of transport types for RRF of the slope and basinal carbonate strata has been constructed (see Fig. 4.6). Sand-sized grains (larger than 62.5 μm) will not be transported by eolian suspension over long distances. The presence of grains larger than 62.5 μm would imply a combination of fluvial or eolian dune delivery reworked by marine processes, to bring the sand across the shelf, and gravity flows to bring it out into the basin. Because both sand and silt-sized detrital grains are present in the RRF, at least some component of delivery must have been fluvial. A simple logic test can be used to determine if this was the only mechanism, or if there were an eolian delivery component as well, which would have created a mixed system. The majority of material transported fluvially and delivered by marine processes would settle on the

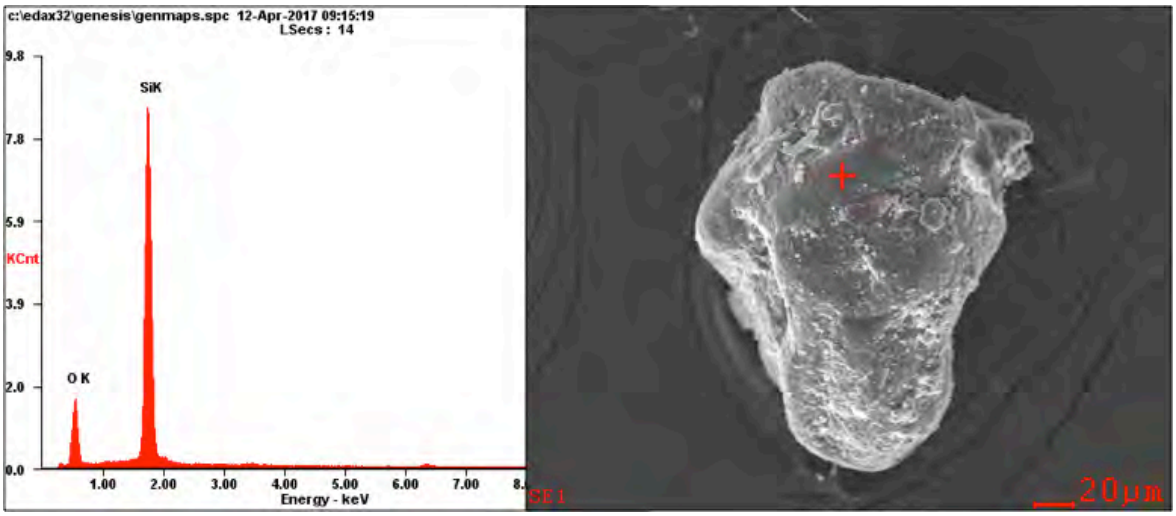

Figure 4.9: Quartz grain with clay coating and quartz overgrowth hiding much of its microtextures.

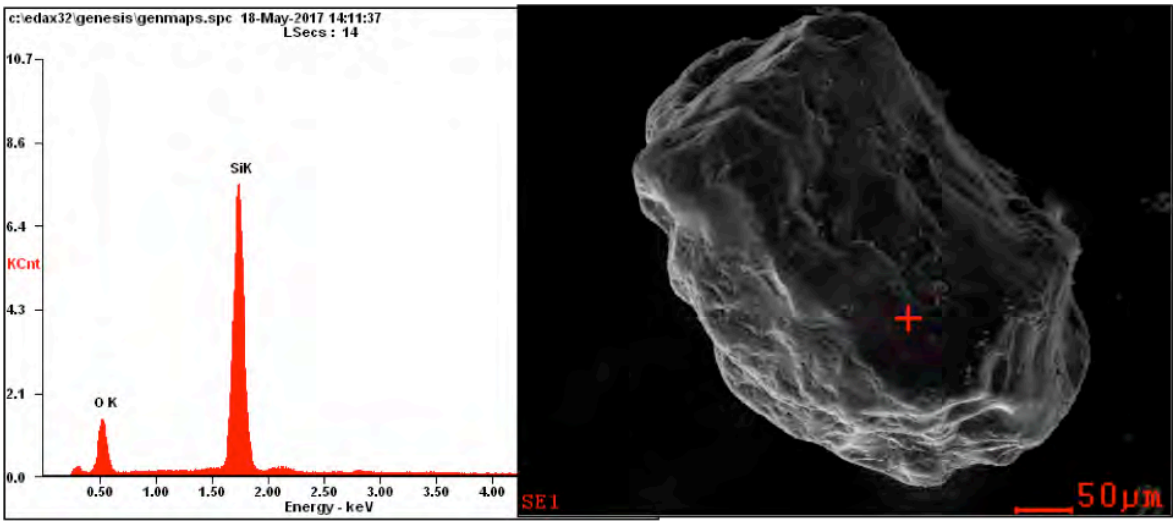

Figure 4.10: Quartz grain with visible microtextures including bulbous edges and V-shaped percussion cracks.

slope and not make it out deeper into the basin. Therefore, lateral equivalent sections should demonstrate a decrease in RRF distally. On the other hand, the fine fraction of the RRF should be relatively invariant between equivalent sections if it was delivered via eolian transport.

Because the coarse RRF is largely insignificant compared to the fine RRF, the total RRF weight percent of lateral sections can be compared (see Table 4.1). In the rimmed system, the two Bell Canyon sections showed little variability in RRF, actually increasing slightly proximally (5.4%) to distally (6.5%), implying mixed shelf

bypass and eolian delivery. Comparing the DQRRF proximally (3.7%) to distally (1.9%) shows a decrease in detrital grains away from shore, as expected if material was bypassing the shelf rather than accumulating by fallout from eolian suspension (see Fig. 4.6). The hypothesis for this study predicts that minimal material bypasses a rimmed shelf edge. The lateral consistency and relative percentage of the data appear consistent with this hypothesis.

In the ramp system, there is a substantial decrease in RRF proximally (22.8%) to distally (3.6%). The same trend is observed with the DQRRF, decreasing from 15.0% proximally to 2.4% distally. We previously noted that the two sections are not laterally equivalent (uppermost Leonardian Bone Spring vs. Leonardian/Guadalupian Cutoff). It is entirely possible that a secular event during deposition of the Cutoff Formation resulted in a substantial decrease in siliciclastic sediment transport; however, regional assessments show no hints of that event (Soreghan et al., 2008). The location of the shelf edge for both formations is in a similar position (Hurd et al., 2016); thus it seems likely that downslope position is the simplest explanation. The hypothesis of this study predicts that a ramp geometry will exhibit downslope fining and relative high percentages of detrital siliciclastic material. The data appear to be consistent with the hypothesis. Although the higher RRF of the proximal ramp section compared to all others may be due in part to more sponge spicules and chert fragments inflating the RRF, but this could not explain the entire gap.

Reworked Material of Prior Transport

It is possible that some of the RRF did cross the shelf during the prior lowstand and subsequently was reworked into the highstand strata; however, there is no evidence to support significant scouring. Weakly erosional gravity flows are common, yet no deep scouring within sections was observed.

Shoreline Location and Width of the Shelf

One additional possible variable between the rimmed and ramp systems of this study is the lateral distance between the shoreline and the shelf break in each system. Logically, a system with a shelf crest closer to the shoreline should have an easier time getting siliciclastic material across the shelf and into the basin as gravity flow deposits.

Facies distribution and sequence stratigraphic interpretation from Tinker (1998) was used to determine the distances from shoreline to shelf break throughout upper Guadalupian times (Fig. 4.11). Using the shelf crest as a shoreline indicator and the Capitan Reef as the shelf-edge break (Tinker, 1998) enables constraint on the distance between the two by making a direct measurement of their locations. The distance representing the amount of water that terrestrial detrital grains would need to transect in order to be deposited in the basin can thus be determined for each composite sequence of the Bell Canyon Formation (Fig. 4.12). Specifically for the Lamar Member of the Bell Canyon Formation (Y6 cycle), where the two rimmed system sections likely occupied, the distance from shoreline to shelf crest was measured to be 354 meters. More proximal facies largely consisted of siltstone, algal-laminated carbonate and silty dolomite (Tinker, 1998). Therefore, local very shallow water could have periodically existed to the west of the shelf crest, thus the estimates of transport distance presented here are minimums.

The Bone Spring Formation, where the Bone Canyon section was measured, was deposited in the late early Permian (Leonardian). At that time, the shoreline was pushed about 150 km from the shelf-edge break (Blakey, 2013). A change in shelf size of that magnitude means that terrestrial detrital grains would have had to travel orders of magnitude farther across shallow waters before deposition in the basin.

Based off of distance grains must travel alone, it would be easy to say that the Bell Canyon sections would have a higher RRF than the Bone Spring section. However, as this study's data shows, this is not the case. The Bone Canyon section having a higher RRF, despite the parity of grains having possibly an extra 150 km distance of travel to bypass the shelf, is further evidence that the rimmed platform

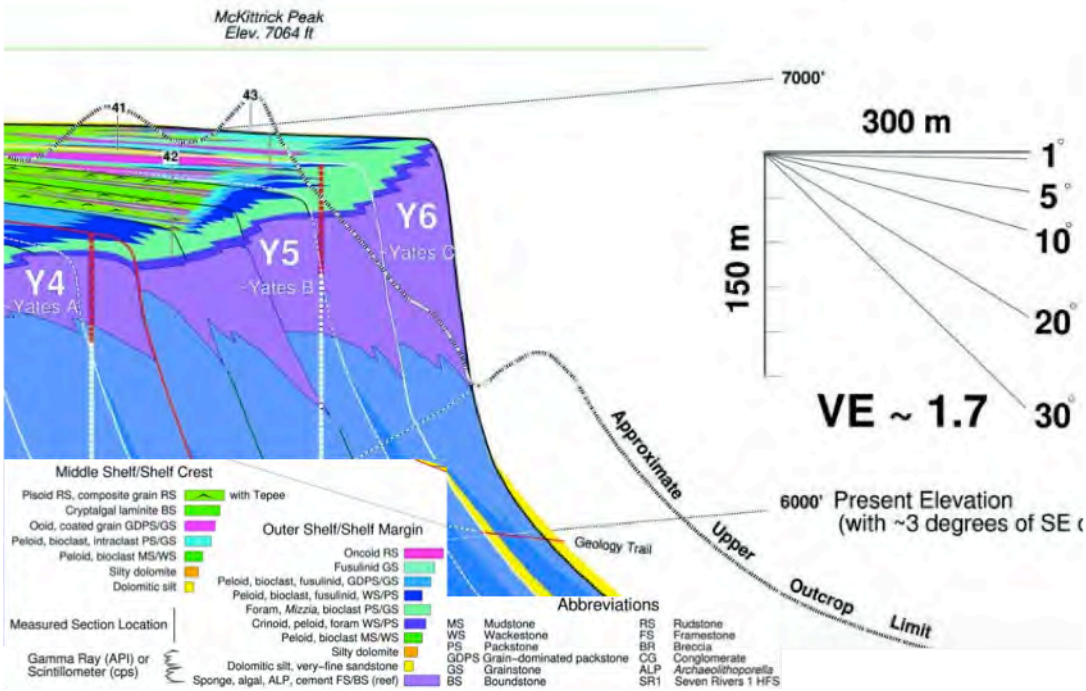

Figure 4.11: Locations of distinct facies on the rimmed margin. From Tinker (1998).

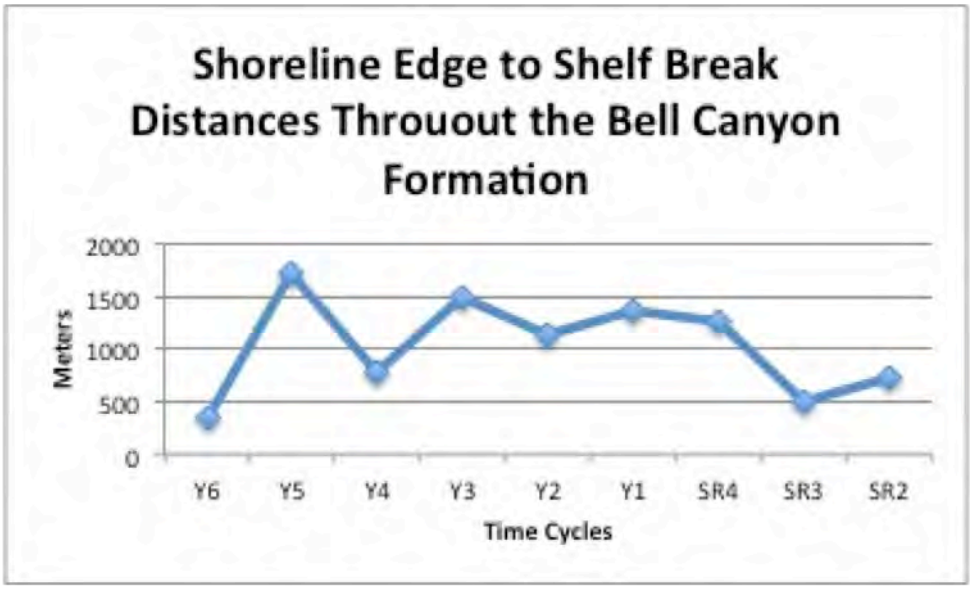

Figure 4.12: Time cycles from left to right represent young to old. Cycle Y6 represents the youngest unit of the Bell Canyon Formation, the Lamar Member.

coeval to the Bell Canyon Formation may play a role in blocking siliciclastic grains from reaching the basin during relative highstand.

Diagenetic History

In order to test diagenetic history, we utilized the Quartz Crystallinity Index (QCI) and assessed clay mineralogy. Both methods prove significant diagenetic imprinting did occur, and provide insight into burial history.

Quartz Crystallinity Index

The Quartz Crystallinity Index (QCI), introduced by Murata and Norman (1976) and updated by Korovkin et al. (2016), can be used for assessing pressure and temperature conditions to which quartz populations were exposed to. For our purpose, the QCI is used to determine the crystallinity of siliceous sponge spicules; this is treated as a proxy for diagenesis. Testing QCI involves measuring parameters of a specific quartz peak, found at 67.77° on any given XRD spectrum, yielding a representation of peak intensity compared to background noise, scaled from 0-10 (Fig. 4.13). The highest value (i.e., ten) represents clear, euhedral quartz, while values less than one represent poor crystallinity. The isolated spicules' poor crystallinity was revealed by their 0.13 QCI value, compared to other samples containing detrital and inorganic diagenetic quartz that ranged from 0.47 to 5.8 (Table 4.2).

Coarse fractions typically showed a lower QCI than their fine counterpart in sections with spicules. This is counterintuitive, but likely due to the coarse fraction containing more, and larger, siliceous sponge spicules than the fine fraction, which only contained small and broken spicule pieces. Chert fragments composed dominantly of microcrystalline quartz cement have low QCI values as well, albeit substantially higher than the spicules. Poor crystallinity may be characteristic of diagenic microquartz (Murata and Norman, 1976), which the chert fragments qualify as.

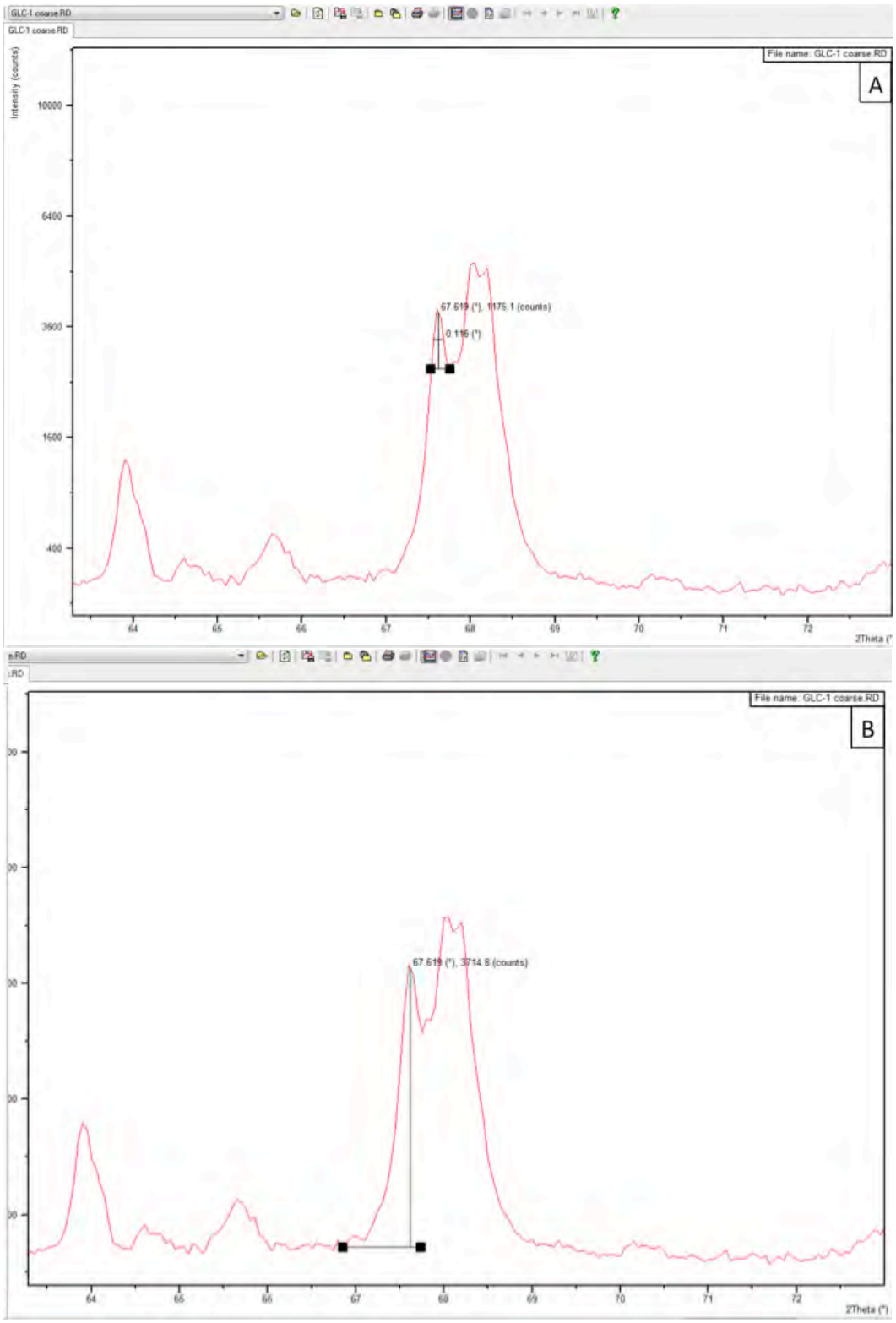

Figure 4.13: A shows the measurement of the specific quartz peak and B represents the measurement of the background noise needed to measure Quartz Crystallinity Index. Modeled after Murata and Norman (1976) and Korovkin et al. (2016).

Table 4.2: Quartz Crystallinity Index Controlling Factors

Sample	Location	QCI	Spicule Abundance	Other Quartz
BC-27.2 (coarse)	Proximal ramp	5.78	Not observed	Detrital silt and inorganic diagenetic
GLC-1.15 (fine)	Distal ramp	5.64	Rare	Detrital silt and chert rock fragments
BC-1.75 (fine)	Proximal ramp	5.58	Present	Detrital silt and inorganic diagenetic
62A-0 (whole)	Distal rimmed	5.49	Present	Detrital silt/sand and inorganic diagenetic
GLC-1.15 (coarse)	Distal ramp	5.28	Present	Detrital silt and chert rock fragments
BC-1.75 (coarse)	Proximal ramp	5	Common	Detrital silt/sand and inorganic diagenetic
BC-27.2 (whole)	Proximal ramp	4.1	Not observed	Detrital silt and inorganic diagenetic
BC-27.2 (fine)	Proximal ramp	3.42	Not observed	Detrital silt and inorganic diagenetic
BC-145 (fine)	Proximal ramp	2.73	Rare	Detrital silt and inorganic diagenetic
GLC-8.0 (whole)	Distal ramp	1.79	Common	Chert rock fragments
BC-16.6 (chert fragments)	Proximal ramp	1.72	Not observed	Chert rock fragments
BC-145 (coarse)	Proximal ramp	0.47	Present	Detrital silt/sand and inorganic diagenetic
BC-1.75 (spicules)	Proximal ramp	0.13	~100%	None

Results showing that spicules from studied samples have recrystallized as quartz, but have poor crystallinity, imply that sediment reached a high enough burial temperature to convert the original biogenic opal to quartz. However, the spicules may not have been altered past cryptocrystalline quartz in the diagenesis sequence, since their QCI is substantially lower than the chert fragments composed of microcrystalline quartz.

Clay Mineralogy

X-ray diffraction and scanning electron microscopy both show a range of smectite to illite-smectite mixed-layer clay minerals present in the RRF of samples (Table 4.3). The origin of mixed-layered clay minerals is usually linked to diagenetic transformations via a series of mixed-layer intermediates that stem from smectite being progressively converted to high charged illite or chlorite (Hower et al., 1976; Burley, 1986). Alternatively, surface or shallow subsurface alteration of mica/illite may produce illite-smectite mixed-layer minerals (Millot, 1970; Šegvić et al., 2014). The nature of clay minerals can be conveniently assessed from EDS phase chemistry (e.g., Welton, 1984). The Si/Al intensity ratio is particularly helpful to distinguish Si-rich clay minerals (i.e., smectites) from those having less silica per formula unit (i.e., illites). SEM-EDS investigation enabled to distinguish three main clay species in analyzed samples: smectite (Fig. 4.14), mixed-layer illite-smectite with up to 90% of illite component (Fig. 4.15), and illite (Cf. Fig. 4.16, Fig. 3.33).

X-ray diffraction conducted on the clay-sized fraction of one or two representative samples from each section (Fig. 4.17) allowed more insights in clay mineralogy of analyzed sediment; however, more work should be done to corroborate these preliminary findings (Table 4.4). The effects of iron fluorescence curving the shape of the background and generating an increase of intensity from ~15 °2θ were documented in all clay-sized fraction XRD measurements. This must be due to the myriad of low-crystallinity crystallites of Fe-oxyhydroxydes in each clay-sized fraction analyzed. Parameters used to distinguish between corresponding depositional environments were the following: relative amounts of 10Å phases (mica/illite),

Table 4.3: Clay Mineralogy Based on Elemental Data

Sample	Mg	Al	Si	K	Fe	O	C	Total	Si/Al	Mineral Interpretation
GLC-0.9	0.64	23.53	30.96	9.69	0	27.62	7.28	99.72	1.32	Mica
GLC-0.9	1.31	11.5	30.27	5.5	17.55	23.26	10.61	100	2.63	Illite
GLC-0.9	0.75	10.32	43.25	6.41	15.51	10.79	7.14	94.17	4.19	Mixed layer illite/smectite
GLC-0.9	1.14	17.75	40.16	7.15	0	25.51	7.8	99.51	2.26	Illite
BC-1.75	0.7	8.1	57.02	4.11	0	28.15	0	98.08	7.04	Smectite
BC-1.75	0.97	10.87	47.17	4.45	7.52	29.01	0	99.99	4.33	Smectite
BC-1.75	0.59	9.66	54.16	5.12	2.45	28.02	0	100	5.61	Smectite

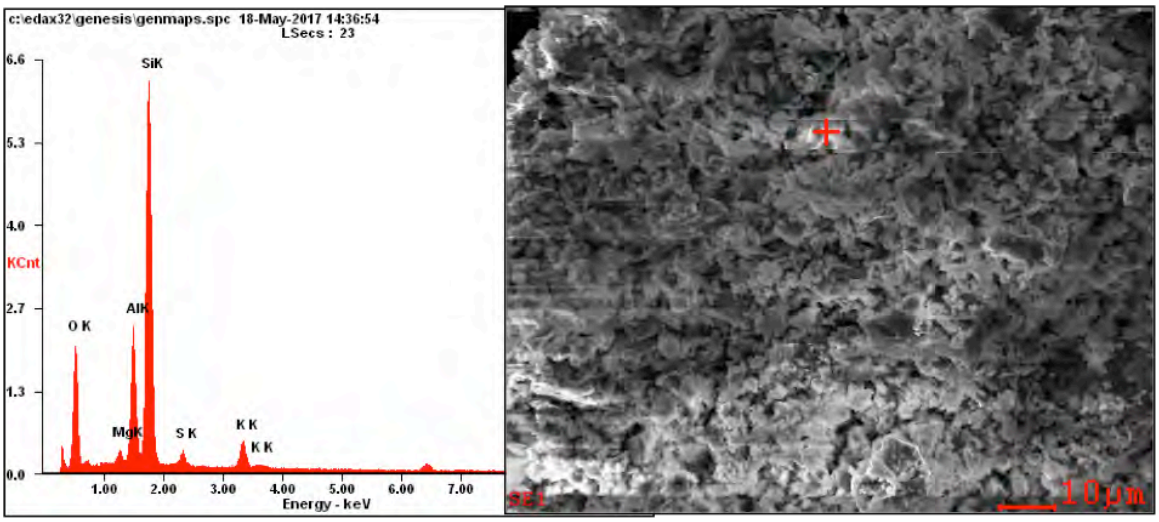

Figure 4.14: Smectite EDS phase chemistry and SEM image from BC-1.75

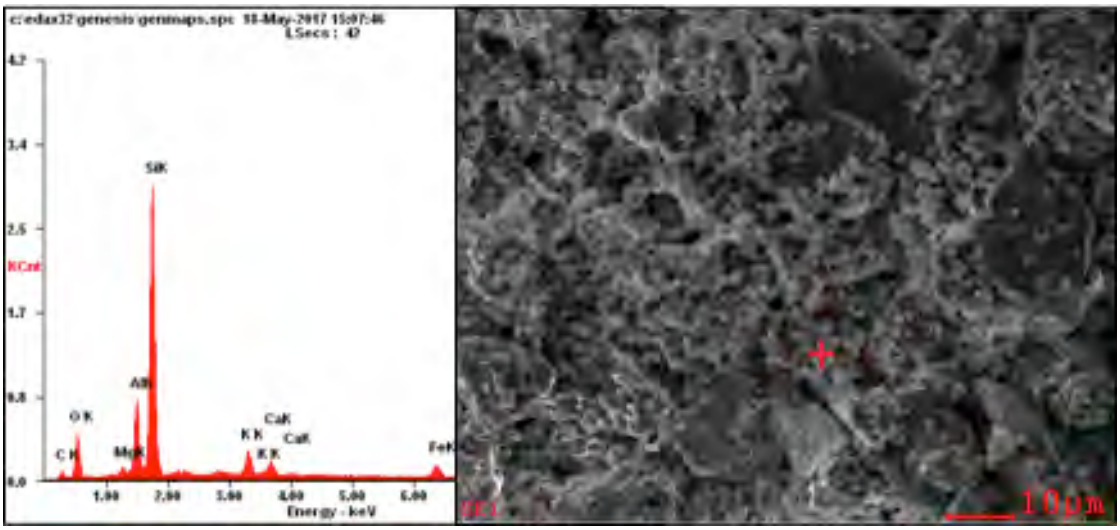

Figure 4.15: Mixed-layer illite-smectite clay EDS phase chemistry and SEM image from GLC-0.9

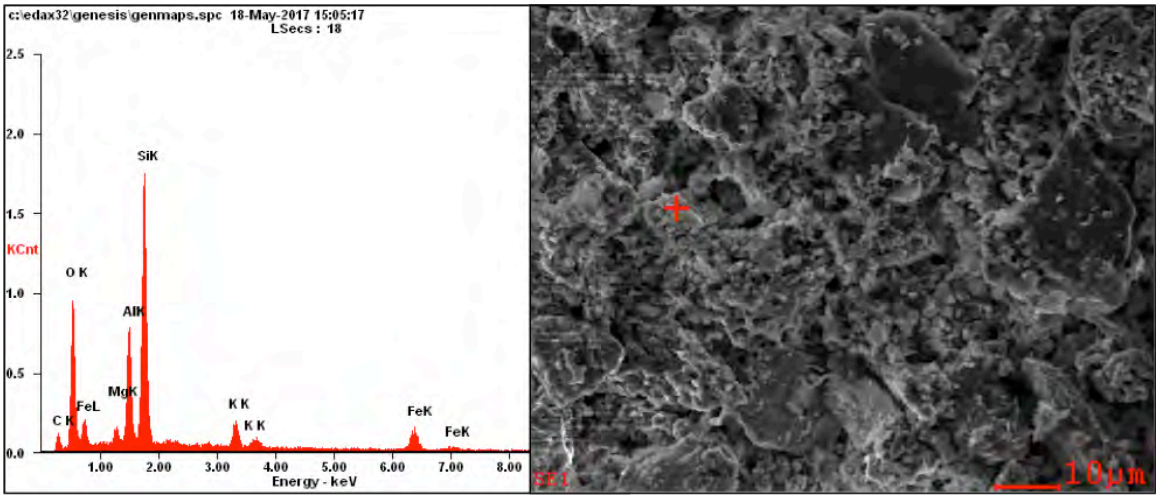

Figure 4.16: Illite EDS phase chemistry and SEM image from GLC-0.9

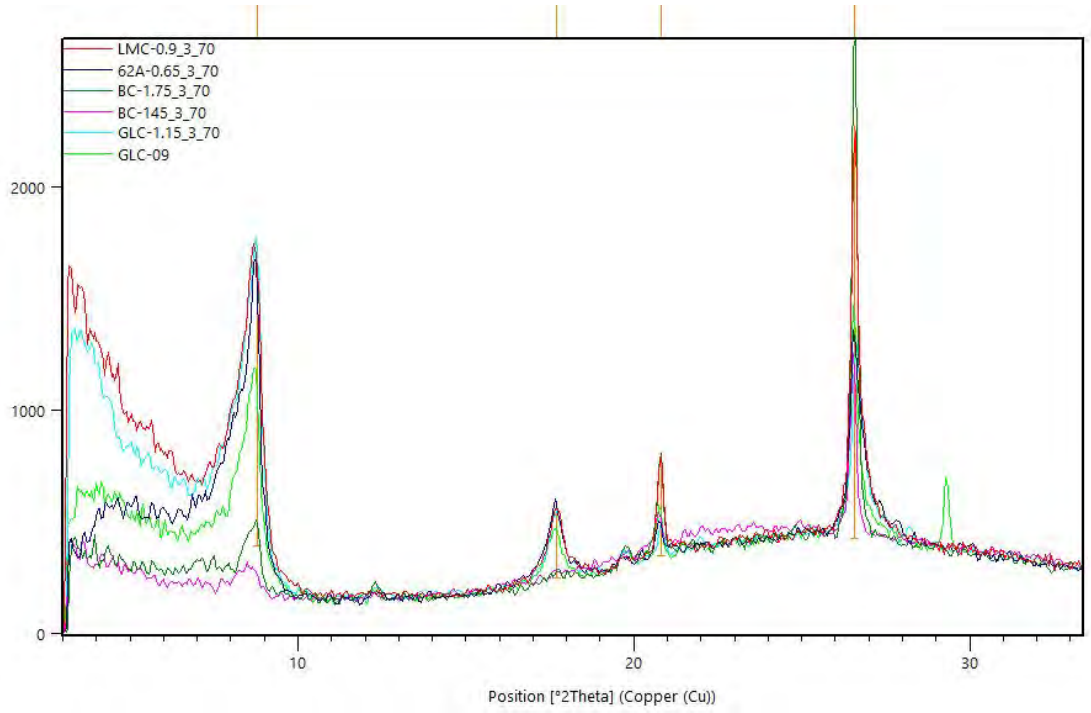

Figure 4.17: Comparative XRD spectra of clay-sized fractions.

Table 4.4: Clay-Sized Fraction Interpretation

Sample	Presence of 10Å phase	Illite-Smectite interstratification	Presence of expandable phases	Presence of 7Å phase
LMC-0.8	+	++	-	-
62A-0.65	+	++	+	-
BC-1.75	+	-	-	+
BC-145	+	-	-	-
GLC-0.9	+	+	+	-
GLC-1.15	+	++	-	-

presence of 7Å phases (kaolinite/serpentine minerals), and illite-smectite mixed layering and possible presence of expandable clay phases (14-10Å phases; Table 4.4).

Based on the relatively modest dataset, it seems that the Guadalupian sections on the slope of a rimmed carbonate platform have higher amounts of mica and mixed-layer clay minerals than the Leonardian sections on the slope of a carbonate ramp. It is impossible to make further interpretations regarding the Leonardian sections because the clay mineral signals are overshadowed by the strong presence of quartz, even in the clay-sized fraction. Furthermore, more treatment is necessary to determine the exact nature of expandable clay phases.

CHAPTER 5

CONCLUSIONS

Coeval shelf geometry likely played a role in limiting detrital quartz grains from reaching slope facies in the rimmed system that were similar to those in the ramp system. Additionally, greater transport distance from the shelf likely limited detrital quartz grains from reaching the more distal sections. The Bone Canyon section has a significantly higher RRF weight percentage than the other three sections, with an average well above one standard deviation from the mean. The BC section also has significantly higher grain-sizes, with average D_{50} and percent of sand-sized grains throughout the section over one standard deviation above each respective mean. Additionally, the percentage of quartz that makes up the RRF was as high, or higher, than all other sections (Fig. 5.1). It is clear that the Bone Canyon section, which represents a proximal ramp slope environment, has more, and larger, detrital quartz grains than any other section, which is proven by its 15.0% DQRRF (see Table 4.1).

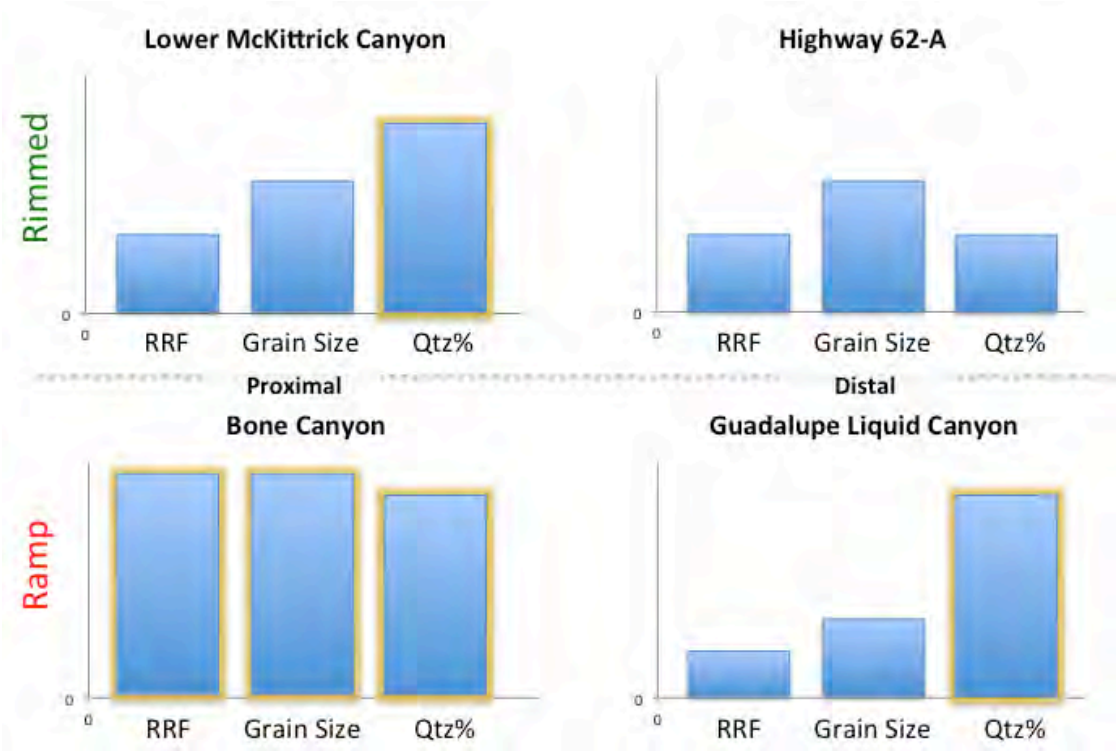

Figure 5.1: Relative comparison of RRF quantity, grain size, and quartz abundance between each section.

REFERENCES

Adams, J. E., 1965, Stratigraphic-tectonic development of Delaware Basin: AAPG Bulletin, v. 49, no. 11, p. 2140-2148.

Amerman, R., Nelson, E. P., Gardner, M. H., and Trudgill, B., 2011, Submarine mass transport deposits of the Permian Cutoff Formation, West Texas, USA: internal architecture and controls on overlying reservoir sand deposition: Mass-Transport Deposits in Deepwater Settings: SEPM, Special Publication, v. 96, p. 235-267.

Blakey, R., 2013, Early Permian.

Bozanich, R. G., 1979, The Bell Canyon and Cherry Canyon Formations, eastern Delaware basin, Texas: lithology, environments and mechanisms of deposition: Guadalupe Delaware Mountain Group of West Texas and Southeast New Mexico: Permian Basin Sect., Soc. Econ. Paleontologists Mineralogists Publ, v. 79, no. 18, p. 121-141.

Bridge, J., and Demicco, R., 2008, Earth surface processes, landforms and sediment deposits, Cambridge University Press.

Bull, P., and Morgan, R., 2006, Sediment fingerprints: a forensic technique using quartz sand grains: Science & Justice, v. 46, no. 2, p. 107-124.

Burley, S., 1986, The development and destruction of porosity within Upper Jurassic reservoir sandstones of the Piper and Tartan Fields, Outer Moray Firth, North Sea: Clay Minerals, v. 21, no. 4, p. 649-694.

Cecil, C. B., 2015, Paleoclimate and the Origin of Paleozoic Chert: Time to Re-Examine the Origins of Chert in the Rock Record.

Cys, J., and Gibson, W., 1988, Pennsylvanian and Permian geology of the Permian Basin region: Frenzel et al, p. 277-289.

Dutton, S. P., 2008, Calcite cement in Permian deep-water sandstones, Delaware Basin, west Texas: Origin, distribution, and effect on reservoir properties: AAPG bulletin, v. 92, no. 6, p. 765-787.

Esteban, M., and Taberner, C., 2003, Secondary porosity development during late burial in carbonate reservoirs as a result of mixing and/or cooling of brines: Journal of Geochemical Exploration, v. 78, p. 355-359.

Fischer, A. G., and Sarnthein, M., 1988, Airborne silts and dune-derived sands in the Permian of the Delaware Basin: Journal of Sedimentary Research, v. 58, no. 4.

Frenzel, H., Bloomer, R., Cline, R., Cys, J., Galley, J., Gibson, W., Hills, J., King, W., Seager, W., and Kottlowski, F., 1988, The Permian basin region: Sedimentary cover—North American craton: US: Boulder, Colorado,

Geological Society of America, The Geology of North America, v. 2, p. 261-306.

Gradstein, F. M., Ogg, J. G., Schmitz, M., and Ogg, G., 2012, The geologic time scale 2012, elsevier.

Harris, M. T., 1987, Sedimentology ol the Cutotf Formation (Permian), western Guadalupe Mountains, west Texas: New Mexico Geology.

-, Members for the Cutoff Formation, western escarpment of the Guadalupe Mountains, West Texas, *in* Proceedings The Guadalupian Symposium: Smithsonian Contributions to the Earth Sciences2000, Volume 32, p. 101-120.

Hartman, J., and Woodard, L., 1971, Future petroleum resources in post-Mississippian strata of north, central, and west Texas and eastern New Mexico: Future Petroleum Provinces of the United States-Their Geology and Potential. Ed., IH Cram. AAPG Memoir, v. 15, p. 752-800.

Hower, J., Eslinger, E. V., Hower, M. E., and Perry, E. A., 1976, Mechanism of burial metamorphism of argillaceous sediment: 1. Mineralogical and chemical evidence: Geological Society of America Bulletin, v. 87, no. 5, p. 725-737.

Hurd, G. S., Kerans, C., Fullmer, S., and Janson, X., 2016, Large-Scale Inflections in Slope Angle Below the Shelf Break: A First Order Control On the Stratigraphic Architecture of Carbonate Slopes: Cutoff Formation, Guadalupe Mountains National Park, West Texas, USA: Journal of Sedimentary Research, v. 86, no. 4, p. 336-362.

Jacka, A. D., Thomas, C. M., Beck, R. H., Williams, K. W., and Harrison, S. C., Guadalupian depositional cycles of the Delaware Basin and Northwest Shelf, *in* Proceedings Cyclic Sedimentation in the Permian Basin (2d ed.): 1967 Symp., W. Tex. Geol. Soc. Pub1972, p. 151-195.

Kerans, C., and Tinker, S. W., 1999, Extrinsic stratigraphic controls on development of the Capitan reef complex: SEPM Special Publication No. 65.

Korovkin, M., AnanIeva, L., Nebera, T., and Antsiferova, A., Assessment of quartz materials crystallinity by x-ray diffraction, *in* Proceedings IOP Conference Series: Materials Science and Engineering2016, Volume 110, IOP Publishing, p. 012095.

Mahaney, W. C., 2002, Atlas of sand grain surface textures and applications, Oxford University Press, USA.

Mahaney, W. C., Stewart, A., and Kalm, V., 2001, Quantification of SEM microtextures useful in sedimentary environmental discrimination: Boreas, v. 30, no. 2, p. 165-171.

Margolis, S. V., 1968, Electron microscopy of chemical solution and mechanical abrasion features on quartz sand grains: Sedimentary Geology, v. 2, no. 4, p. 243-256.

Mazzullo, S., Mazzullo, J., and Harris, P. M., 1985, Significance of Eolian Quartzose Sheet Sands on Emergent Carbonate Shelves: Permian of West Texas-New Mexico: ABSTRACT: AAPG Bulletin, v. 69, no. 2, p. 284-284.

Millot, G., 1970, Geology of Clay: Weathering, Sedimentology, Geochemistry, Springer-Verlag.

Moore, D., and Reynolds Jr, R., 1997, X-ray Diffraction and the Identification and Analysis of Clay Minerals, Oxford University Press, Oxford, England.

Murata, K., and Norman, M., 1976, An index of crystallinity for quartz: American Journal of Science, v. 276, no. 9, p. 1120-1130.

Parrish, J. T., and Peterson, F., 1988, Wind directions predicted from global circulation models and wind directions determined from eolian sandstones of the western United States—A comparison: Sedimentary Geology, v. 56, no. 1, p. 261-282.

Pray, L. C., The all wet constant sea level hypothesis of upper Guadalupian shelf and shelf edge strata, Guadalupe Mountains, New Mexico and Texas, *in* Proceedings Upper Guadalupian facies, Permian Reef complex, Guadalupe Mountains, New Mexico and West Texas. 1977 Field Conference Guidebook. SEPM Publication1977, p. 77-16.

Read, J. F., 1985, Carbonate platform facies models: AAPG bulletin, v. 69, no. 1, p. 1-21.

Sarg, J. F., 1988, Carbonate sequence stratigraphy: SEPM Special Publication No. 42.

Scheffer, F., Schachtschabel, P., Blume, H.-P., Hartge, K., and Schwertmann, U., 1976, Lehrbuch der Bodenkunde-9.

Schlager, W., Reijmer, J. J., and Droxler, A., 1994, Highstand shedding of carbonate platforms: Journal of Sedimentary Research, v. 64, no. 3.

Scholle, P., Goldstein, R., and Ulmer-Scholle, D., 2004, Classic upper Paleozoic reefs and bioherms of west Texas and New Mexico: New Mexico Bureau of Geology and Mineral Resources, v. Open-file Report 504.

Šegvić, B., Mileusnić, M., Aljinović, D., Vranjković, A., Mandic, O., Pavelić, D., Dragičević, I., and Mählmann, R. F., 2014, Magmatic provenance and diagenesis of Miocene tuffs from the Dinaride Lake System (the Sinj Basin, Croatia): European Journal of Mineralogy, v. 26, no. 1, p. 83-101.

Silver, B. A., and Todd, R. G., 1969, Permian cyclic strata, northern Midland and Delaware basins, west Texas and southeastern New Mexico: AAPG Bulletin, v. 53, no. 11, p. 2223-2251.

Soreghan, G. S., and Soreghan, M. J., 2013, Tracing clastic delivery to the Permian Delaware basin, USA: implications for paleogeography and circulation in westernmost equatorial Pangea: Journal of Sedimentary Research, v. 83, no. 9, p. 786-802.

Soreghan, G. S., Soreghan, M. J., and Hamilton, M. A., 2008, Origin and significance of loess in late Paleozoic western Pangaea: A record of tropical cold?: Palaeogeography, Palaeoclimatology, Palaeoecology, v. 268, no. 3, p. 234-259.

Soreghan, G. S., Sweet, D. E., and Heavens, N. G., 2014, Upland glaciation in Tropical Pangaea: Geologic evidence and implications for late Paleozoic climate modeling: The Journal of Geology, v. 122, no. 2, p. 137-163.

Soreghan, M. J., and Soreghan, G. L., 2007, Whole-rock geochemistry of upper Paleozoic loessite, western Pangaea: Implications for paleo-atmospheric circulation: Earth and Planetary Science Letters, v. 255, no. 1, p. 117-132.

Sur, S., Soreghan, G. S., Soreghan, M. J., Yang, W., and Saller, A. H., 2010, A record of glacial aridity and Milankovitch-scale fluctuations in atmospheric dust from the Pennsylvanian tropics: Journal of Sedimentary Research, v. 80, no. 12, p. 1046-1067.

Sweet, D. E., and Brannan, D. K., 2016, Proportion of Glacially To Fluvially Induced Quartz Grain Microtextures Along the Chitina River, SE Alaska, USA: Journal of Sedimentary Research, v. 86, no. 7, p. 749-761.

Tabor, N. J., and Montañez, I. P., 2002, Shifts in late Paleozoic atmospheric circulation over western equatorial Pangea: Insights from pedogenic mineral δ18O compositions: Geology, v. 30, no. 12, p. 1127-1130.

Tinker, S. W., 1998, Shelf-to-basin facies distributions and sequence stratigraphy of a steep-rimmed carbonate margin: Capitan depositional system, McKittrick Canyon, New Mexico and Texas: Journal of Sedimentary Research, v. 68, no. 6.

Ward, R. F., Kendall, C. G. S. C., and Harris, P. M., 1986, Upper Permian (Guadalupian) facies and their association with hydrocarbons--Permian basin, west Texas and New Mexico: AAPG Bulletin, v. 70, no. 3, p. 239-262.

Welton, J. E., 1984, SEM petrology atlas.

Williams, L. A., and Crerar, D. A., 1985, Silica diagenesis, II. General mechanisms: Journal of Sedimentary Research, v. 55, no. 3.

Wilson, J. L., 1967, Cyclic and reciprocal sedimentation in Virgilian strata of southern New Mexico: Geological Society of America Bulletin, v. 78, no. 7, p. 805-818.

APPENDIX A

RRF WEIGHT PERCENTAGES

Table A.1: Lower McKittrick Canyon Residual Residue Fraction Weight Percentages

MAB	RRF weight %
26.1	8.618670349
24.5	13.06082089
19.2	4.640872804
14	1.811186172
12.5	5.570936352
8.6	2.361999098
4.5	3.942244357
0.8	3.114876636
Average	5.390200832

Table A.2: Highway 62-A Residual Residue Fraction Weight Percentages

MAB	RRF weight %
3.45	10.31412172
2.15	3.211517165
1.65	3.359118214
1.2	3.448895545
0.65	9.952276396
0	8.696602755

Average	6.497088632

Table A.3: Bone Canyon Residual Residue Fraction Weight Percentages

MAB	**RRF weight %**
205.6	18.22990458
199.6	13.67854256
194	74.96054201
170.5	5.753733178
145	10.77108899
124.2	10.17350455
72	10.98022394
56.2	14.42188968
42.9	24.62797192
34.1	11.07615825
27.2	17.39113085
21.4	22.16096982
16.6	21.03363444
11.6	29.08458516
6.6	53.59253807
1.75	26.34305543
Average	22.76746709

Table A.4: Guadalupe Liquid Canyon Residual Residue Fraction Weight Percentages

MAB	**RRF weight %**
9.25	6.263422117
8	8.183734133
6.6	2.251239787
5	2.573083155
4.55	2.572500538
3.8	2.837262905
2.9	3.478391574
2.5	3.041012699
1.8	3.595094906
1.75	2.160082017
1.5	3.520238969
1.15	3.411532601
0.9	2.728022937
Average	3.585816795

APPENDIX B

SAMPLE LOCATIONS

Table B.1: Lower McKittrick Canyon Sample Locations

Sample (MAB)	Lat (°N)	Long (°W)
0.8	31.98314	104.74797
4.5	31.98313	104.74778
8.6	31.98321	104.74754
12.5	31.98314	104.74629
14	31.98304	104.74577
19.2	31.98264	104.7454
24.5	31.98218	104.74474
26.1	31.982	104.74461

Table B.2: Highway 62-A Sample Locations

Sample	Lat (°N)	Long (°W)
All	31.951874	104.695465

Table B.3: Bone Canyon Sample Locations

Sample (MAB)	Lat (°N)	Long (°W)
1.75	31.88353	104.88371
6.6	31.88363	104.8835

11.6	31.88365	104.88334
16.6	31.88348	104.88297
21.4	31.8835	104.88275
27.2	31.88368	104.88231
34.1	31.88421	104.88177
42.9	31.88447	104.88157
56.2	31.88429	104.88071
72	31.88418	104.88036
124.2	31.88311	104.87833
145	31.88384	104.87839
170.5	31.88381	104.87743
194	31.88386	104.87676

Table B.4: Guadalupe Liquid Canyon Sample Locations

Sample (MAB)	**Lat (°N)**	**Long (°W)**
0.9	31.845863	104.864658
1.15	31.845857	104.864621
1.5	31.845848	104.864566
1.75	31.845835	104.864685
1.8	31.845843	104.864531
2.5	31.84584	104.864484
2.9	31.84584	104.864482
3.8	31.845829	104.864469
4.55	31.845829	104.864438
5	31.845809	104.86452

6.6	31.845794	104.86451
7	31.845789	104.864513
8	31.84578	104.864513
9.25	31.845774	104.864517

APPENDIX C

THIN SECTION CLASSIFICATION

Table C.1: Thin Section Classification

Sample	Dunham (1962)	Folk (1962)	Main Allochemical Component
62A-0	Wackestone	Biomicrite	Broken hash
62A-0.65	Wackestone	Biomicrite	Broken hash
62A-1.2	Mudstone, locally Wacke	Biomicrite	Broken hash
62A-1.65	Mudstone	Silty Micrite	
62A-2.15	Wackestone	Biomicrite	Forams
62A-3.45	Wackestone	Biomicrite	Broken hash
GLC-0.9	Mudstone	Fossiliferous Micrite	Calcispheres
GLC-1.15	Packstone	Biomicrite	Brachiopod, Foram
GLC-1.5	Wackestone	Biomicrite	Calcispheres, Q, broken hash
GLC-1.75	Packstone	Foram Biosparite	Foram
GLC-1.8	Wackestone	Biomicrite	Calcispheres, Q
GLC-2.5	Wackestone	Biomicrite	Spics, calcispheres
GLC-2.9	Wackestone	Biomicrite	Spics, calcispheres
GLC-3.8	Wackestone	Biomicrite	
GLC-4.55	Wackestone	Biomicrite	Calcispheres
GLC-5.0	Mudstone	Fossiliferous Micrite	Calcispheres, spics
GLC-6.6	Mudstone	Fossiliferous Micrite	Calcispheres, spics

GLC-7.0	Mudstone	Fossiliferous Micrite	Calcispheres, spics
GLC-8.0	Packstone	Spicule Biomicrite	Spics
GLC-9.25	Packstone	Spicule Biomicrite	Spics
BC-1.75	Wackestone	Silty Biomicrite	Broken hash
BC-6.6	Wackestone	Silty Biomicrite	Q
BC-11.6	Silty wacke	Silty Fossiliferous Micrite	Q
BC-16.6	Wackestone	Sandy Biomicrite	Q
BC-21.4	Wackestone	Silty Biomicrite	Q
BC-27.2	Wackestone	Silty Biomicrite	
BC-34.1	Wackestone	Silty Biomicrite	
BC-42.9	Wackestone	Biomicrite	Broken hash
BC-56.2	Wackestone	Biomicrite	Broken hash
BC-72.0	Wack/Pack	Biomicrite	Broken hash
BC-124.2	Wackestone	Biomicrite	Broken hash
BC-145.0	Wackestone	Biomicrite	
BC-170.5	Wackestone	Biomicrite	
BC-194	Mudstone	Spicule Biomicrite / Claystone	Extraclasts and spics
BC-199.6	Wackestone	Biomicrite	Calcispheres, spics
BC-205.6	Wackestone	Biomicrite	Calcispheres, spics
LMC-0.8	Mudstone	Fossiliferous Micrite	Broken hash, calcispheres, spics
LMC-4.5	Mudstone	Fossiliferous Micrite	Allochem ghosts, broken hash
LMC-8.6	Mudstone	Fossiliferous Micrite	Calcispheres, Q silt, broken hash
LMC-12.5	Wackestone	Biomicrite	Spics, calcispheres, forams
LMC-14.0	Wackestone	Biosparite	Diverse fauna

LMC-19.2	Packstone	Foram Biomicrudite	Foram
LMC-24.5	Packstone	Foram Biosparite	Foram
LMC-26.1	Mudstone	Fossiliferous Micrite	Calcispheres

APPENDIX D

STATISTICS

Table D.1: Grain Size Trends (μm)

Section	D_{10}	D_{50}	D_{90}
62A	1.74	9.73	35.32
GLC	1.6	8.37	26.38
BC	3.16	17.56	42.68
LMC	2.46	11.24	27.27

Table D.2: Grain Size Class Distribution

Grain Size Class	LMC	GLC	BC	62A
% Clay	24.17	31.69	16.63	25.7
% Fine Silt	47.3	43.94	35.15	43.17
% Coarse Silt	27.13	23.34	43.86	28.69
% Sand	1.4	1.03	4.36	2.43
Total	100%	100%	100%	99.9%

Table D.3: Statistics

Section	Average RRF %	D_{50} grain size	% Sand	DQRRF %
GLC	3.59	8.3746 μm	1.0308	3.69
62A	6.50	9.7289 μm	2.4333	1.92
BC	22.77	17.5597 μm	4.3603	15.02
LMC	5.39	11.2425 μm	1.3963	2.45

Average	9.5625	11.7264 µm	2.3052	5.7714
Standard Deviation	8.886	4.0614	1.4934	6.2121